Biomimetic Structuring of Silicones for Cell Control and Strain-Stiffening

Dissertation

zur Erlangung des akademischen Grades
Doktor der Ingenieurwissenschaften
(Dr. Ing.)
der Technischen Fakultät
der Christian-Albrechts-Universität zu Kiel

vorgelegt von
Michael Timmermann

Kiel 2018

Referenten:
Prof. Dr. Christine Selhuber-Unkel
Prof. Dr. Rainer Adelung

Mündliche Prüfung:
19.12.2018

Erklärung

Hiermit erkläre ich, dass die beigefügte Dissertation, abgesehen von der Beratung durch die Betreuerin, nach Inhalt und Form meine eigene Arbeit ist.

Die Arbeit, ganz oder zum Teil, wurde nie schon einer anderen Stelle im Rahmen eines Prüfungsverfahrens vorgelegt und ist nie veröffentlicht worden oder zur Veröffentlichung vorgelegt worden.

Außerdem ist die Arbeit unter Einhaltung der Regeln guter wissenschaftlicher Praxis der Deutschen Forschungsgemeinschaft entstanden.

Kiel, den_____ _____

Michael Timmermann

Abstract

Scientists across a wide range of disciplines are currently engaged in artificially reproducing biological systems. In doing so, they have to ensure that the materials used fulfill certain requirements, such as deformability in the case of replicating soft biological systems. Another requirement is easy structurability in order to mimic complex biological systems. For this thesis, biological systems were recreated, too.

In the first part of this thesis research, an artificial extra-cellular matrix formed the basis for experiments with a pathogenic species of amoeba, *Acanthamoeba castellanii*. In order to find new therapeutic approaches to fighting diseases caused by this species, the migratory behavior of *Acanthamoeba castellanii* in micro-pillar structures made of silicone, which were used to mimic the confined environment of an extra-cellular matrix, was explored. For the experiments, amoebae ingested microparticles of varying shapes. While it was found that sphere-shaped particles with a diameter smaller than the distance between the micro-pillars did not impact migration behavior, absorption of larger particles by *Acanthamoeba castellanii* caused migration to be strongly reduced. However, in some instances, it appeared that *Acanthamoeba castellanii* was nonetheless able to successfully navigate the pillar structures. These observations could serve as a basis for developing methods aimed at capturing amoebae before they can enter the human body.

In the second part of this thesis, the focus was on developing a material with specific mechanical properties geared at mimicking an intra-cellular effect, namely the cross-linking of fibers within the cytoskeleton as a reaction to deformation of the cell and thereby increasing its stiffness. Emulating this effect, a strain-stiffening material was developed using a flexible, slat-structured silicone. When the material is elongated, these slats touch, thereby leading to a stiffening of the material. Employing finite element analysis, the degree to which various geometrical factors of the structure and friction between the slats affect the material's stiffening behavior was examined, and the results were verified using tensile tests. The structure that resulted from my efforts yields a stiffening behavior that is material-independent, speed-independent and reversible, and that occurs also when the material is elongated.

In this thesis, I was able to demonstrate that it is possible to employ flexible materials to imitate intracellular and extracellular structures. Artificially created materials such as these can serve as a groundbreaking solution for new therapeutic approaches to fighting pathogenic microorganisms and serve as options when choosing materials for highly specific, technical applications.

Zusammenfassung

Aktuell fokussieren sich Wissenschaftler aus verschiedensten Forschungsgebieten darauf biologische Systeme künstlich nachzubilden. Hierzu werden diverse Anforderungen an die zugrundeliegenden Materialien gestellt. So werden, um zum Beispiel weiche biologische Systeme nachzustellen, deformierbare Materialien benötigt. Weiterhin sollten die Materialien strukturierbar sein, um die teilweise sehr komplexen Strukturen biologischer Systeme nachzubilden. Auch in dieser Arbeit sollten biologische Systeme nachgestellt werden.

Eine künstliche extrazelluläre Matrix war die Basis für Experimente mit der pathogenen Amöbenspezies *Acanthamoeba castellanii* im ersten Teil der Arbeit. Auf der Suche nach neuartigen therapeutischen Ansätzen gegen Krankheiten, die von dieser Spezies verursacht werden, wurde deren Migrationsverhalten in mikrostrukturieren Säulenstrukturen aus flexiblem Silikon, die die beengende Umgebung der extrazellulären Matrix darstellen sollten, untersucht. Im Rahmen der Experimente haben die Amöben Mikropartikel mit verschiedenen Geometrien aufgenommen. Kugelförmige Partikel mit einem Durchmesser, der kleiner als der Abstand zwischen den Säulen ist, beeinflussten die Migration in den Strukturen nicht. In den Fällen, in denen *Acanthamoeba castellanii* größere Partikel aufgenommen hat, war die Migration in den Strukturen stark reduziert. In einigen Fällen konnten jedoch alternative Herangehensweisen beobachtet werden, die trotzdem Migration durch die Säulenstrukturen erlaubten. Diese Beobachtungen könnten die Grundlage für Methoden bilden, zukünftig Amöben einzufangen, bevor sie auf den menschlichen Körper übertagen werden können.

Die Imitation eines intrazellulären Effektes war die Grundlage für die Entwicklung eines Materials mit definierten mechanischen Eigenschaften im zweiten Teil der Arbeit. Die Fähigkeit von Zellen, als Reaktion auf eine Deformation Fasern im Zytoskelett zu vernetzen und somit ihre Steifigkeit zu erhöhen, wurde in dehnungsversteifenden Materialien nachgestellt. Es wurde eine Struktur aus flexiblem Silikon entwickelt, die eine Lamellenstruktur enthält. Diese Lamellen berühren sich im Fall einer Elongation des Materials und führen zu einer Versteifung des Materials. Es wurde mit Hilfe von Finite Elemente Analysen der Einfluss sowohl diverser geometrische Faktoren der Struktur, als auch der Reibung zwischen den Lamellen auf das Versteifungsverhalten des Materials untersucht. Die Ergebnisse wurden mit Hilfe von realen Zugversuchen verifiziert. Die entwickelte Struktur bietet ein materialunabhängiges, geschwindigkeitsunabhängiges, reversibles Versteifungsverhalten, das zudem auch bei einer Elongation des Materials auftritt.

Im Rahmen der Arbeit konnte ich zeigen, dass es möglich ist, flexible Materialien einzusetzen um intra- und extrazelluläre Strukturen nachzubilden. Diese künstlich hergestellten Materialien könnten wegweisend für neuartige therapeutische Ansätze gegen pathogene Mikroorganismen und für alternativen in der Materialauswahl für hochspezielle technische Anwendungen sein.

Contents

1. Introduction

It would probably be safe to say that every person in Europe has used a Velcro fastener at least once in their life. The German word for Velcro, "Klett-Verschluss", provides an indication of what inspired the technique behind the fastener. Reportedly, the inventor observed how "Kletten", or burdock seeds, clung to his dog's fur, and he then applied the underlying principle [1]. Velcro, therefore, is a good example of how biomimetics - the science of using biological mechanisms to solve a variety of problems - works. For my Ph.D. thesis I, too, have turned to biomimetics in order to solve two problems in the field of materials science.

The first problem addressed was the risk posed by disease-spreading microorganisms such as fungi, bacteria, viruses and amoebas, i.e. organisms which are transmitted via contact with other species or via contaminated water. One example of such a disease is Acanthamoeba keratitis, where amoebae invade the cornea of the human eye. The disease, which can lead to visual impairment or even blindness, primarily affects contact lens wearers who store their lenses in contaminated water [2]. One focus of this thesis was on investigating how the amoeba *Acanthamoeba castellanii* - one of the main culprits behind Acanthamoeba keratitis - behaves in confined spaces. The knowledge gathered in the process was to form the basis for developing methods aimed at preventing organisms such as *Acanthamoeba castellanii* from spreading in the human body and, even more importantly, trapping them before they invade the body. For this, the confined space had to be as similar as possible to human tissue. To create a simulation of the latter, I used a biomimetic approach to generate an abstracted form of human tissue made of silicone-based micro-pillar arrays. The distance between the pillars was chosen such that it resembled the distance between the naturally occurring obstacles in human tissue.

The second problem concerned strain-stiffening materials. "Strain-stiffening" refers to the phenomenon whereby the stiffness of a material increases when it is deformed. Such materials are already used today in applications as diverse as leaf-spring suspensions in cars or shock absorbing layers in protective clothing, and perform their task well. However, strain-stiffening materials also come with downsides that prevent their use for other tasks. For my thesis, I aimed to develop a strain-stiffening material with a wider-than-usual range of applications. For this, it was necessary to neutralize the disadvantages affecting the current crop of existing materials, namely: limited choice of underlying materials, dependency of the stiffening effect on the speed of deformation, irreversibility of the effect in some cases, as well as limitation of the effect to stiffening by material compression. To come up with a solution I again chose a biomimetic approach: imitating the capability of cells to stiffen in response to an external force through the linking up of biopolymer fibers inside the cell. I used this characteristic to develop a material which harbors none of the downsides mentioned above.

2. Theoretical Background

In this chapter, the underlying biological effects of the biomimetic approaches are described. Additionally, the state of the science for artificially structured cellular environments as well as for strain-stiffening materials are presented and discussed. In the last part of this chapter information about silicones, their mechanical behavior and the simulation of this behavior is provided.

2.1. Biological background

After a short introduction of the important components of cells, the mechanisms of cell motility, the properties of the extracellular matrix and two different effects of strain-stiffening in cells are described in this chapter.

2.1.1. Important components of a cell

Cells are the smallest units of life and are able to actively rearrange and remodel their shape and internal components. The components of a cell are the nucleus, the membrane, the cytoskeleton, the cytosol and several organelles and molecules with specific functions. The cytoskeleton and two special groups of molecules, molecular motors and adhesion molecules, play an important role in cell motility and cell stiffness and are therefore the focus of this chapter.

The cytoskeleton is composed of three types of fibers: microtubules, actin filaments and intermediate filaments. Figure 2.1 shows a sketch of the arrangement of the cytoskeletal fibers in a cell. Actin filaments form a cortex within the cell and intermediate filaments can be found in the entire cell. The microtubules are primarily connected to so-called microtubule organizing centers or centrosomes in the center of the cell and spread outward from there [3].

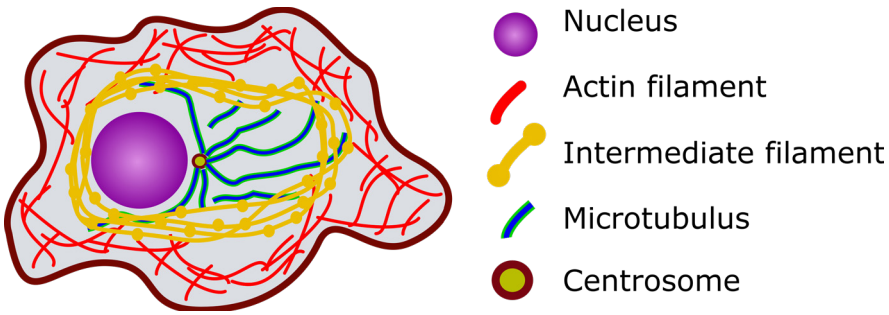

Figure 2.1: Sketch of a cell with the different parts of the cytoskeleton.

All three types of fibers are bio-polymers with proteins as monomers. A sketch of the three types of cytoskeletal fibers is shown in Figure 2.2. The two globular proteins α and β-tubulin in microtubules form dimers. They first polymerize head-to-tail into protofilaments, then arrange in a parallel

fashion into hollow tubes. The diameter of a fully polymerized microtubule is about 25 nm [4]. Actin filaments polymerize from globular actin monomers, where two parallel actin protofilaments twisted around each other into a right-handed helix [5]. The diameter of an actin filament is about 7 nm [6]. Intermediate filaments generally consist of eight protofilaments that are twisted into a rope-like structure, with a diameter of about 10 nm [6]. More than 50 different proteins that make up intermediate filaments have been identified to date [6].

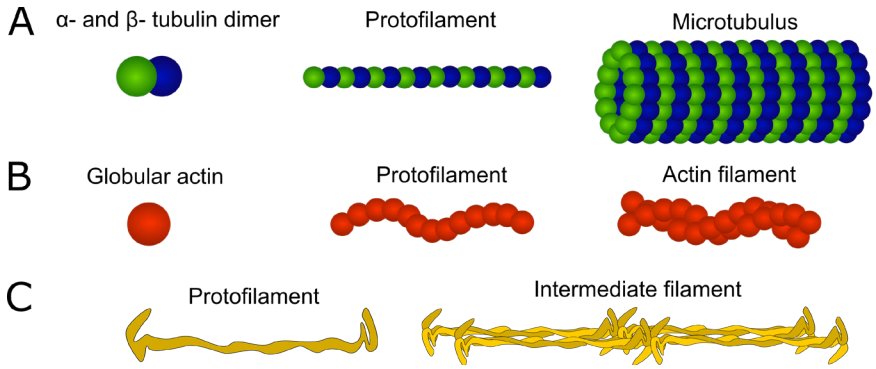

Figure 2.2: Sketches of the components forming a microtubulus (A), an actin filament (B) and an intermediate filament (C).

The three types of filaments have different mechanical properties. To describe the mechanical properties of such polymeric filaments, two values have to be introduced, namely persistence length; and contour length. The persistence length is a measure of a polymer chain stiffness and is defined as the length scale of tangent-tangent correlation decay along the filament [5, 7]. Consequently, polymer chains with a high persistence length are stiffer than those with low persistence lengths. The contour length on the other hand represents either the full length of a polymer chain [8] or the distance between network junction points or crosslinks in a network of polymer chains [7].

There are two extremes and an intermediate case for the relation between contour length and persistence length. If the contour length is considerably larger than the persistence length, the filament is considered flexible. On the contrary, when the persistence length is considerably larger than the contour length, the filament is considered to be stiff. If the difference between contour and persistence lengths is small, the filament is considered to be semi-flexible. While the contour lengths of all three types of fibers are in the same length scale of around 10 μm, microtubules have a persistence length of 1-6 mm (resulting in a stiff filament), actin filaments have a persistence length of 10-20 μm (resulting in a semi-flexible filament), and intermediate filaments have a persistence length of 1-3 μm (resulting in a flexible filament) [5, 9–11]. The different mechanical properties of filaments result in different roles in the structural integrity of cells. While the stiff microtubules act as load-bearing elements, the more flexible actin and intermediate filaments act as tension-bearing elements [11].

Apart from their mechanical properties, there are further differences between the filaments that influence the mechanical properties of the cytoskeleton. Actin filaments and microtubules are able to polymerize and depolymerize rapidly, thus can change their entire network within minutes, while intermediate filaments need hours for this task [12].

Molecular motors are a second important player in, specifically, cell motility where they are able to convert energy into motion. One example for a molecular motor is myosin II, which is able to connect two actin filaments and cause a motion of two filaments across each other by moving along both of them [3]. This mechanism is displayed in Figure 2.3.

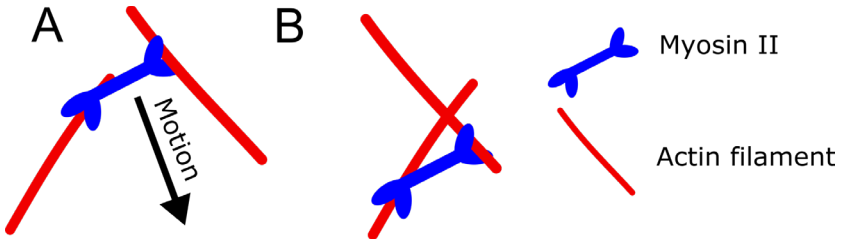

Figure 2.3A: A myosin II molecule is connected to two actin filaments. B: If the myosin II molecule moves along the filament, a motion of the actin filaments across each other is caused.

Adhesion molecules are another major player in multiple cellular functions, especially in cell adhesion. In order to change from a swimming to an adherent state, a cell needs to be in a physical contact with its environment. This is mediated by adhesion molecules like integrins that form a connection between the extracellular matrix and the cytoskeleton. The integrin is a transmembrane molecule with one end, which is outside the cell, connected to extracellular matrix molecules like collagen, fibronectin or laminin and the other end, which is inside the cell, connected to actin filaments via a clutch of proteins [3, 13]. A sketch of integrins connecting the extracellular matrix and the cytoskeleton is demonstrated in Figure 2.4.

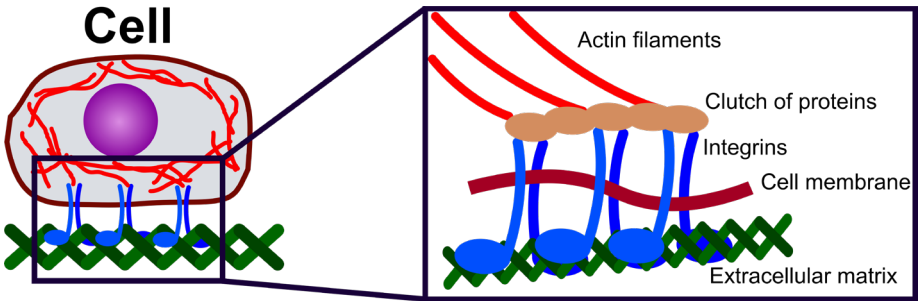

Figure 2.4: A cell adheres to the extracellular matrix with the help of integrin molecules. They are binding to the extracellular matrix outside of the cell and to cytoskeletal fibers inside of the cell.

2.1.2. Cell motility

Cell motility plays a crucial role in many biological and pathological processes. These range from gastrulation, tissue repair and immune surveillance to development disorders, vascular diseases and cancer [14–16]. In this section, the mechanisms that let cells migrate are described. These mechanisms can be divided into two major forms. One is commonly referred to as “mesenchymal motility” and one as “amoeboid motility” [17].

In mesenchymal motility, the cytoskeletal components of a cell are arranged such that a concentration gradient of biomolecules between two ends of the cell occurs. At the front end of the cell, a high amount of actin filaments is present, while their concentration at the posterior end is low. The opposite holds for myosin II molecules [15]. Actin filaments are actively cross-linked to form protrusions in the form of broad lamellipodia or spike-like filopodia, which are both stabilized by linking up with the extracellular matrix via integrins. While lamellipodia provide the basis for directional movement, filopodia are used for exploring the local environment [16]. Molecular motors are highly important here. Myosin II is required to hold the cell in shape and to prevent the formation of protrusions at lateral ends [18], and it is also responsible for the retraction of the cell´s posterior end by breaking adhesion sites [15, 16, 18]. The combination of an elongation via protrusions at the front of a cell and the retraction of a cell´s back leads to motion. This is sketched in Figure 2.5. This adhesion-based method of motion is slow and it is mainly used by adherent animal cells, like epithelial cells or fibroblasts [16, 19] and if cells move along the extracellular matrix [20].

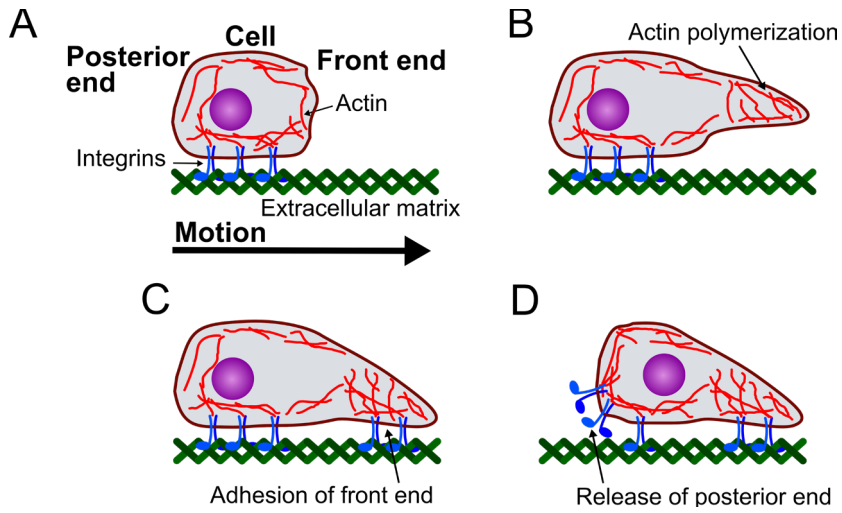

Figure 2.5: Sketch of the mesenchymal motility mechanism. A: A cell adhering to the extracellular matrix. B: The cell extends the leading edge through a remodeling of the actin cytoskeleton. C: The cell forms new adhesive contacts at the front. D: The cell moves forward by releasing the posterior end from the extracellular matrix and contracting its body.

Amoeboid motility can be found in several motile cells, like free-living amoeba or human immune cells. It is faster than mesenchymal motility by a factor of 100 to 1000 [20]. In contrast to mesenchymal motility, this method of movement is not based on strong adhesion. While rapid protrusions and retractions of extensions lead to a constant change of cell shape, an actual movement arises either from contraction-based blebbing or from polymerization-driven gliding [21]. Cells can form a bleb either by first dissociating the membrane from the cortex or by introducing a local rupture of the actin cortex. This step is followed by an expansion due to a pressure increase produced by myosin contraction. In a 2D environment, blebbing leads to motion if blebs are formed on the leading edge of a cell while weak cell adhesions to a surface are formed and the rear edge of the cell is contracted. In 3D environments, often another mechanism called chimneying is exploited. There, a cell does not need any adhesion to the substrate, instead, the growing bleb locks the cell into place while the rear

edge is contracted [22]. The chimneying mechanism is shown in Figure 2.6. Polymerization-driven gliding exploits the same mechanisms as described in mesenchymal motility. Actin that expands by polymerization below the leading plasma membrane pushes out protrusions, though no strong links to the surface are initiated. Movement is still possible if cells are immobilized due to confinement in 3D environments [21].

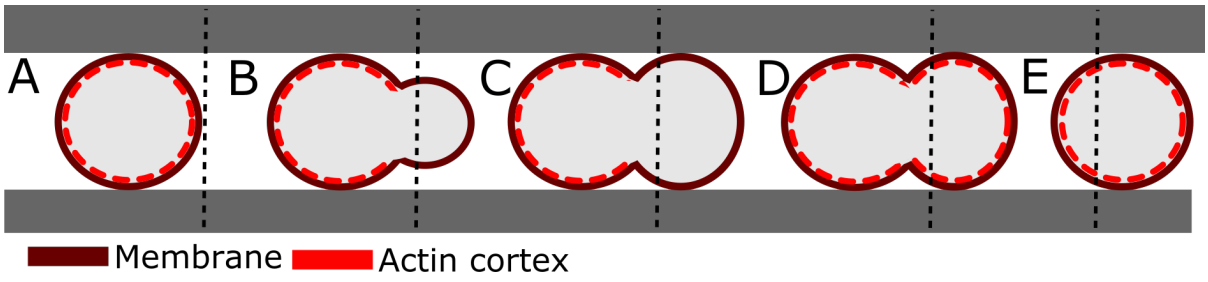

Figure 2.6: Cell motility via chimneying. A cell in a confined space (A) forms a bleb by rupturing the actin cortex (B). The bleb is used to lock the cell in place (C). After rebuilding the actin cortex (D), the rear of the cell is contracted (E).

Several studies have shown that cells, including cancer cells, can switch from mesenchymal motility to amoeboid motility in confined conditions such as three-dimensional environments [23–25]. This has raised a special interest in understanding the underlying mechanisms of cell motility. The social amoeba *Dictyostelium discoideum*, for example, has become a well-established model system to analyze amoeboid motility [15, 17, 26, 27].

There is another reason why research on the motility of amoeba is in the focus of science. While *Dictyostelium discoideum* are harmless, other amoebae are pathogenic. One of them is *Acanthamoeba castellanii (A. castellanii)*. To understand the connection between the pathogenicity and the motility of *A. castellanii*, a short description of this amoeba based on a review paper by Marciano-Cabral [28] is provided below.

A. castellanii is a species of the genus *Acanthamoeba*, which are protozoa found worldwide in soil, dust and air as well as in natural and treated water. *Acanthamoebae* have a two-stage life cycle: a dormant cyst and a trophozoite that undergoes division and actively feeds. Encystment occurs in unfavorable environmental conditions such as a lack of nutrients, desiccation or extreme temperatures. When environmental conditions are favorable, *Acanthamoebae* occur in the trophozoite stage. Figure 2.7 depicts a phase-contrast image of an *Acanthamoeba* trophozoite. Besides several cytoplasmic food vacuoles and other components of the cytoplasm like mitochondria, two features that only occur in the trophozoite stage are observable: spiny surface projections called acanthopodia and a large contractile vacuole which is responsible for the control of the cell´s water content.

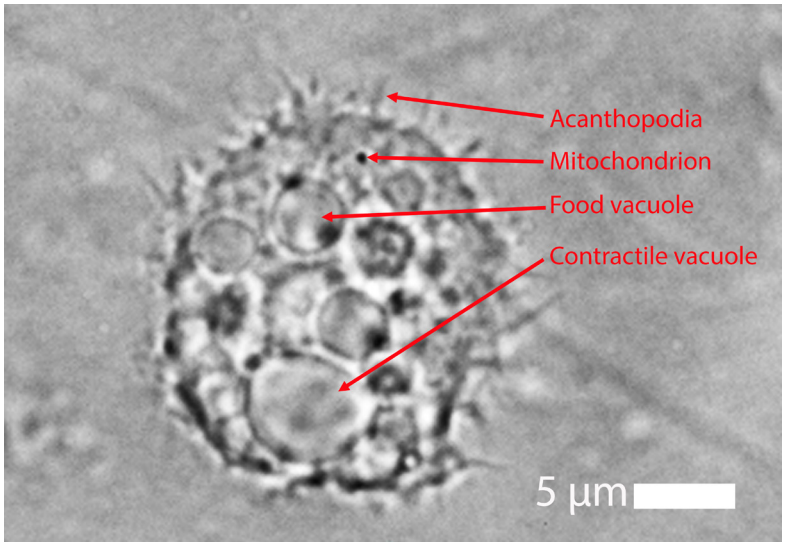

Figure 2.7: Phase contrast image of an Acanthamoeba trophozoite showing acanthapodia, mitochondria, food vacuoles and the contractalie vacuole.

Acanthamoebae are the cause of several severe diseases. In diseases like Granulomatous Amebic Encephalitis, an infection of the brain, *Acanthamoeb*ae act as opportunistic pathogens. Consequently, they are dangerous for hosts with weakened immune systems. Some species like *A. castellanii* can act as non-opportunistic pathogens and cause diseases like Acanthamoeba Keratitis, an infection of the eye. These species are even dangerous for hosts with a healthy immune system. The described diseases are caused by an invasion of Acathamoeba into the host tissue.

In nature and in the host tissue, *A. castellanii* has to be able to move in confined spaces [29, 30]. The understanding of *A. castellanii´s* motion in confined spaces might be a key to successful therapeutic approaches for diseases caused by Acanthamoeba.

2.1.3. The extracellular matrix

Generally speaking, the extracellular matrix (ECM) is the most important component of almost all human body tissues besides cells. The ECM provides a space for cells to live in, defines the physical properties of the tissue and forms the framework of the vertebrate body [31]. Consequently, it plays an important role in the movement of *A. castellanii* or cancer cells inside the body.

The ECM is composed of certain proteins and polysaccharides, most importantly collagens, fibronectin, laminin, and proteoglycans. All these are secreted by specific cell types. Depending on the type of tissue, the ratio of the components to each other and the number of cells connected to the ECM change [3].

ECM components form a three-dimensional network, as sketched in Figure 2.8. While fibronectins and laminins are small molecules that play a role in cell adhesion and matrix cross-linking, collagens

and proteoglycans are long fibers [3], which mainly form the structure that leads to cell confinement.

It has been the goal of several studies to mimic the extracellular matrix in order to investigate the cellular behavior in this confined environment. Established concepts are described in chapter 2.2.1 and a concept with new approaches is part of this work.

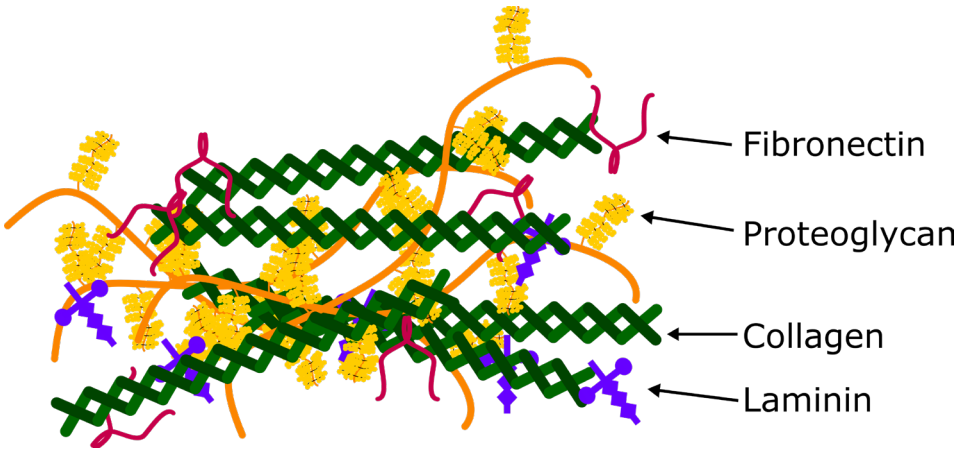

Figure 2.8: Sketch of the Extracellular matrix (ECM) with its typical components collagens, proteoglycans, fibronectins, and laminins.

2.1.4. Strain-stiffening in cells

With the help of the three components of the cytoskeleton, the actin filaments, the intermediate filaments, and the microtubules, the cell is able to react to external forces in specially designed approaches. It has been shown that cells react to fast changes of external force and slow changes of external force with two different mechanisms, a passive and an active [32].

The passive mechanism mainly arises from the mechanical properties of the actin filament network, which is composed of actin filaments and associated regulator, motor and cross-linking proteins [32, 33]. In several studies, the network was reconstructed with increasing complexity to determine their mechanical behavior. Networks cross-linked with only one actin cross-linking protein were studied in vitro [32, 34, 35], and networks with additional motor proteins were studied in vitro [36, 37] as well as by using computer simulations [37]. All these experiments showed a strain-stiffening behavior of the network. There are two main theories that try to explain the strain-stiffening behavior of networks composed by semi-flexible polymers. One theory is based on an entropic model in which semi-flexible filaments are bent weakly due to thermal fluctuations [38]. Material deformation increases the end-to-end distance of the filament segment between two cross-linking points and consequently straightens out the bending. The force needed to do so is highly non-linear [7, 38–40]. A second theory states that the stiffening mechanism is caused by filament reorientation. Upon deformation, the filaments first bend and then rotate in the direction of straining, which

results in a stretching of the filament. As filament bending requires less force than stretching, the network becomes stiffer [41].

The cell´s active reaction to external force stimuli is based on its ability to rearrange the actin filament network quickly, as described in chapter 2.1.1. When cells adhere to surfaces, they build up a connection between the surface and the actin cytoskeleton called focal adhesion [42], as depicted in Figure 2.4. The formation of focal adhesions is followed by a rearrangement of actin filaments into stress fibers that are connected to either one (dorsal stress fibers) or two (ventral stress fibers) focal adhesions. Stress fibers are cross-linked via the protein α-actinin and myosin II bundles [43]. It has been shown that an arrangement of actin filaments into stress fibers is the result of an external stimulus. Examples are the reorientation of stress fibers in endothelial cells and fibroblasts as a response to the pulsatile stretching of blood vessels [42]. In Figure 2.9, the cell´s stress fiber formation as a response to cyclic stretching as described by Greiner et al. [44] is sketched. The formation of stress fibers increases cell stiffness [45–47] and stress fibers are actively reinforced and repaired in response to external forces [48]. It has additionally been shown that stress fibers themselves are strain-stiffening elements [49].

Both mechanisms, the passive and the active response to strain, increase cell stiffness [32, 46, 48, 50, 51]. The cell uses them to protect itself from possible damage [52] and to strengthen its adhesion [53].

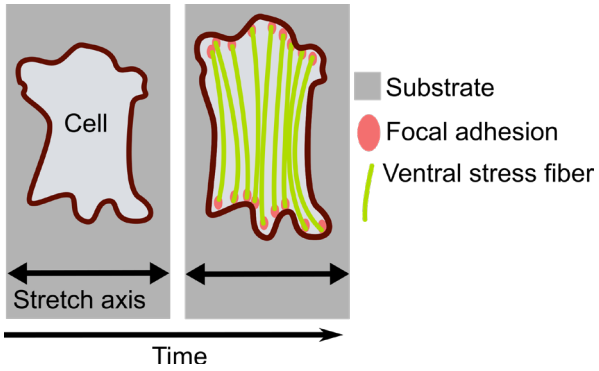

Figure 2.9: Sketch of the formation of ventral stress fibers as described by Greiner at al. [44]. Upon cyclic stretch, the cell arranges perpendicular to the stretch axis and forms focal adhesions and ventral stress fibers perpendicular to the stretch axis.

2.2. The current state of the science

As the two biomimetic approaches in this thesis address different fields of science, the state of the science for the fabrication of artificial cellular environments is described first, followed by the state of the science in the field of strain-stiffening materials.

2.2.1. Artificially structured cellular environments

There are several strategies to generate artificial environments to mimic the structure of the extracellular matrix. The goal in the field of synthetic biology is to use ECM molecules to replicate the shape and function of the extracellular matrix as close as possible [54, 55]. The major downsides of this approach are the high cost and the limited reproducibility of experiments. The next step of abstraction is the use of completely artificial materials, as they provide the possibility to precisely adjust important key parameters, like the size of the confinement or the stiffness of the material. The most prominent examples of this approach are micro channels, three-dimensional porous materials, and micro-pillar arrays. An example of each approach is sketched in Figure 2.10.

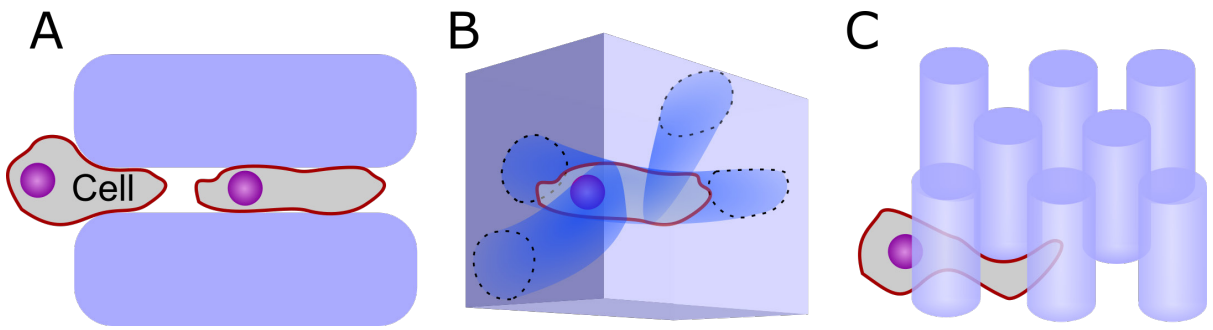

Figure 2.10: Sketches of different approaches to artificially structured cellular environments. A: Top view of a micro channel. B: A three-dimensional porous material. C: A micro-pillar array.

A micro channel is the most basic approach to mimic a confined situation for a cell. A channel with a predefined width and height is in most cases produced via silicone micro-molding and closed with a glass coverslip. Depending on the experimental goal, the width and height of the channels range from a few micrometers to several hundred micrometers [56–60]. While micro channels are well-suited to observe cellular behavior in a confined condition, they poorly represent the situation inside a three-dimensional network, like the ECM. An additional downside is the possible lack of nutrients inside closed channels [61].

An approach that resembles the situation in the ECM better than micro channels is three-dimensional porous materials. These can, for example, be produced via salt-leaching (a process where a salt is mixed with a matrix material and, after matrix curing, the salt is dissolved, leaving pores inside the material

[62]), 3D printing techniques [63], or via dissolving a network of interconnected zinc oxide tetrapods inside a hydrogel matrix [64]. The pore diameter of these materials is in the range of several tens of micrometers. Depending on the method of production, the downsides can be an uneven pore size inside the structure, low interconnection between the pores and expensive production techniques. A downside that all methods have in common is the complicated observability of cell behavior inside the three-dimensional sample with conventional light microscopes and a possible lack of nutrients.

Micro-pillar arrays lessen some of the downsides described before. Micro-pillar arrays are in most cases produced via silicone micro-molding, which results in elastomeric pillars with heights, diameters, and distances between pillars from a few micrometers to several hundreds of micrometers. The pillars can be arranged in different patterns, e.g. hexagonal patterns or simple square patterns. It is possible to precisely determine the distance between the pillars and thereby precisely define the obstacles for cells. With micro-pillar arrays, not only can the behavior of cells in a confined environment be observed (as is the case with microchannels), but also the moving pattern and problem-solving strategies if cells have the possibility to choose their direction of movement (as is the case with three-dimensional porous materials) [65–67]. Micro-pillar arrays are only quasi-three-dimensional, as they provide confinement in several directions, but not in all. This has both advantages and downsides. One advantage is the easy observability of cells in these structures. A downside is the fact that cells are not confined on the top and might, therefore, be influenced in their behavior. It is possible to close the structure on the top to avoid this downside, but this can cause a lack of nutrients. The micro-pillar arrays used in this work are open on the top.

2.2.2. Strain-stiffening materials

Today, there are already several strain-stiffening materials that were developed for special applications. Simple strain-stiffening springs are used in suspension systems in the automotive sector, certain viscoelastic materials are used as shock absorbers in protection wear and extremely specialized materials are investigated to be used in tissue engineering. While these materials are suitable for their specific application, they come with several downsides that make them unsuitable for a universal approach. In this chapter several already established strain-stiffening materials known from the literature will be presented. Their advantages and downsides, especially in regard to material-independency, speed- and material-independency of the effect and strain-stiffening upon elongation will be discussed, as these are the features making the material developed in this thesis special. To provide the reader with the necessary background about the terminology in this field, the beginning of this chapter will be used to define the terms stiffness, stiffening, and strain-stiffening.

The term stiffness is most generally defined as load divided by deformation. While a load can be for example a force, a moment, a stress or a combination of these, the deformation can be a strain, a displacement, an angle or a combination of them [68]. All of these measures are tensors. As the goal of this part of the chapter is the description of the correlation between the measures it is sufficient to

treat them as scalars. The first relevant combination is the spring constant. According to Hooke´s law of elasticity, the extension *d'* of a spring within its elastic limit is in direct proportion to the force *F* applied to it. The constant of proportionality *k* is called the spring constant [69]. Hence, the spring constant *k* is force divided by displacement.

$$k = \frac{F}{d'} \tag{2.1}$$

In Figure 2.11 a sketch of a simple force-displacement curve is shown. The slope of these curves can be determined by dividing the change in displacement by the change in force. Consequently, the slope in the force-displacement curves is equal to the spring constant of the material. As the spring constant is the measure of stiffness that can be most easily obtained from force-displacement curves, the terms spring constant and stiffness will be in this thesis used synonymously.

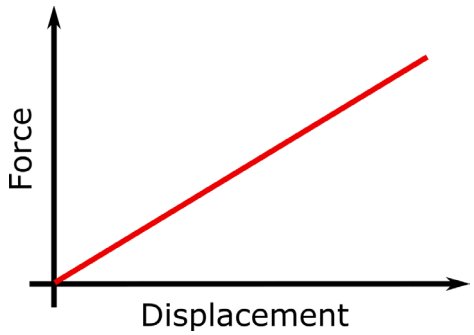

Figure 2.11: Sketch of a simple linear force-displacement curve. The slope of the curve describes the stiffness.

In materials science, the term stiff is used as the opposite of the word soft. For this reason, the term stiffening will be used here if the stiffness of a material increases.

To define the term strain-stiffening, the term strain has to be explained first. Strain (ε) is most commonly defined as the increase in length Δ*l'* of an object divided by its original length l'_0 [68]:

$$\varepsilon = \frac{\Delta l'}{l'_0} \tag{2.2}$$

In other words, the strain is a measure of displacement. If the stiffness of a material increases with increasing displacement and consequently, strain, the material is a strain-stiffening material.

Figure 2.12 shows a sketch of a force-displacement curve of a strain-stiffening material. The slope of the curve changes with displacement. Up to a certain displacement, the slope of the curve, which represents the stiffness of the material is constant. At a certain displacement the slope changes to an increased value. Starting at this displacement the material is stiffer than before.

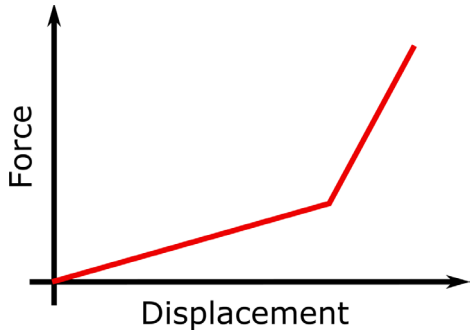

Figure 2.12: Sketch of a force-displacement curve of a strain-stiffening material.

Another measure of stiffness that is very common for the characterization of materials in materials science is the Young´s modulus. It uses normalized values for the load and the deformations. It is therefore independent of the sample geometry and can be used for the description of a material in general. According to the IUPAC Compendium of Chemical Terminology, the Young´s modulus or modulus of elasticity E is defined as the normal stress σ divided by the strain ε. The normal stress is the force acting normal to a surface divided by the area of the surface [8].

$$E = \frac{\sigma}{\varepsilon} \tag{2.3}$$

Conventional strain-stiffening materials either increase their spring constant or their Young´s modulus upon deformation. The increase in spring constant is caused by a change of sample geometry. The stiffness of the underlying material itself is not changed. If the Young´s modulus of a material is increased upon deformation, the stiffness of the underlying material is increased. This happens independently of the geometry of the material. Examples for both types of strain-stiffening materials are given in the following sub-chapters. In Table 2.1 all concepts of strain-stiffening materials described and discussed in the following sub-chapters are listed and it is marked if they fulfill the requirements that are necessary for a universally applicable strain-stiffening material: material independency, speed independency, reversibility and stiffening upon elongation.

Table 2.1: Summary of the current state of the science in the field of strain-stiffening materials. "+" means that the material fulfills the requirement. "– "means that the material does not fulfill it. A "0" means that the requirement is not discussed in the regarding publication.

	Material independency	Speed independency	Reversibility	Stiffening upon elongation	Additional remarks	References
Coil spring and leaf springs with progressive spring constant (e.g. made from metal)	+	+	+	-		[80, 82]
Porous materials (e.g. made from elastomers)	+	+	+	-		[80, 81]
Gels made from biopolymer fibers, synthetic triblock copolymers, and polyisocyanopeptides	-	+	+	+	High costs for biopolymer fibers	[36, 40, 74–79]
Gels made from poly(ethylene glycol) and branched polyethyleneimine	-	0	+	+	Temperature dependency	[73]
Gels with thiol-containing monomers within a poly(ethylene glycol)-acrylate backbone	-	-	+	+		[54]
Special viscoelastic material (e.g. a mixture of silicone, silica and boric acid)	-	-	+	+		[71, 72]
Self-stiffening composites (e.g. composites with embedded microcapsules)	+	-	-	+		[70]

2.2.2.1. Increase of spring constant

Several materials that show strain-stiffening due to an increase of spring constant upon deformation have been reported in the literature. The most prominent example is the coil spring. Its spring constant k can by calculated with equation 2.4:

$$k = \frac{Gd''^4}{8D'^3 n_a} \tag{2.4}$$

The axial compression y of a spring can be calculated with equation 2.5:

$$y = \frac{8FD'^3 n_a}{Gd''^4} \tag{2.5}$$

In these two equations, G represents the shear modulus ($G=E/2(1+v)$), with the Poisson´s ratio of the material v and die Young´s modulus of the material E. d'' represents the wire diameter, D' the mean diameter of the spring, n_a the number of active coils and F the axial force applied to the spring [69, 83]. It can be noted, that the Young´s modulus is constant in these equations.

From equation 2.5 it is evident that a spring with variable coil diameter (Figure 2.13A) would show strain-stiffening behavior upon compression. If the spring is compressed, the larger coils deform more easily. At a certain degree of compression these coils would touch each other, thus decreasing the number of active coils n_a and therefore increasing the spring constant, which is indirectly proportional to the number of active coils. A similar effect can be found in variable pitch springs (Figure 2.3B), where coils with smaller pitch p_i touch each other at a certain degree of compression and again decrease the number of active coils n_a, resulting in an increased spring constant of the whole spring [80]. The working principle of progressive multi-leaf springs is based on the same principle. These springs have additional leafs, so-called help leafs, that are shaped in a way that their contact area with the main leafs increases with increasing deformation. This increases the spring constant of the entire spring (Figure 2.3C) [82]. Springs that show an increase in spring constant upon compression are called springs with progressive spring constants. Metal springs with progressive spring-constant are often used in suspension systems of cars and trucks.

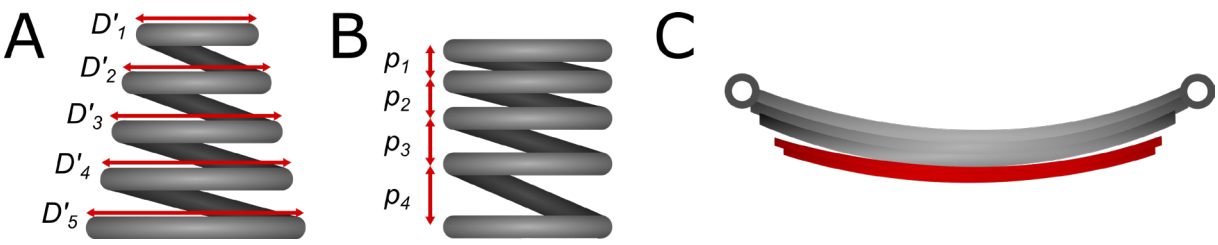

Figure 2.13: Side views of three different samples of springs with progressive spring constant. A: The diameter of the spring D'_i varies. B: the pitch p_i of the spring varies. C: A progressive multi-leaf spring. The contact area with the help leaf, marked in red, increases with increasing deformation.

An increase of spring constant upon compression can also be found in porous materials. It has been observed that the compression of a porous material does not require high forces until all pores are completely collapsed. After this point, further deformation of the material needs more force. The reason for this behavior is that the force needed to deform a material depends on the area the force is acting on. Rearranging equation 2.3 and replacing the stress with *F/A* provides a relationship between the force acting on a material and the area the force is acting on:

$$F = \frac{E}{\varepsilon} A \tag{2.6}$$

Equation 2.6 shows that with constant Young´s modulus the force needed to deform the material is directly proportional to the area the force is applied to. While at the beginning of the compression of a porous material the force only acts on the area of the material between the pores, it acts on the entire area of the material after the pores are collapsed.

For example, in the patent EP 2416030 B1 [81] the introduction of pores into a rubber material is described. Due to the pores, the rubber material shows strain-stiffening upon compression. According to the patent the material is supposed to be used as a damping system for car seats.

The springs with progressive spring constant and the porous materials described in this section show strain-stiffening by changing the spring constant of the material. The effect is reversible, speed independent and all materials showing a sufficient degree of elastic deformation can be used to build these systems. The major downside of the described examples is that they only react upon compression. None of the systems shows strain-stiffening when the structure is elongated.

2.2.2.2. Increase of Young´s modulus

Several materials that show strain-stiffening due to an increase of Young´s modulus upon deformation have been reported in the literature.

Soft polymer gels, either made from biopolymer fibers like actin, collagen, or intermediate filaments [36, 40, 79] or synthetic triblock copolymers [74, 75] and polyisocyanopeptides [76–78] are strain-stiffening. The reason why these networks show strain-stiffening is the semi-flexible behavior of their components. As described before, deformation leads to an increase of stiffness of networks of semi-flexible filaments. Two theories explain this behavior. The first theory states that thermally induced bending of the filaments is straightened out in response to deformation. The required force is highly non-linear. The second theory states that with increasing deformation filaments are first bent and then stretched. Stretching the filament needs more force than bending it. The gels described are very soft, as the network of their components is only loosely cross-linked. Their Young´s modulus is in the lower kPa region. In comparison, the Young´s modulus of silicone materials for engineering applications is in the lower MPa region [84]. This low rigidity limits the applications of the gels. One example would be the use in tissue scaffolds where the low stiffness in combination with strain-stiffening is desired [75], as it resembles the mechanical properties of the extracellular matrix. The fact that only networks of semi-flexible polymers show strain-stiffening limits the choice of materials drastically. The strain-stiffening is reversible, it can occur upon elongation and it is speed independent. The fact that it is very expensive to purify biopolymer fibers adds another downside to this special approach.

Strain-stiffening can also arise from strain induced active cross-linking in networks of synthetic polymers. Yan et al. presented gels where a Schiff base reaction between the amino groups and aldehyde groups on poly(ethylene glycol) and branched polyethyleneimine reversibly cross-link upon elongation of the gel, causing reversible strain-stiffening [73]. The stiffness of these gels is in the lower kPa region, making it, similar to the materials described before, suitable for tissue engineering applications. As the strain-stiffening is based on the cross-linking of specially designed polymers, this approach is not material-independent. Yan et al. did not discuss the dependency of the strain-stiffening effect on the deformation speed. An additional downside is the high-temperature dependency of the strain-stiffening effect of the gels. Tran et al. presented gels where the thiol-containing monomers within a poly(ethylene glycol)-acrylate backbone reversibly cross-link upon deformation, causing reversible strain-stiffening of the gel [52]. The material stiffens from 150kPa to 600kPa in cyclic tension and compression tests. As the initial, as well as the final stiffness of these gels, is considerably higher than the stiffness of the gels described before, this material might have future applications in several fields including tissue engineering. A large downside of this approach is that the stiffening takes several hours. This makes the gels unsuitable for applications were a speed independent strain-stiffening is desired. Similar to the approach by Yan et al. the strain-stiffening is based on the cross-linking of specially designed polymers. Consequently, this approach is not material-independent.

Carefully designed mixtures of polymers and fillers result in viscoelastic materials that show strain-stiffening. A well-known example is "silly putty", which consists of a mixture of silicone (polydimethylsiloxane), silica and boric acid. This material behaves more elastic than other viscoelastic materials when deformed quickly, but at the same time, it has a lower viscosity. The effect results from long entangled polymer chains that are linked by weak hydrogen bonds. If a stress is applied over a long time scale the bonds are broken and the chains untangled. The material behaves then like a liquid. Stress that is applied rapidly cause only a few bonds to break and the material behaves elastically [71]. Consequently, the Young´s modulus of the material can be increased by increasing the deformation speed. A commercial application is the usage of the material as a shock absorber. An example is the material "d3o" [72], that is used as a shock absorber in protection wear. The main advantages of strain-stiffening viscoelastic materials are the reversibility of the stiffening effect and the fact that it can occur upon elongation. The downsides are the high dependency of the effect on the deformation speed and the fact that only certain carefully designed mixtures of materials show the described behavior.

Strain-stiffening also occurs in so-called self-stiffening composites. Self-stiffening composites are inspired by self-healing materials. In certain self-healing materials, microcapsules of monomers and catalysts are dispersed in a material. When the microcapsules are ruptured due to material damage, the monomer can propagate through this damage. It comes in contact with the catalyst, polymerizes and thus repairs the material [85]. The working principle of this type of self-healing material is demonstrated in Figure 2.14. Under specially designed conditions this concept of self-healing composites can be used for self-stiffening composites. The composite can be designed in a way that deformation breaks the embedded capsules and starts the polymerization of the embedded material. If the polymerized embedded material is stiffer than the original material, the material stiffness is increased upon deformation. This concept is for example presented in a self-stiffening stent [70]. The main advantages of self-stiffening composites are the large flexibility in choice of materials and a stiffening upon elongation. The downsides are a certain speed dependency as the material takes time to cross-link and a non-reversible stiffening effect as the rupture of the embedded particles and the following polymerization is not reversible.

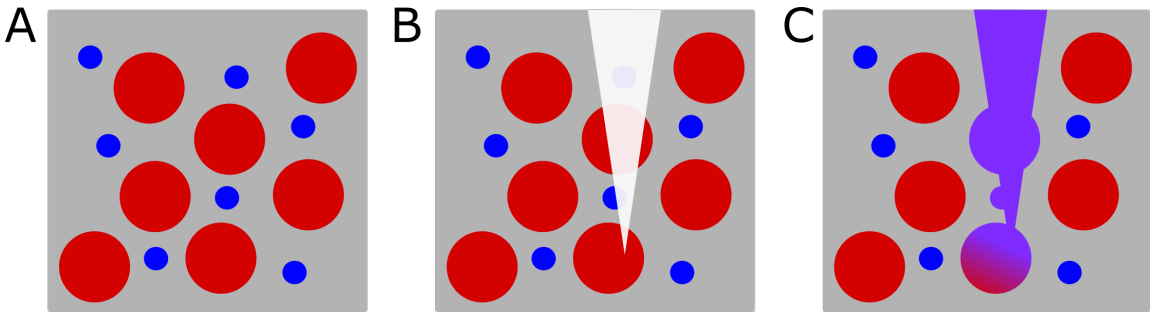

Figure 2.14: Sketch of the working-principle of one type of self-healing composites. A: Microcapsules of a monomer (red) and a catalyst (blue) are dispersed in a material. B: Damage leads to rupture of the microcapsules. C: Once the monomers and the catalyst are in contact, the monomers polymerize and heal the material (purple).

2.3. Silicones

To introduce silicones, at the beginning of this chapter a short introduction to the fundamentals of silicone rubbers is presented. Afterward the mechanical properties of elastomers such as silicones are described and the theory behind finite element simulations of elastomers is explained, as a major part of this thesis deals with the simulation of the mechanical properties of silicones.

2.3.1. Fundamentals of silicone rubbers

Silicone rubbers are crosslinked networks of polymer chains of the composition shown in Figure 2.15, where R can be methyl (CH_3), phenyl (C_6H_5), vinyl (C_2H_3) or trifluoropropyl ($C_3H_4F_3$) groups [86].

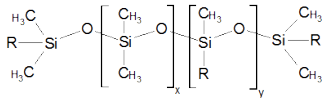

Figure 2.15: Chemical structure of silicone rubber. R can be methyl, phenyl, vinyl or triflouropropyl groups.

A well-known silicone rubber is polydimethylsiloxane (PDMS), where R is a methyl group. Silicone rubbers have special properties originating from the high bond strength of Si-O compared to C-C, providing the backbone of most other polymers. This results in, especially in case of PDMS, high thermal resistance, chemical stability, electrical insulation, non-toxicity, biocompatiblity and abrasion resistance. Other properties that are not common for all compositions of PDMS are optical transparency and high elongation at break [84, 86–88]. Most of the described properties of PDMS can be influenced by adjusting the polymer chain-length, the crosslinking degree and the filler amount and type [89–91].

In several commercial products siloxane polymer chains are cross-linked either by a catalyst driven addition reaction or by condensation [86, 87]. The two silicone rubbers used in this work are Sylgard 184 (Dow Corning, USA) and Elastosil RT625 (Wacker, Germany), which are both polydimethylsiloxanes that cross-link at room temperature via a platinum-catalyzed addition reaction. They are sold as two components where one component contains polymers with vinyl groups, the platinum catalyst and fillers and the other part contains polymers with Si-H groups [92–94]. Once these two components are mixed a cross-linking reaction takes place. The reaction scheme of the platinum catalyzed cross-linking reaction of PDMS is shown in Figure 2.16.

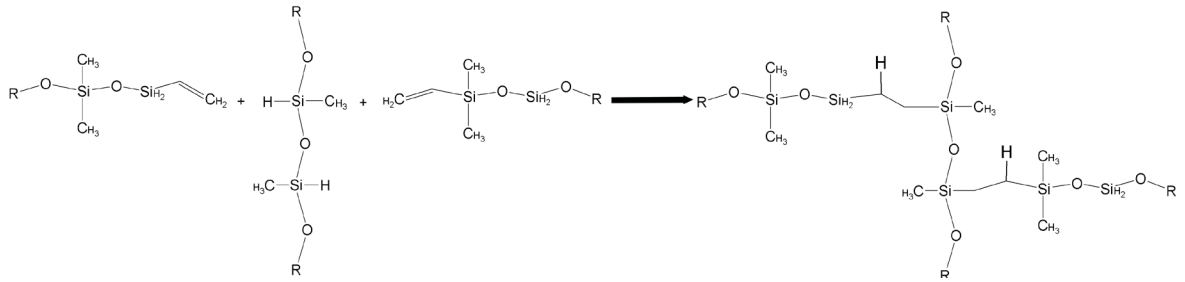

Figure 2.16: Reaction scheme of the platinum catalyzed cross-linking of PDMS. Chains with vinyl groups and chains with Si-H groups are cross-linked via an addition reaction.

The two silicones Sylgard 184 and Elastosil RT 625 are chosen as they each had desired behavior for the respective experiments in this thesis. Sylgard 184 is highly optically transparent and proven to be biocompatible [93]. It is used for cell experiments in this thesis. As its mechanical properties do not allow large deformations [95], it was not suitable for experimenting with strain-stiffening behavior. For these experiments, Elastosil RT625 was chosen. It is not optically transparent but it can be elongated up to 600% before break [87].

2.3.2. Mechanical properties of Elastomers

Later on in this thesis, the mechanical properties of strain-stiffening silicone samples are simulated via finite element analysis. An important parameter in these analyses is the allocated mechanical properties of the selected material in these simulations.

In materials science, it is common to describe the mechanical properties of a material with constants like the Young´s modulus introduced in chapter 2.2.2. The Young´s modulus can be derived from the linear stress-strain behavior of a metal or a ceramic and is a measure of its stiffness. The mechanical properties of polymers can be quite different from the properties of metals or ceramics. Especially elastomeric polymers show an extremely non-linear stress-strain behavior. The behavior in this case is called hyperelastic behavior. As the Young´s modulus is not sufficient to characterize this hyperelastic behavior, hyperelastic constitutive models are used for the description [96]. In the following, the stress-strain behavior of elastomers is presented first, then the hyperelastic constitute models are introduced.

Figure 2.17 shows the stress-strain behavior of the elastomeric PDMS Sylgard 184.

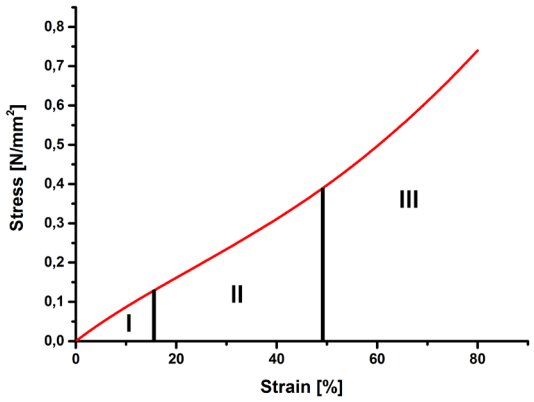

Figure 2.17: Exemplary stress-strain curve for an elastomer. Three regimes are marked (I, II and III). The first one is relatively stiff, the second one is softer and the third one is stiff again.

The stress-strain curve of this PDMS is governed by three regimes. The first one is influenced by a relatively stiff response of entangled polymer chains to a deformation. At higher strains (second regime) these polymers uncurl resulting in a lower stiffness as uncurled polymers provide less resistance and entanglement. This allows them to move more freely [97, 98]. In the third regime, the material becomes even stiffer as the polymer chains are fully stretched and the bond between single atoms is elongated [98].

There are also some structural requirements needed for a polymer in order to show such elastomeric properties. The material must be above its glass transition temperature, it has to have a low degree of crystallinity and it should be lightly crosslinked [99].

To describe the hyperelastic stress-strain behavior of an incompressible elastomer like silicone the Cauchy stress tensor is used:

$$\boldsymbol{\sigma} = 2\mathbf{B}\frac{\partial W}{\partial \mathbf{B}} - p''\mathbf{I} \tag{2.7}$$

The Cauchy stress tensor contains the left Cauchy-Green deformation tensor **B**, the strain energy density W, the identity tensor I and an arbitrary scalar parameter p'', which can be determined with the help of equilibrium conditions [100]. The strain energy density W and the left Cauchy-Green deformation tensor **B** are of particular importance here, as W depends on the invariants of **B** and each constitutive model defines a different relationship between W and the invariants of **B**. Before the constitutive models and their regarding strain energy density are described, the left Cauchy-Green deformation tensor and its invariants are shortly introduced.

If a solid is subjected to a deformation, the left Cauchy-Green deformation tensor is defined as:

$$\mathbf{B}=\mathbf{F}\cdot\mathbf{F}^{\mathbf{T}} \tag{2.8}$$

The tensor **F** describes the local gradient of the deformation. **B** has the following invariants:

$$I_1 = \mathrm{tr}(\mathbf{B}) \tag{2.9}$$
$$I_2 = \frac{1}{2}[\mathrm{tr}(\mathbf{B})^2 - \mathrm{tr}(\mathbf{B}^2)] \tag{2.10}$$
$$I_3 = \mathrm{det}\mathbf{B} \tag{2.11}$$

The invariants can also be written in terms of λ_1, λ_2, and λ_3 which are defined as the square roots of the eigenvalues of **B** and represent the principal stretches of the solid [100].

$$I_1 = \lambda_1^2 + \lambda_2^2 + \lambda_3^2 \tag{2.12}$$
$$I_2 = \lambda_1^2\lambda_2^2 + \lambda_2^2\lambda_3^2 + \lambda_3^2\lambda_1^2 \tag{2.13}$$
$$I_3 = \lambda_1^2\lambda_2^2\lambda_3^2 \tag{2.14}$$

If the solid is incompressible the third invariant I_3 is equal to 1.

In the following section, three of the over twenty existing constitutive models and their specific forms of the strain energy density W are presented and their advantages and disadvantages are briefly discussed. All models contain the invariants of **B**, which can be determined from the principal stretches during mechanical tests, and certain material constants, which can be calculated by fitting the constitutive models to the acquired mechanical test data. The following strain energy densities are written in a form describing incompressible material behavior, as this is the behavior most elastomers show.

One constitutive model is the neo-Hookean model, where the strain energy density W is defined to be [96, 101]:

$$W = \frac{\mu_1}{2}(I_1 - 3) \tag{2.15}$$

It contains the unknown material constant μ_1. It is relevant because it can be predicted that $\mu_1 = N\text{‘}k\text{‘}T$, relating the material constant with the number of polymer chains per unit volume (N‘), the Boltzmann constant (k‘), and the temperature (T) [96, 102]. This makes it suitable for the description of small deformations. A major disadvantage is that this model is not able to capture the stiffening of the material at high strains [101, 103].

A second model is the Mooney-Rivlin model with its strain energy density W [96, 100] defined to be:

$$W = \frac{\mu_1}{2}(I_1 - 3) + \frac{\mu_2}{2}(I_2 - 3) \tag{2.16}$$

This model contains the unknown material constants μ_1, μ_2. By introducing a dependency on I_2 the goal of the Mooney-Rivlin-Model is to increase the fitting sector of the Neo-Hooke model [101]. This model is also not able to capture the stiffening of the material at high-strains [102].

There are several further models that are able to increase the quality of the fit between test data and model, but the experimental data is required to be of elevated quality in order to determine valid material constants [104]. To obtain optimal experimental data three tests are necessary. The uniaxial tensile, the pure shear and the equibiaxial tensile test. These tests are supposed to be homogeneous but in practice this homogeneity is only assumed, which leads to a variance in material constants derived from each of the tests [105].

In order to bypass this challenge, new material models have been introduced that are sufficiently accurate in determining material constants with limited experimental test data. One of them is the Yeoh model. In this model the strain energy density W is defined to be [102, 104]:

$$W = \sum_{i=1}^{3} \frac{\mu_i}{2}(I_1 - 3)^i \tag{2.17}$$

This model contains the unknown material constants μ_1, μ_2, and μ_3. It has been shown that this model is able to describe the material behavior of rubbers quite well with only data available from uniaxial tensile tests [106].

The elastomeric materials used in this work show hyperelastic behavior and their mechanical properties are described by the Yeoh model.

2.3.3. The Finite Element Method

The method of choice for simulating the behavior of strain-stiffening structures is the finite element method (FEM). Relevant information on this method is given in this chapter. First, a motivation for the use of FEM and a general description of its working principle is given. Afterward, it will be explained how FEM works if a hyperelastic material is used.

The finite element method is a tool to solve engineering problems. Several engineering problems are described by differential equations. Their solution can in many cases only be found as an approximation. One method of finding these approximations is the finite element method. The idea of this method not to find a solution for the entire problem but to discretize it, which means separating it

in several parts, thus called finite elements. The finite element method can be used to model material properties such as the mechanical, electronic or magnetic properties. In this thesis, the mechanical response of a material is modeled. Figure 2.18 shows a strain-stiffening structure that is used later in this thesis and its representative in the simulation that has been separated into finite elements.

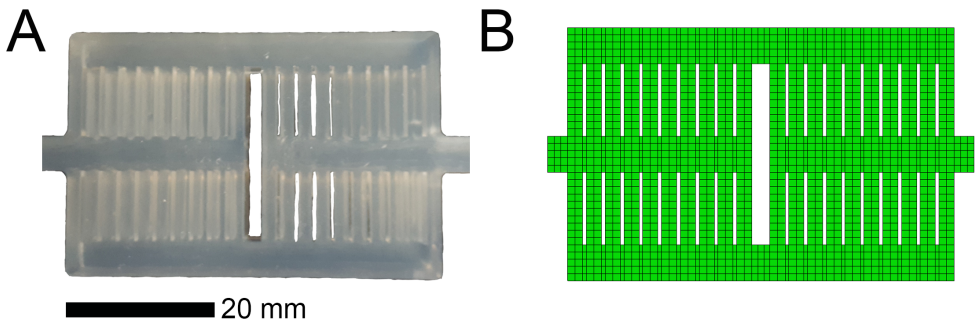

Figure 2.18: Geometrical structure (A) and its representative in the simulation (B). The structure was discretized and separated into finite elements. Each cube in (B) represents a finite element.

It is possible to define simple basis functions in each finite element, which are defined to be zero at each part of the analyzed body except for the section inside the element. Consequently, one element has only local influence and it is possible to calculate each element separately. The solution for the entire body can then be derived by setting up a system of equations that describes the entire body.

The process for a linear elastic problem will be explained in the following section. Afterward the concept is expanded for the solution of non-linear problems, allowing the simulation of elastomeric materials. The information in this chapter has been, if not marked, adapted from "Lineare und nichtlineare FEM" by Marcus Wagner [107].

As mentioned before, an engineering problem is first discretized. For each resulting finite element polynomial basis functions for the deformation $\tilde{\mathbf{u}}^e(\mathbf{x})$ are defined which, in the case of 3-dimensional problems, results in a matrix $\boldsymbol{N}_i$ for each node. Nodes are the points of connection between elements. The following rule is defined for the basis functions:

$$\boldsymbol{N}_i(x_j) = \begin{cases} \boldsymbol{I} \text{ for } i = j \\ \boldsymbol{0} \text{ for } i \neq j \end{cases} \tag{2.18}$$

Equation 2.18 states that the basis function equals one only at the site of the regarding deformation *(i=j)* and zero everywhere else.

The matrices $\boldsymbol{N}_i$ for each node are combined in a matrix $\boldsymbol{N}$ with the dimension:

$$Dim(\boldsymbol{N}) = [n_{df} \times n_{df} \cdot n_e] \tag{2.19}$$

where n_{df} is the number of degrees of freedom and n_e the number of elements. It connects the deformation of an element $\tilde{u}^e(\mathbf{x})$ and the displacement of the single nodes $\boldsymbol{u^e}$ via the relation:

$$\tilde{\boldsymbol{u}}^{\boldsymbol{e}}(\boldsymbol{x}) = \boldsymbol{N_I}(\boldsymbol{x})\boldsymbol{u_I^e} + \boldsymbol{N_J}(\boldsymbol{x})\boldsymbol{u_J^e} + \boldsymbol{N_K}(\boldsymbol{x})\boldsymbol{u_K^e} + \ldots = \boldsymbol{N}(\boldsymbol{x})\boldsymbol{u^e} \tag{2.20}$$

This connection is used to describe a continuous parameter, the displacement, by a function described by displacements at discrete nodes.

The same has to be done with the distortions and stresses. The strain and stress of an element can be described as

$$\tilde{\boldsymbol{\varepsilon}}^{\boldsymbol{e}} = \boldsymbol{D_\varepsilon}\tilde{\boldsymbol{u}}^{\boldsymbol{e}} = \underbrace{\boldsymbol{D_\varepsilon}\boldsymbol{N}(\boldsymbol{x})}_{\boldsymbol{B}(\boldsymbol{x})}\boldsymbol{u^e} \tag{2.21}$$

$$\tilde{\boldsymbol{\sigma}}^{\boldsymbol{e}} = \boldsymbol{C}\tilde{\boldsymbol{\varepsilon}}^{\boldsymbol{e}} = \boldsymbol{C}\boldsymbol{B}(\boldsymbol{x})\boldsymbol{u^e} \tag{2.22}$$

Where $\boldsymbol{D}_\varepsilon$ is a differential operator matrix and $\boldsymbol{B(x)}$ is a matrix that contains the derivatives of the basis functions with respect to global coordinates, and $\boldsymbol{C}$ describes the underlying material properties.

With the use of principles from the analytical mechanics field a simple description connecting the displacements, the material properties and the applied loads can be found. Where $\boldsymbol{K^e}$ is the stiffness matrix of a single element that contains the Matrix $\boldsymbol{C}$, $\boldsymbol{u^e}$ is the displacement of an element and $\boldsymbol{f^e}$ is the force acting on an element:

$$\boldsymbol{K^e u^e} = \boldsymbol{f^e} \tag{2.23}$$

In order to describe the entire problem, all element stiffness matrices are combined into one stiffness matrix $\boldsymbol{K}$. This matrix $\boldsymbol{K}$ connects the vector of the forces acting on all nodes $\boldsymbol{f}$ with the desired vector of the displacement of all nodes $\boldsymbol{u}$:

$$\boldsymbol{K}\boldsymbol{u} = \boldsymbol{f} \tag{2.24}$$

After defining suitable boundary conditions, the resulting system of linear equations can be solved.

This principle works well if all parameters like the kinematics, the stress-strain behavior of the ma-

terial, the equilibrium conditions and the boundary conditions behave linearly. If this is not the case, for example when the regarding stress-strain behavior of the material is highly non-linear, the approach has to be modified. This is the case for elastomeric materials. A strategy to modify the linear approach is based on using the principle of virtual work. Similar to the linear approach, it can be described via discretized relations. Consequently, a system of time-dependent equations can be derived:

$$\boldsymbol{M}\boldsymbol{a}(\boldsymbol{X},t) + \boldsymbol{t}(\boldsymbol{X},t) = \boldsymbol{f}(\boldsymbol{X},t) \tag{2.25}$$

Where $\boldsymbol{f(X,t)}$ represents the forces acting on the nodes, $\boldsymbol{M}$ is the mass matrix that contains information about the position of all nodes, $\boldsymbol{a(X,t)}$ is the vector of the accelerations at each node and $\boldsymbol{t(X,t)}$ the vector of internal node forces. The vector $\boldsymbol{t(X,t)}$ is defined as:

$$\boldsymbol{t}(\boldsymbol{X},t) = \int_{\boldsymbol{v}} \boldsymbol{B}^{\boldsymbol{T}}(\boldsymbol{\xi})\boldsymbol{\sigma}(\boldsymbol{X},\boldsymbol{v}',t)\boldsymbol{d}v' \tag{2.26}$$

With the Cauchy stress tensor $\sigma\boldsymbol{(X,}\nu\boldsymbol{',t)}$ known from equation 2.7 and the velocity ν' and the natural coordinates ξ.

The vector of internal node forces $\boldsymbol{t(X,t}$) contains the information about the geometrical and physical non-linearity of the system. The Cauchy stress tensor of hyperelastic materials, for example, is not linear as it was shown in chapter 2.3.2. In case of large deformations, the loads acting on the body are also not constant. Caused by the large deformation, the direction of how the forces act on the body is changed. Consequently, the vector of internal node forces depends on the degree of deformation, which makes it impossible to directly determine the state of equilibrium after a certain deformation. Insted, the problem has to be separated into time steps. All changes in the state of the material between the beginning and the end of a time step have to be calculated. There are two methods to do this. An explicit and an implicit method.

In the explicit method, the vector of internal node forces $\boldsymbol{t(X,t)}$ is calculated for each step and the updated version is used for the next step. In the implicit method, an iterative solving method like the Newton-Raphson method is used to linearize the problem. At each time step, an equilibrium of the internal structure force with the externally applied loads is derived iteratively. For each iteration, the so-called tangent matrix ($\boldsymbol{K}_T$) is calculated, which replaces the stiffness matrix known from linear problems and contains information about the non-linear material properties and variations in forces due to large deformations.

Each of the two methods has certain advantages and disadvantages. The iterative method is time- and memory consuming as a tangent matrix has to be calculated for each time step. In comparison in the

explicit method, a solution for each time step can be provided directly. The explicit method, on the other hand, has problems with instability in the simulation and an effect called “hourglass modes”, an effect where elements of a model can deform in a physically not possible manner. To avoid these problems sufficiently small time steps and special stabilizing mechanisms need to be used [108–110].

3. An artificial extracellular matrix

For the prevention of *Acanthamoeba*-borne diseases, it is necessary to understand the amoeba's movement in confined conditions and to be able to control it.

Acanthamoebae can be found in nature in two states: In an active trophozoite state and in a dormant cyst state [28]. For the following experiments, only the active trophozoite state is important, as this is the state where *A. castellanii* is pathogenic. The phrases trophozoite, cell, and *A.castellanii* will, therefore, be used synonymously in the next chapters.

Trophozoites of *A. castellanii* migrate through body tissue that is composed of cells and extracellular matrix molecules. These molecules form a network with pores that confine the movement of intruding cells. In order to recreate these confinements, micro-pillar arrays have proven to be suitable [111].

In this series of experiments, silicone micro-pillars are used to represent the confinement of the extracellular matrix inside body tissues. Micro-pillar arrays have several beneficial properties for this kind of analysis, as their structure is only quasi-three-dimensional: Cells migrating through such structures are confined on the bottom and on the sides. While it might be a disadvantage that the cells are not confined on the top, the open structure allows a constant supply of nutrients and easy observability of the cell behavior with a phase-contrast microscope. The observability is supported by the optical transparency of PDMS Sylgard 184 that was used for this experiment. Another beneficial property is that the gap-size between all pillars is the same. This allows repeated observability of cell behavior at constant conditions. A scanning electron microscopy picture of such a micro-pillar array is shown in Figure 3.1A.

Two major aspects are analyzed in this chapter: the general behavior of *Acanthamoebae* inside these structures and their behavior inside the structures after the cell had ingested micro-particles of defined size and shape. The experimental approach is sketched in Figure 3.1B-E. For the experiments with particles, the highly phagocytic nature of *A. castellanii* trophozoites was exploited, as it allows the cells to ingest extracellular targets such as blood cells or micron-sized beads [112, 113]. Three types of microparticles were used: spherical particles with a diameter below the gap-size between pillars, spherical particles with a diameter above the gap-size between pillars, and cylindrical particles with a diameter below the gap size and a length above the gap-size between pillars. The goal to come up with methods to trap *A. castellanii* motivated the study of the cell´s behavior after ingesting particles. A successful trapping could prevent *Acanthamoeba*-born diseases by inhibiting a transmission of the cell to the host.

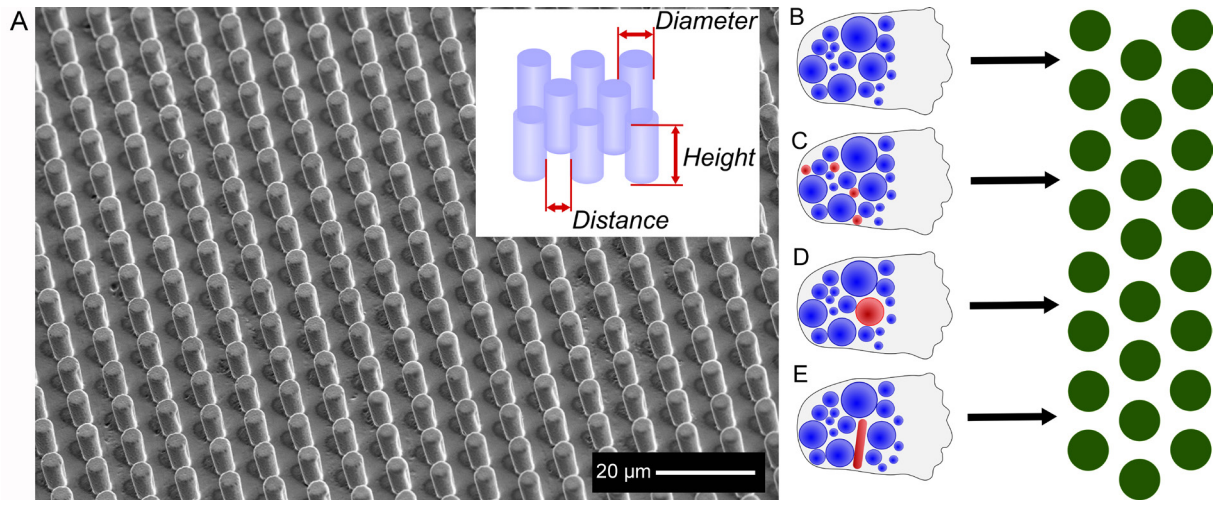

Figure 3.1A: SEM image of the micro-pillar array. The distance between the sidewalls of the pillars is 5.5 µm. The height of the pillars is 10 µm and their diameter is 4.5 µm. B-E: Sketches of *A. castellanii* with vacuoles inside (blue) before entering a micro-pillar structure (green). B: No ingested particles. C: Ingested particles (red) with a diameter below distance between pillars. D: Ingested particle (red) with diameter above distance between pillars. E: Ingested cylindrical particle (red). The diameter is below the distance between pillars. The length is above distance between pillars.

The experiments in this chapter are part of a manuscript by me, Nils Lukat, Lindsay P. Schneider, C. Wyatt Shields IV, Gabriel P. López and Christine Selhuber-Unkel with the title "The phagocytic catch in constricted environments: cells between logjam and problem solving". My contribution to the manuscript was the production of the microstructures, the conceptual design and the supervision of the cell experiments conducted by Lindsay P. Schneider, the evaluation and processing of the results and a major part of the scientific writing. Lindsay P. Schneider and I worked in the lab of Christine Selhuber-Unkel. Wyatt Shields produced the cylindrical particles in the lab of Gabriel López. The contribution of Nils Lukat that focuses on intra-cellular mechanisms is not part of this thesis.

To provide a smooth reading experience, results are provided and directly discussed. Materials and Methods are described at the end of this chapter.

3.1. Results and discussion

The results of the experiments with *A.castellanii* are separated into two sub-sections. The first one deals with the general behavior of *A.castellanii* inside the micro-pillar arrays and the second one deals with their behavior after phagocytosing artificial cargo.

3.1.1. Migration behavior of *A. castellanii* in micro pillar arrays

To observe the migration behavior of *A. castellanii* trophozoites, a microenvironment of PDMS micro-pillars was used. The pillar arrays were produced via a PDMS micro-molding process and provided a defined wall-to-wall distance of 5.5 µm between neighboring pillars as well as a height of 10µm and a diameter of 4.5 µm. The wall-to-wall distance was chosen to be in the range of the larger vacuoles in the trophozoites and in the range of the gap size in the extracellular matrix [60]. The cells were not only observed inside the structure but also, as a control, outside the structure on flat PDMS.

Special focus was set on the vacuole size and the cell´s morphology inside and outside of the structure on flat PDMS. Figure 3.2 shows the results of the experiment. One representative example of a cell outside the structure (Figure 3.2A) and one sample of a cell inside the structure (Figure 3.2B) are presented. It can be observed that the vacuole diameter is smaller inside the structure than outside. Quantitative results from the measurement of the largest vacuole's diameter of 100 cells inside and outside of the structure support this observation (Figure 3.2C). While the largest diameter of the vacuole that could fit between two pillars is about 5.5 µm, the largest possible diameter that would fit in the triangle between three pillars is around 7 µm. Except for one outlier, which was probably due to an out-of-focus image, all diameters of vacuoles of the cells inside the structure were below 7 µm and most of them even lied below 5.5 µm.

It is interesting to mention that trophozoites not only change the size of the vacuoles when they move inside the pillars but, they also change their shape. On the flat PDMS outside of the structure, they were mostly found in a roundish to an elliptical shape. Inside the structure, the shape was more elongated with a serpentine-like outline.

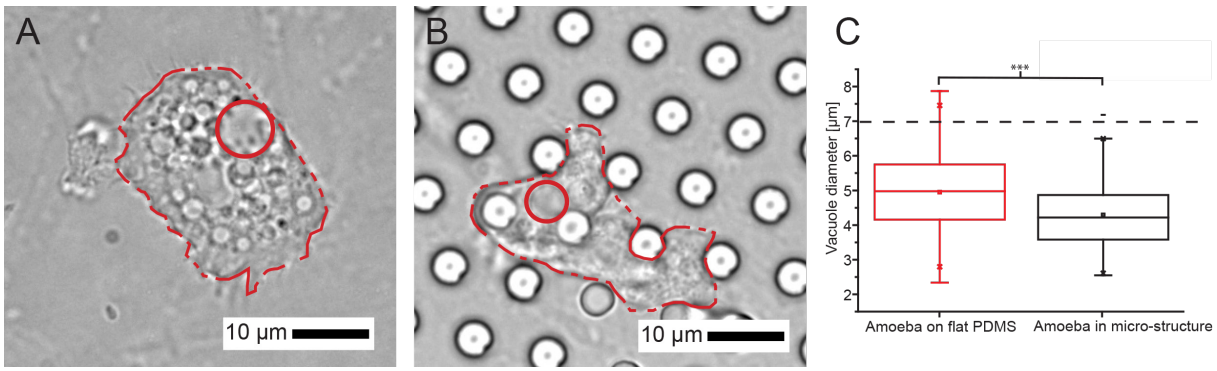

Figure 3.2: Phase contrast microscopy images of representative *A. castellanii* trophozoites. A: on a flat PDMS substrate. B: On a PDMS substrate with micro-pillars. The dashed red line marks the outline of the trophozoite, while the continuous red line marks the outline of the largest intracellular vacuole. The cells are rounder on the flat PDMS substrate than on the micro-patterned surface, where the cell is spread between the pillars in different directions. Inside of the micropattern, the size of the vacuole is limited by the maximum size of the interior circle fitting in between the pillars. C: The boxplot shows a significant difference between the size of the largest vacuoles inside and outside the micro-pillar array (box: interquartile range; line in each box: median; dot: mean; whiskers: minimum/maximum, Student´s t-test: $p < 0.001$, *).**

From these observations, it can be concluded that the cell adapts its vacuoles´ diameter to the available space. In other cell types, not the vacuoles but the nucleus is the largest structure and defines the behavior of a cell towards spatial confinement [66]. Studies have shown that even though the nucleus is relatively stiff, its size can be adapted by opening and resealing it if the cell moves through narrow gaps [60]. A similar behavior can be observed by *A. castellanii* as it adapts the size of the largest vacuole, to the size of the confinement and is, therefore, able to intrude the structure and freely move inside. As *A. castellanii* naturally moves in confined conditions [28] the ability to adapt internal obstacles (like the vacuole size) to external obstacles (like the pores of the extracellular matrix) seems to be necessary. The size of the vacuoles can also be influenced by other factors than the geometry. It has been reported that the motility of cells can be influenced by the adhesiveness of the substrate and the stiffness and contractility of the cell [114]. As the determination of these parameters were not a part of the experiments, it cannot be concluded that they are the same inside and outside of the structure. A difference of these parameters between the inside and the outside of the structure could also be a reason for an adaption of the vacuole size.

In addition, the shape of the trophozoites was adapted to the structure. The elongated shape of the cell with a serpentine-like outline inside the micro-pillar array can also be found in other cells in micro-structured assemblies and is most likely based on the maximization of the contact area between cell and surface [115].

3.1.2. Influence of phagocytosed particle on the migration behavior of *A. castellanii*

Another interesting parameter to investigate is the behavior of *A. castellanii* after the ingestion of stiff artificial particles in the micrometer range. These particles had different geometries so that the impact of their size and shape on the cell´s motility inside the micro-pillar arrays could be investigated.

The first question that should be answered in this series of experiments was: can the cells still migrate, although they contain particles whose size the cell cannot actively adapt? In the first series of experiments, *A. castellanii* phagocytosed either spherical particles with a diameter of 3 µm, which is below the distance between neighboring pillars or 6.7 µm, which is above the distance between neighboring pillars. The influence of the motility of such particle-containing cells inside the structure was compared to cells without additional particles. Figure 3.3 shows the position of representative cells after an observation time of 0 s and 300 s. If the diameter of the particle was smaller than the wall-to-wall distance between pillars, the particles did not hinder the movement of the cell. The cells were able to migrate inside the structure similar to the cell without phagocytosed particles (Figure 3.3A, B). If the particle was larger than the wall-to-wall distance between pillars the motility of the cell was hindered, as the size of the particle could not be adapted to the gap size between pillars (Figure 3.3C).

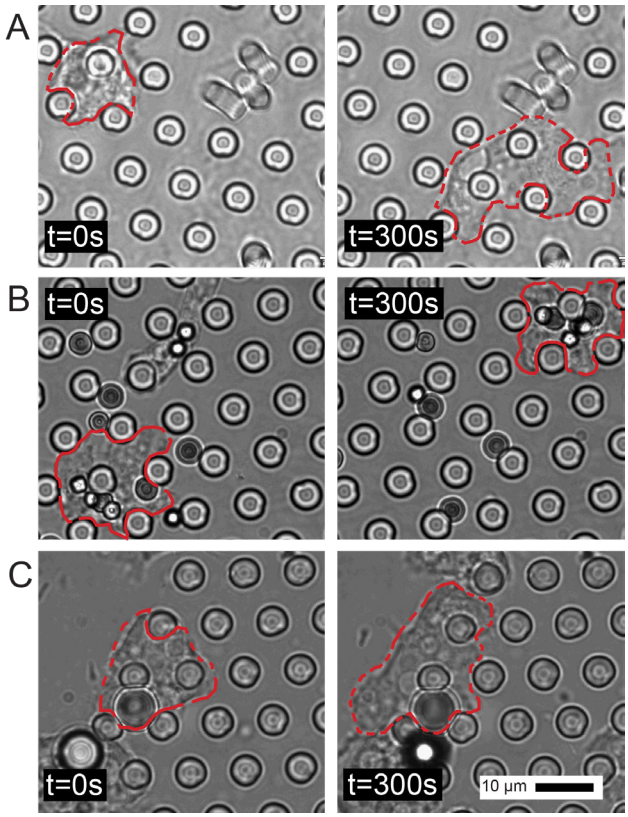

Figure 3.3A: *A. castellanii* inside the micro-pillar array without particles. B: The cell with particles smaller than the pillar gap C: The cell with particles larger than the pillar gap. In all three situations, cell shape adapts to the micro-pillar array and the snapshots at 0 and 300 s demonstrate that cell migration is strongly hindered in C.

Cells that had phagocytosed particles with a larger diameter than the wall-to-wall distance were completely hindered in their migration in most cases, but some cells showed highly interesting problem-solving strategies. All observed strategies are shown in Figure 3.4.

The first strategy is presented in Figure 3.4A. A cell with a phagocytosed particle approached the structure from outside. The cell entered the structure and the particle that did not fit inside the structure is gradually pushed to the back as an increasing part of the cell entered the structure. After a certain time, the cell changed its direction of movement and migrated outside of the structure. Hence, the cell decided to not enter the structure. In the following strategies, the cells found ways of entering the structure like presented in Figure 3.4B. The behavior of the cell was similar to the one of the first case until the point where the particle was completely pushed to the back of the cell. In this strategy, the cell ejected the particle and moved inside the structure, while the particle remained outside of the pillar array. The next strategy exploits the fact that the pillar structures are not closed on the top. The cell carried the particle above the pillars which allowed it to move inside or on top of the structure. The lifting of the particle can be observed in Figure 3.4C as the particle leaves the focal plane, is moved above pillars and brought back to the focal plane. In Figure 3.4D the last observed strategy is shown. In this strategy, the cell dragged the particle through the gap between neighboring pillars. It applied a force to the particle which leads to a significant bending of the flexible PMDS pillars. The bending increased the distance between the pillars and the particle could be pulled through. From the displacement of the pillars an estimation of the force applied by the cell could be made. The pictures indicate that each pillar is deformed by a distance of ~0.55 µm. The two-dimensional pictures acquired do not allow the determination of the exact height of the contact point between the particle and the pillars above the surface, but it can neither be below the radius of the bead (3.35 µm) nor above the height of the pillar (10µm). From this estimation, a minimal and a maximal bending force of 75 nN (contact at 10 µm) and 920 nN (contact at 3.35 µm) can be calculated. It can be estimated that the pushing force the cell applied to the bead was in the range of several 100 nN, as the contact between the pillars is presumably a continuum contact. None of the observed strategies for the problem solving was preferred.

The first two strategies presented show two completely opposing strategies. In the first strategy, the cell´s drive to enter the structure was not large enough to exocytose the particle. It rather stayed outside of the structure. In the second strategy, the cell entered the structure and exocytosed the particle. Studies have shown that *A. castellanii* preferred a structured sample to a flat sample [116] and that it tends to eject artificial particles if it is preferable for its natural behavior [117]. This would in principle explain an increased tendency towards the second problem-solving strategy. Still, no preference towards the ejection of the particle has been observed.

The other two strategies provided remarkable information about the abilities of *A.castellanii*. Being able to transport the particle above the pillar array to avoid the confinement shows that the trophozoites can detect free space above them and are able to reposition the cargo accordingly. Being able to drag the particle through the gaps between pillars, even though it was initially smaller than the

particle shows that the trophozoites are able to apply forces in the range of several 100 nN on phagocytosed objects. Forces in a similar range have been measured for cardiomyocytes in micro-pillar structures [118].

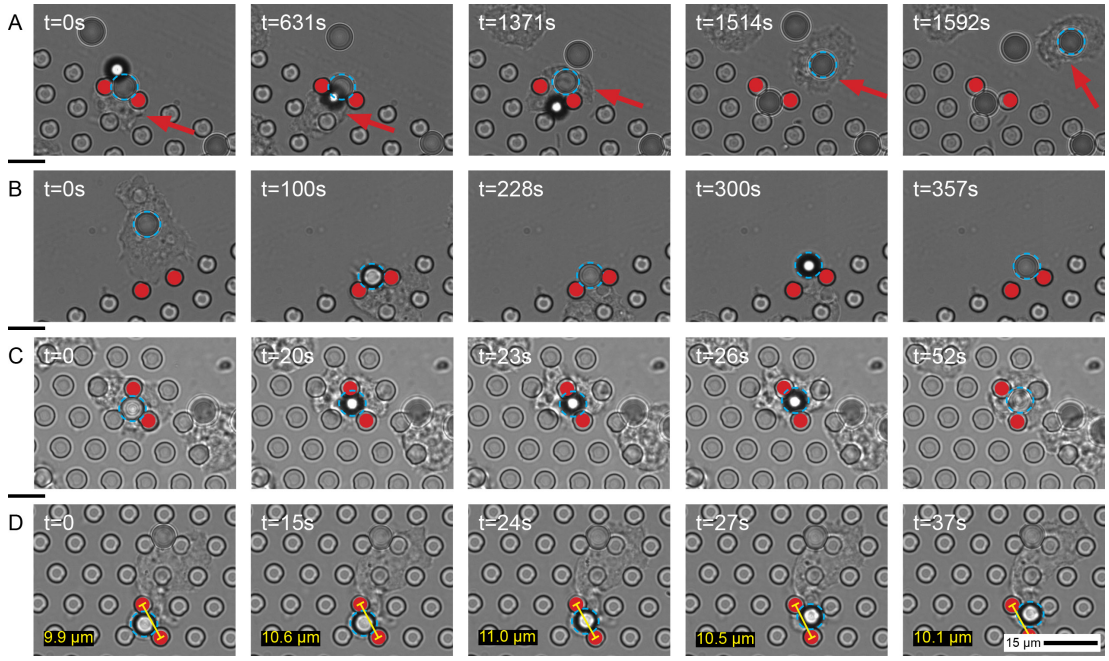

Figure 3.4: Strategies of *A. castellanii* to bypass micro-pillar structures after phagocytosing a particle larger than the gap between the two pillars. Each row shows snapshots at different time points for a different cellular strategy. To aid in visualization, the pillar constrictions of interest are marked with red circles. The particles of interest are encircled with a blue dotted line. A: The cell does not enter the structure (red arrow indicates the position of the cell). B: The cell ejects the particle. C: The cell carries the particle over the structure. D: The cell pulls the particle through the opening by exerting forces. The size of the pillar gap is marked by yellow lines and its length is given

A. castellanii is also able to phagocytose cylindrical particles. The particles used here had a diameter of 2 µm and a length of 10 µm. Hence, their diameter lied below the wall-to-wall distance between pillars, but their length lied above this distance. Three strategies how cells transported these particles through the pillar structure were observed. They are presented in Figure 3.5.

In the first strategy, the lateral surface of the particle stayed parallel to the array surface, while the particle was guided through the opening between two pillars with its short diameter leading ahead (Figure 3.5A). In the second strategy (Figure 3.5B) the pillar was turned such that its lateral surface changed from being parallel to the array surface to being perpendicular. In this position, its diameter was below the wall-to-wall distance between two neighboring pillars. Consequently, it could be guided easily through the gap between the pillars. Afterward the pillar was turned again until its lateral surface was parallel to the array surface. In the third strategy, the particle is carried above the pillar structure while its lateral surface stayed parallel to the array surface (Figure 3.5C). This strategy was similar to the strategy with spherical particles presented in Figure 3.4C.

Other than in the experiments with spherical particles, in these experiments, a preference for a

certain problem-solving strategy was observed. Most of the cells (about 92%) guided the particle parallel to the array surface (Figure 3.5A) through the structure instead of carrying it above. It was additionally observed that the mechanism of guiding the sample through the pillar array is directed and organized and not by a trial and error approach.

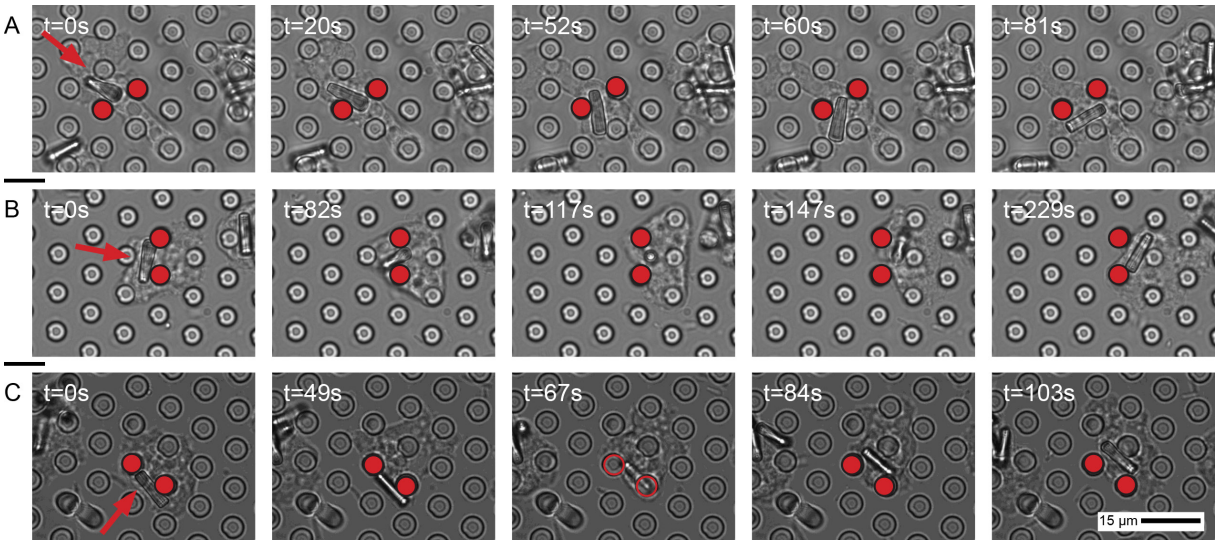

Figure 3.5: Methods of transportation of *A. castellanii* through the micro-pillar array after phagocytosing a cylindrical particle with a diameter smaller than the gap between pillars, but a length larger than the gap. Three different scenarios were observed. A: The cell guides the cylinder through the structure by turning it parallel to surface (oriented in the direction of motion). B: The cell turns the cylinder perpendicular to the surface before guiding it through the pillars. C: The cell carries the cylinder above the structure.

The fact that *A. castellanii* trophozoites are able to guide the particles in a directed and organized way indicates that they might have a mechanism for sensing the orientation of the pillars. Active sensing of geometrical features has already been discussed in cell adhesion and in the context of the cytoskeleton´s, ability to sense local cell geometry [119, 120]. The ability of cells to solve complex problems has been discussed in the context of cell memory and biochemical processes [121]. These studies and the presented findings show that a cell acts as an intelligent and active system.

3.2. Conclusion

The data provided in this chapter demonstrated that *A. castallanii* is able to adapt to constricted environments and that the migration of *A. castellanii* in constricted environments can be controlled by the size and the shape of phagocytosed micro-particles. These observations could serve as a basis to come up with a new strategy to prevent *Acanthamoeba*-born diseases: Specifically designed artificial microenvironments could be combined with the phagocytosis of synthetic particles, to generate novel filtering or cleaning devices, as the cells are then trapped in the material. Such devices would represent a purely material-based approach where no chemoattractants would be needed.

The presented results might also have an influence on the research on other pathogenic microorganisms that migrate through dense body tissue. Finding strategies to prevent the migration might be a key to novel therapeutic approaches against diseases caused by these microorganisms.

3.3. Materials and methods

3.3.1. Sample preparation

To produce the micro-pillar arrays first a template was produced in a lithography process and afterwards, PDMS was molded in this array and removed to form the pillars. The general procedure is shown in Figure 3.6, while details are described in the next two sub-chapters.

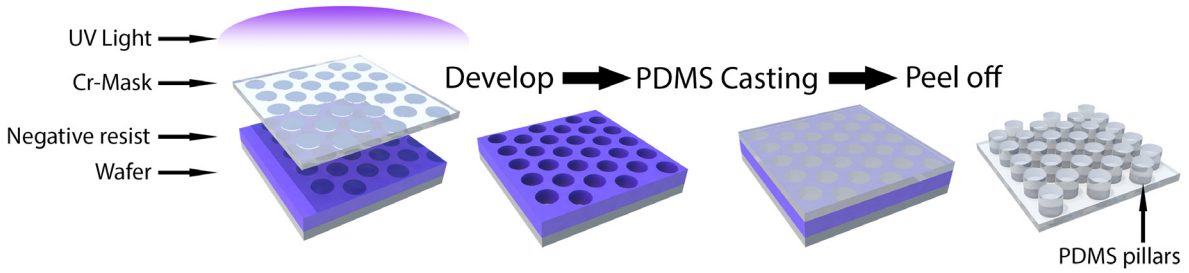

Figure 3.6: Sketch of the steps for the production of PDMS micro-pillar arrays. First, a template is produced by coating a wafer with a negative photoresist. The thickness of the resist defines the length of the pillars. The resist is cured through a chromium mask via UV-light. The chromium mask is transparent except for circles in a hexagonal pattern. Parts that were not cured by the UV light are washed away from the wafer in a developing step leaving holes at the places of the circles on the chromium mask. In a second step, PDMS is cast on the template. After curing the PDMS, a layer with micro-pillars can be peeled off.

3.3.1.1. Template production

A common method to produce molds with micro meter sized features for PDMS-micro-molding is the use of SU-8 photoresist. This negative photoresist can be applied to Silicon wafers in variable thicknesses between 1.5 and 200 µm [122]. This resist layer can be structured via photo-lithography techniques, where the parts of the resist that are exposed to light stay on the wafer and the other parts are solvable. This results in a mold that has the depth of the thickness of the resist and features according to the photomask that was used [123].

For the production of the template the following procedure was used, which was derived from the product datasheet of the photoresist [122]. As this is just a general guideline, certain steps were modified to achieve a high-quality mold for micro-pillars with the available equipment.

The procedure started with a 4 in. silicon wafer (1 0 0) with a thickness of 525 µm. After a prebake for 5 minutes at 200°C on a hotplate and 10 minutes of cool down on a metal plate at room temperature, the wafer was spin-coated with 4 ml of photoresist (SU-8, MicroChem Corp., USA). This was done in two steps: First, five seconds at 500 rpm (ramp of 100 rpm/s) and second 27s at 2000 rpm (ramp of 3000 rpm/s), resulting in a film thickness of 10 µm. This coating was followed by a soft-bake at 65°C on a hotplate for two minutes and at 95°C for 5 minutes. The wafer stayed on the hotplate for the time the hotplate took to heat from 65°C to 95°C. The soft bake was followed by 5 minutes of cool down time on a metal plate at room temperature. Afterward it was exposed to UV light at 1500 mJ/cm^2 in a mask-aligner (MA6/BA6, Süss Microtec, Germany) through a chromium mask that featured full circles in a hexagonal pattern, with a spacing of circle centers of 10 µm and a diameter of 4.5 µm. The exposure was followed by a post-exposure-bake as in the soft-bake, with 1 minute at 65°C and 2 minutes at 95°C. To dissolve unexposed resist the wafer was washed in SU-8 Developer (MicroChem Corp., USA) for 3 minutes, rinsed wit propan-2-ol (Sigma-Aldrich Chemie GmbH, Germany) and blow-dried with nitrogen. After a baking step at 200°C on a hotplate for 5 minutes to harden the resist, the wafer was cut into approximately 1x1 cm^2 pieces including 3x3 mm^2 areas of the desired features.

3.3.1.2. Polymer molding

PDMS, a silicone often used in micro-molding [124] and cell experiments [125] is used for the production of micro-pillar arrays. It features optical transparency and biocompatibility.

To prevent sticking of the PDMS to the template, it was silanized with Trichloro(1H,1H,2H,2H-perfluorooctyl)silane (Sigma-Aldrich Chemie GmbH, Germany) by placing 2 droplets of the silane solution onto a spare wafer piece and placing it with the template in a desiccator under vacuum for 2 hours. PDMS pre-polymer solution and curing agent were prepared in a 10:1 (w/w) ratio (Sylgard 184, Dow Corning, USA). Before pouring a small droplet on a glass slide it was degassed for 1 hour

in a desiccator to remove trapped air. A template, as described in chapter 3.3.1.1, was placed on the polymer with the microstructure facing downwards. To achieve a thin layer of PDMS between the template and the glass slide gentle pressure was applied to the template. In order to release the air form the template and force the PDMS inside the features, it was degassed in a desiccator for 10 minutes. The sample was cured in an oven for 1 hour at approximately 65 °C. Directly after the curing, the template was removed from the PDMS with plastic tweezers. Previous studies have shown that it is necessary to remove the template while the sample is still warm [126]. As the thickness of the resist during template preparation was chosen to be 10 µm, the resulting pillars had a height of 10 µm, too. The polymer molding procedure was developed together with Sören Block [126].

3.3.2. Micro-particle solution preparation

For the experiments, three types of microparticles were used: Polystyrene microspheres with a diameter of 6.7 µm (PC-S-6.0, Kisker Biotech GmbH &Co. KG, Germany) and with a diameter of 3 µm (CAT# 17145, Polysciences, Inc., USA), as well as cylindrical SU-8 particles with a diameter of 2 µm and a length of 10 µm. The latter were produced for these experiments by our collaborator Wyatt Shields according to a previously published procedure [127, 128]. Micro-particle suspensions were made by taking either 200 µl of stock polystyrene particle solution and mixing it with deionized-water in a 1:4 (v/v) ratio or by taking 25 µl of SU-8 microcylinder solution and mixing it with deionized-water in a 1:9 (v/v) ratio. After centrifuging the suspensions for 15 minutes with 6,236 x g in a centrifuge (Mikro 220r, Andreas Hettich GmbH & Co.KG, Germany), the liquid was replaced with 1 ml deionized-water. This step was repeated two more times. After the third centrifuging step, the water was replaced with 200 µl Peptone Yeast Glucose 712 medium [129], which is the medium used for the cell experiments.

3.3.3. *Acanthamoeba* experiments

Trophozoites of *A. castellanii* (ATTC 30) were cultured in Peptone Yeast Glucose 712 medium at room temperature in 75 ml tissue culture bottles (Sarstedt, Germany), as described elsewhere [129, 130]. A PDMS micro-pillar array was placed onto a glass bottom Petri dish (ibidi GmbH, Germany) for each experiment. In each dish, depending on the experiment, either 100 µl of a solution containing spherical particles or 200 µl of the solution containing cylindrical particles, or no solution was added. Additionally, 20,000 trophozoites of *A. castellanii* in 1 ml of Peptone Yeast Glucose 712 medium were added to the dish and were allowed to rest for 15 h to ensure a sufficient uptake of particles by the cells and a sufficient wetting of the hydrophobic PDMS structure by the medium. The migration of the trophozoites was observed and documented with a 60x oil immersion objective (UPlanSApo 60x Oil, Olympus, Japan) on an inverted microscope (IX-81, Olympus, Japan) and a digital camera (Hamamatsu C9300, Hamamatsu, Japan). In total 33 movies, each at a recording frequency of 10 fps, were obtained.

3.3.4. Calculation of pillar bending forces

To calculate the force A. castellanii applies on the bead that leads to a bending of the pillars, elementary beam theory was used, as the pillar can be described as a beam with a circular cross-section. As pillars are attached to a soft substrate, that also deforms in response to pillar bending, a correction factor proposed by Schön et al. was taken into account [131]. The correction factor represents a reduction of bending force due to deformation of the substrate. The material properties of the PDMS micro-pillars were taken from other sources. The following equations were used to calculate the force the cell applies on the bead F_{Cell}:

$$F_{Cell} = 2F \tag{3.1}$$

$$F = corr \times k_{bend}\delta \tag{3.2}$$

$$corr = \frac{\frac{16}{3}\left(\frac{L'}{D''}\right)^3}{\left(\frac{16}{3}\left(\frac{L'}{D''}\right)^3 + \frac{7+6\nu}{3}\frac{L'}{D''} + 8T_{tilt}(\nu)\left(\frac{L'}{D''}\right)^2\right)} \tag{3.3}$$

$$T_{tilt}(\nu) = a\frac{(1+\nu)}{2\pi}\left\{2(1-\nu) + \left(1 - \frac{1}{4(1-\nu)}\right)\right\} \tag{3.4}$$

$$k_{bend} = \frac{3\pi E D^4}{64L^3} \tag{3.5}$$

In these equations δ represents the displacement of the pillar, L' represents its length and D'' its diameter (4.5 µm). E is the Young´s modulus of the PDMS (E=1.72 MPa from [132]), ν is the Poisson´s ratio of PDMS (ν=0.5 from [133]), and a is a fitting parameter (a=1.3 from [131]).

The displacement was determined from the acquired pictures and yielded 0.55 µm and the length of the pillar was set to be either 10 µm or 3.35 µm because this is the maximum and the minimum height the particle can apply a deformation on the pillar, as sketched in Figure 3.7

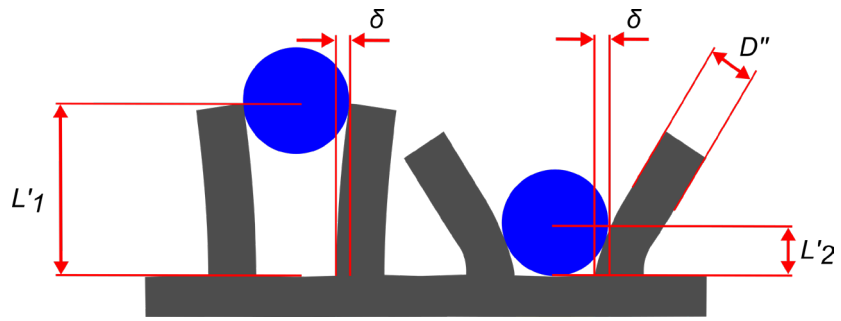

Figure 2.7: Sketch of the two extrema on how a spherical particle (blue) can deform pillars (grey). On the left, the particle deforms the pillar on the highest possible point. In this case the length of the pillar that is used in the equation to calculate the bending force is the full length of the pillar L'_1. On the right, the particle deforms the pillar on the lowest possible point. In this case the length of the pillar that is used in the equation to calculate the bending force is L'_2, which is equal to the diameter of the particle. In the sketch also the displacement of the pillar δ and the diameter D'' of the pillar are marked.

3.3.5. Image analysis and statistical analysis

The distance between pillars and the diameter of the largest vacuole inside the trophozoites was determined with Image J 1.50 (National Institutes of Health, USA). The significance testing of the difference between vacuole sizes was conducted via a two-sample t-test in Origin 9.1 (OriginLab, Northampton, USA).

4. A strain-stiffening structure

The cell´s active stiffening mechanism is an interesting mechanism that is worth to be mimicked for the development of strain-stiffening materials. The goal of this part of the thesis was not only to mimic this mechanism but also to come up with a strain-stiffening material that does not have any of the downsides of conventional strain-stiffening materials listed in chapter 2.2.2. Copying the strain-stiffening behavior of the cell is a novel approach and therefore, a major part of this work was the development of general concepts, the transition of concepts into experiments and the optimization of these concepts towards the following requirements: material independency, speed independency, reversibility and stiffening upon elongation.

In this chapter three approaches that had a major influence on the final solution are shortly presented, followed by a detailed description of the final strategy to produce strain-stiffening elastomers. In order to ensure a smooth reading experience, the results are shown and directly discussed, while materials and methods are described later on.

4.1. Experimental approaches to strain-stiffening materials

The general idea in all concepts was to mimic the cell´s active bundling of actin filaments into stress fibers. This bundling leads to a higher degree of cross-linking inside the cytoskeleton and consequently to a higher stiffness (see chapter 2.1.4). While cross-linking is triggered biochemically in a cell, our approaches induce it through the deformation of a specifically structured material. These structured material had to contain certain structural features that change their distance to each other upon deformation. The main challenge was to increase the cross-linking of a material in response to an elongation, as it can be observed that features that are close to each other tend to move apart when being elongated.

One concept exploits the fact that parallel lines decrease their distance when tilted, as shown in Figure 4.1A. Consequently, an elongation of the material in form of shearing brings structural features closer to each other, thus leading to a surface-to-surface interaction that can have the same effect as cross-linking.

To convert this concept into a strain-stiffening mechanism, a series of parallel channels was introduced into a sample. Inside these channels were spheres with diameters smaller than the distance between the channel walls, thus providing clearance between sphere and channel wall. Shearing of such structures leads to a decrease of the wall-to-wall distance and to a clamping of the spheres between the walls. A sketch showing the general principle of this approach is provided in Figure 4.1B.

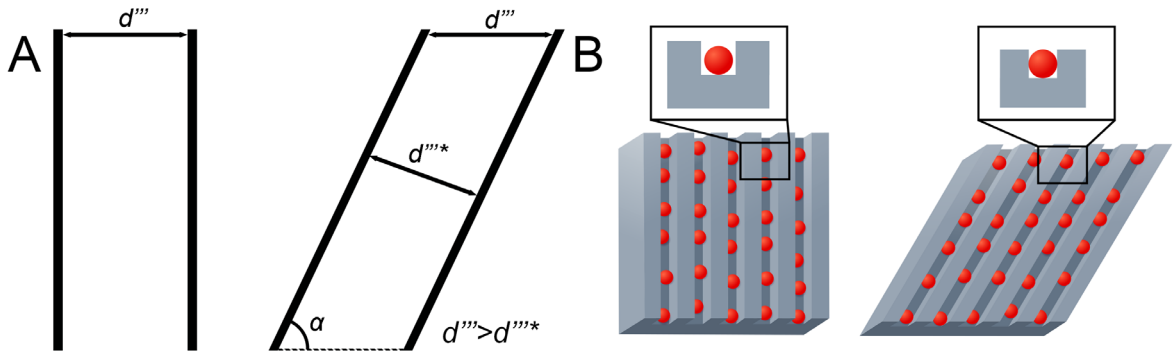

Figure 4.1 A: Two parallel lines have a distance *d'''*. If they get tilted by an angle α, their distance is reduced to *d'''*=sinα*d'''*. B: Sketch of spheres inside channels of an approach of a strain-stiffening material. As shearing motion decreases the distance between channel walls, beads get clamped between the walls. This should increase its stiffness.

When realized in an experiment, the surfaces of the sample and the spheres were additionally chemically functionalized. The goal was to achieve a strong but reversible binding between the spheres and the channel walls that should result in a reversible strain-stiffening due to the increased cross-linking of the structure. For the chemical functionalization, the binding system of biotin and streptavidin was chosen as it is one of the strongest non-covalent binding systems [134]. Even though it is not really reversible it was chosen for a proof of principle. The functionalization method was developed together with Supattra Paveenkittiporn [135]. For further experiments, other reversible binding systems like concanavalin A and mannose carbon hydrates [136] or systems known from self-healing polymers [137] could be used.

Part of the strategy was to use structured materials in the micrometer range to exploit the effect of the biological binding systems and to introduce the structures in a macroscopic sample. In this way, the characterization of the mechanical properties of the sample could be done with a custom-made tensile test setup that measured forces in the millinewton to newton range and applied deformations in the millimeter range. The tensile test setup was modified such that it was able to apply a shear force on the sample. The distance of the clamps perpendicular to the direction of shearing was held constant. This setup was also developed together with Supattra Paveenkittiporn [135]. The channels were kept in an aqueous atmosphere during the test, as this is necessary for the working principle of the biotin-streptavidin binding system [138]. The sample was made using PDMS micro-molding with Sylgard 184, as functionalization and micro-structuring techniques for this material were known from microfluidics and cell experiments [56, 125, 139]. For the micro-molding first molds with micro-channels were produced with photolithography and afterward, PDMS was cast in the molds and then removed after curing. Figure 4.2 shows the experimental setup and the clamping of the beads between channel walls. Also, force-displacement curves comparing the situation with beads inside the structure and without beads inside the structure are shown.

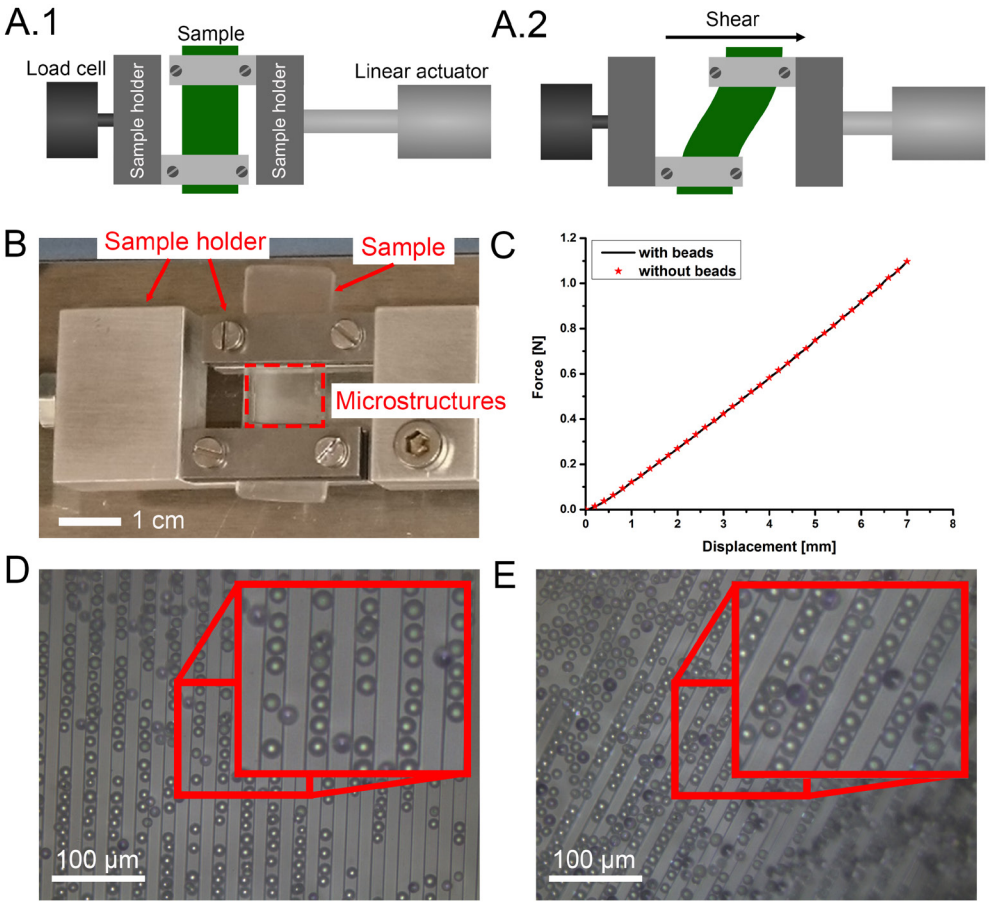

Figure 4.2A: Sketch of the tensile test setup to apply shear to a sample. A1: The sample is clamped in two sample holders. One sample holder is attached to a load cell and one sample holder is attached to a linear actuator. A2: The linear actuator applies shear to the sample. Deformation perpendicular to the direction of shearing is prohibited. B: The area of the sample between the sample holders is micro-structured with channels, and channel walls are chemically functionalized with biotin. A solution of streptavidin-coated beads is dropped onto the structured area. Shearing should lead to clamping of the beads between channel walls and due to the increased cross-linking to a stiffening of the sample. B: Force-displacement behavior of samples with and without beads inside the channels. For each situation, three tests were conducted. The errors in measurements were negligible. There was neither a detectable change in stiffness nor a difference between the measured force-displacement curves. C: Microscopy picture of the un-deformed sample. There is a gap between beads and channel walls. D: Microscopy picture of the deformed sample. Beads are clamped between channel walls.

As it can be observed in Figure 4.2C, beads did not influence the force-displacement curves of the samples indicating that a possible strain-stiffening effect did not exist or was below the limit of detection. The biggest challenge of this approach was determined to be the situation that channels in the micrometer range were introduced into a substrate with dimensions in the millimeter range. Consequently, it is very likely that the stiffening effect of the clamping of the beads was superimposed by the mechanical behavior of the substrate. An increase of the channel-depth to the millimeter range while at the same time keeping the channel-width and distance in the micrometer range would have probably solved the problem, but structures with such an extreme aspect ratio are technically challenging to realize. Therefore, this approach was discarded in further studies.

A second strategy was based on the tack of PDMS. The geometry of the substrate was modified to be entirely in the millimeter range and the mold for the samples could be produced with standard procedures in the workshop of the Faculty of Engineering. Instead of channels, the sample featured parallel slats with a squared cross-section. When the described shear force (see Figure 4.2A) is applied to the sample, the slats touch each other upon a certain degree of deformation. This is sketched in Figure 4.3A. If the touching walls of the slats tack to each other, a stiffening would be the consequence. This behavior is caused by the fact that due to the tack the structures show a higher degree of surface-to-surface interaction. The term surface-to-surface interaction is used because it is not a chemical cross-linking, but the effect on the material behavior is similar. Structures with higher cross-linking are stiffer than structures without cross-linking. Several examples for this effect can be observed in architecture, where cross-linking is used to increase the stability of buildings. Reversible cross-linking would lead to a reversible mechanical behavior. In this setup, no beads are needed to promote the desired surface-to-surface interaction and thus, strain-stiffening.

Figure 4.3B shows a sample made from PDMS Sylgard 184 mounted in the tensile test setup introduced in Figure 4.2A. One can see that the slats touch upon shearing. To observe the influence of the tack on the strain-stiffening effect in these samples tensile tests were conducted in two states. Firstly, a high tack between the slats was achieved by exploiting the tack of the PDMS [140]. Secondly, silicon oil was applied to the walls of the slats, to decrease the tack of the PDMS and to allow gliding of the slats.

Figure 4.3C shows the experimentally determined force-displacement behavior of two samples. It can be observed that there is no difference between the behavior with and without oil. Consequently, the tack of the PDMS had no influence on the force-displacement behavior of these samples.

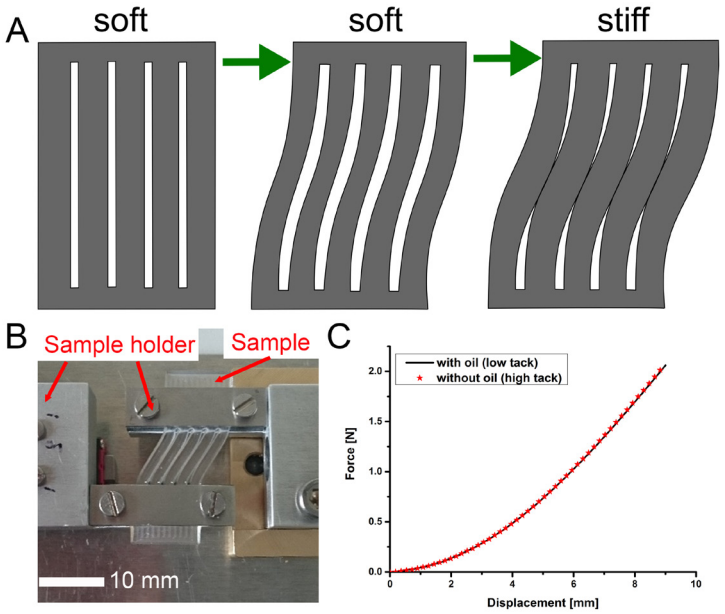

Figure 4.3A: Sketch of the concept of strain-stiffening due to shearing of a sample with slats. Shearing leads to touching of the slats. Reversible surface-to-surface interaction between touching surfaces should lead to a reversible stiffening of the material. B: Tensile-test setup for a sample with 5 slats. The sample is clamped between two sample holders. A shearing motion is introduced by a linear actuator on one side of the sample and on the other side, the force is measured with a load cell. Deformation perpendicular to the direction of the motion is prohibited. The tests are either carried out with a PDMS sample with natural tack or with oil applied on the slat surface to decrease the tack. C: Force-displacement behavior of samples measured in the tensile test setup. There is no difference between a sample with oil and without oil between the slats detectable. The increase of stiffness is caused by the stretching of the slats induced by the tensile-test setup.

The curves in Figure 4.3C show a general increase of stiffness with increasing displacement. This stiffening is most likely caused by the special way of shearing the sample and is therefore not a measure of the strain-stiffening behavior of the sample. In the test setup, only deformation in shearing direction (x-direction) was allowed. Deformation perpendicular to this direction (z-direction) is confined. This is sketched in Figure 4.4A (in comparison to a case where the deformation in the z-direction is not confined in Figure 4.4B). Since unconfined shearing would result in a contraction of the substrate in z direction, confined deformation leads to a forceful increase of the length of the slats with increasing displacement. As increasing the length of the slats needs more force than to just bend them, this results in an increased stiffness.

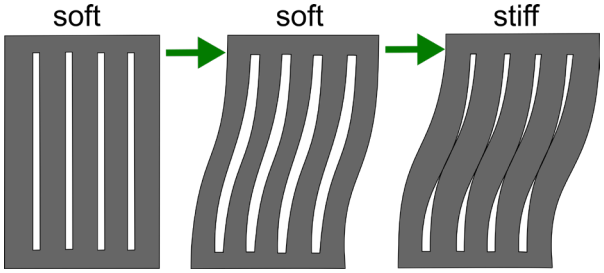

Figure 4.4: Sketch of the deformation of a sample with slats, if deformation in the z-direction is confined (A) and if deformation in the z-direction is not confined (B). It can be seen that confining the movement in z-direction forcefully stretches (i.e. increases the length of) the slats, which results in a tack independent stiffening of the substrate.

In order to investigate if the tack of the PDMS has no influence on the force-displacement behavior of the samples, or if the effect was just very low and it could be increased with a modification of the geometry the mechanical behavior of different sample geometries was simulated via FEM. As this method allows variations of the sample geometry without the need of new casting molds for every shape modification, the influence of the tack on the substrate strain-stiffening could be studied efficiently with a large variety of geometries. Two cases were simulated for each geometry. In the first case, representing the tack effect, no sliding between touching surfaces was allowed. In the second case, representing the non-tack effects, sliding with a low coefficient of friction was allowed. An example of a modified geometry that was optimized towards a high strain-stiffening effect as it was simulated is shown in Figure 4.5A. Figure 4.5B shows the simulated force-displacement behavior of the modified sample geometry from Figure 4.5A. Compared to the samples from the experimental tensile tests, the simulated geometry had 10 slats instead of 5 and the width of the slat was 1.9 times higher. Even though both curves show the same setup-induced stiffening behavior as the samples from experimental tensile tests, the influence of tack is clearly visible. The curves of the sample with tack and the sample without tack have the same stiffness up to a displacement of ~3 mm, which is the point where the slats start touching. At higher displacements the sample with tack underwent stiffening. This proves that the tack has an influence on the force-displacement behavior of the samples. The FEM analysis showed that the magnitude of the influence of the tack depends on the structure of the sample and proved a very useful tool to calculate the best sample geometry for a prominent strain-stiffening effects. An unfavorable geometry could be the reason why there was no influence of the tack visible in the experimental tensile tests (Figure 4.3C).

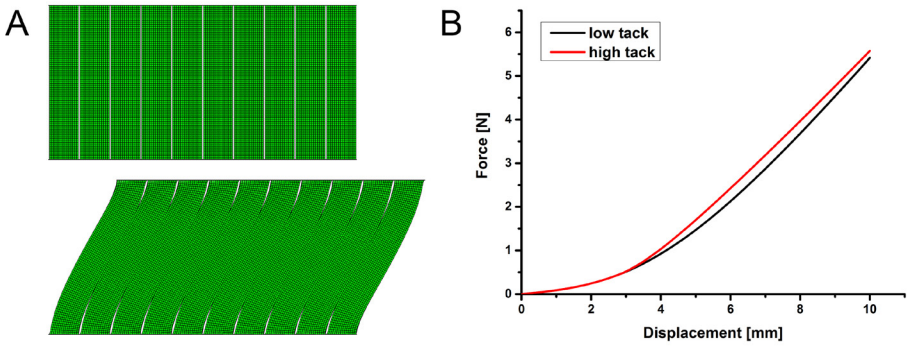

Figure 4.5A: Picture of a sample geometry with 10 slats in an un-deformed (top) and deformed (bottom) state. B: Simulated force-displacement behavior of the sample with high tack and low tack. Both curves are the same up to a displacement of ~3 mm. At higher displacements, the sample with high tack underwent a stiffening.

The experimental tensile-tests and FEM simulations showed that the tensile-test setup causes a stiffening of the structure that superimposes possible strain-stiffening effects of the material. This undesired stiffening was caused by a confinement of the deformation of the sample in the z-direction (Figure 4.4A). The confinement forced the slats to elongate. To avoid the undesired elongation of the slats, a test setup that allowed deformation in z-direction was necessary. A sketch of the desired deformation mechanism is provided in Figure 4.4B.

Figure 4.6A shows how the desired deformation mechanism was transferred into a test setup. A stamp with an attached load cell pushed on one side of the sample, while the other side of the sample was fixed. Since the sample holder does not clamp the entire top half of the sample anymore, enforcements made out of a non-elastic material were attached to the sample. To ensure an even distribution of the deformation induced by the stamp over the entire length of the sample. The enforcement on the other side of the sample allowed a clamping of the sample to a table. The stamp introduced a deformation in x-direction without confining the deformation in z-direction (Figure 4.6B), allowing the slats to deform without elongation. As a control, a sample with a large distance between the slats was used because, as sketched in Figure 4.6C, the slats do not touch when the sample is deformed and hence no stiffening should occur. Pictures of the samples made from Sylgard 184 are provided in Figure 4.6D. The geometrical features of the samples are optimized toward a maximum strain-stiffening effect based on the FEM analysis described before. A picture of the test setup is shown in Figure 4.6E and force-displacement curves from the experiments are provided in Figure 4.6F. The results indeed demonstrated strain-stiffening of the sample with low distance between slats after the slats started to touch at a displacement of ~3 mm. The control sample did not show strain-strain-stiffening.

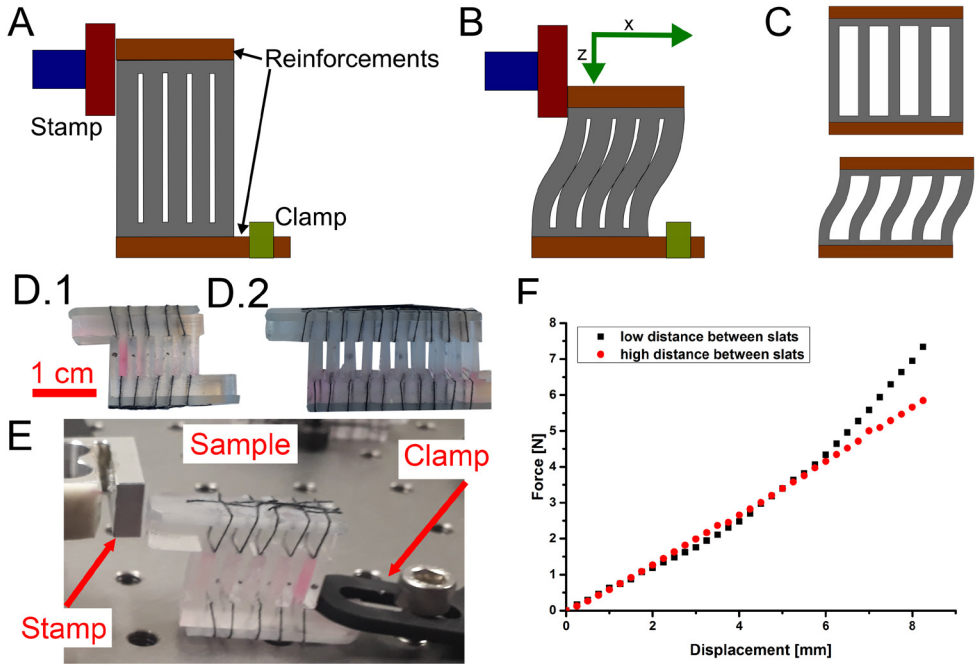

Figure 4.6A and B: Sketch of a test setup that allows free deformation of the sample in the z-direction. Reinforcements made from a non-flexible material are attached to the sample. The sample is clamped to a surface on one side. On the other side, a stamp with an included load cell is pushed against the sample. Reinforcements allow clamping of the sample and an even distribution of deformation over the length of the sample. C: Control sample with a wide distance between slats. The slats do not touch upon deformation. D: Picture of a sample with a low distance between slats (D.1) and with a high distance between slats (D.2). As the reinforcements could not be glued to the sample they are attached via strings (black). The strings are glued to the reinforcements. E: Picture of the test setup. The sample is clamped to a sample on one side. A load cell acts as a stamp on the other side and is pushed against the sample. The deformation and the force are recorded. F: Force-displacement curve of the samples with a high and low distance between slats. The control sample with a high distance between slats shows no stiffening. The sample with a low distance between slats shows strain-stiffening after the slats touch at a displacement of ~ 3 mm.

In this sub-chapter, several studies that influenced the design of the final strain-stiffening material were described. Most importantly it was shown that strain-stiffening can be achieved with special structures that include slats that are able to touch upon deformation. Additionally, FEM analysis indicated that the degree of the strain-stiffening depends on the geometry of this structure.

4.2. Design of a strain-stiffening structure for tensile tests

Based on the results presented in the previous sub-chapter a sample geometry was designed that allowed tensile tests instead of shear tests. In this chapter, the geometry of such a demonstrator sample is explained.

The geometry of the strain-stiffening sample is generally derived from combining four of the samples shown in Figure 4.6D into one and is presented in Figure 4.7A. The combination of two of these systems in a row with a common backbone allowed to transform a shearing motion into a linear elongation of the sample. Mirroring the structure along the axis of deformation lead to a symmetric deformation of the sample during stretching where no additional support structures are needed. The final structure is composed of four sets of slats that are connected via two backbones and two middle-backbones. At each middle-backbone, a protrusion for clamping in a tensile test setup is added.

The material used for the strain-stiffening sample was here the PDMS Elastosil RT625. Sylgard 184 was used in the previous tests as it is commonly used for micro-structured geometries. However, its mechanical properties are unsuitable for the tests that are conducted in this chapter as Sylgard 184 tends to break at low deformations and its stiffness increases at large deformations [95]. Elastosil RT625 is superelastic and can be stretched by up to 600% of its original length [87] before it breaks and its stiffness stays constant up to larger strains than Sylgard 184 [95], which makes it more suitable for the tests.

The strain-stiffening sample, shown in Figure 4.7A, was characterized in a tensile test setup. Additionally, the test was simulated in FEM, as shown in Figure 4.7B. Both, the experiment and the simulation yield a similar shape of the deformed sample. Later on, the influence of the modification of several geometrical features as well as the influence of friction between slats was determined by simulating the entire tensile test. The general procedure of the tensile tests and the FEM simulations was to start with a defined demonstrator sample and then to systematically modify a certain feature of this sample to determine its influence on the strain-stiffening behavior.

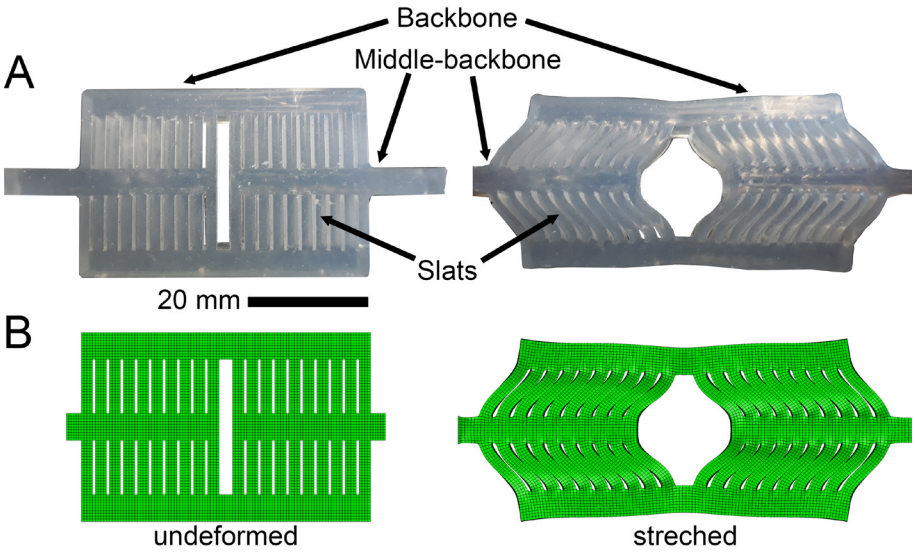

Figure 4.7A: Demonstrator sample made from PDMS Elastosil RT625 for the tensile test setup in an un-deformed (left) and stretched (right) state. B: Un-deformed and stretched representation of the sample in the FEM analysis.

The demonstrator sample will now be described in detail. Its geometrical features were partially derived from the preliminary experiments, partially defined by the geometry of the tensile test set-up and partially limited by the technical possibilities of sample production. The limit in technical possibilities of sample production is caused by the fact that the samples were cast in aluminum molds produced in the workshop of the Faculty of Engineering. The molds were produced with standard milling techniques and there are tool related limits to the aspect ratio between width and depth of structures in this method. The thickness of the backbone h, the width w and length l of the slats and the number of slats per set N were taken from the preliminary experiments with the optimized structure (see Figure 4.6D). While the depth of the sample D was influenced by the geometry of the tensile test setup, the distance between slats d was limited by the technical possibilities of sample production. The length of the protrusion for clamping p and the gap between the sets of slats g was chosen to be suitable for the tensile-test setup. Generally, it would not be necessary to include the protrusions in the simulation as they are fixed in the tensile-test setup and consequently are not expected to deform. However, as it is hard to realize clamping right at the edge of the structure in tensile tests, a small part of the protrusions (p')is simulated to represent the unclamped part of the structured material. All dimensions of the demonstrator sample are presented in Table 4.1 and their position in the sample is shown in Figure 4.8. The influence of the parameters was systematically investigated in FEM simulations. The slat-length l and the gap between the sets of slats g was kept constant in all simulations. Additionally, the friction between slat surfaces was simulated. Tensile tests with selected geometries were conducted to verify the FEM simulations.

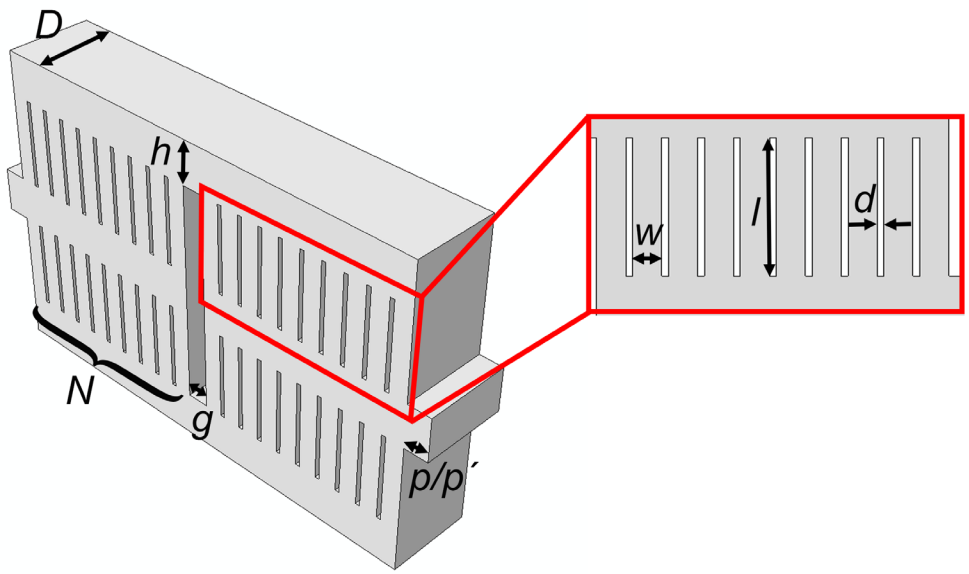

Figure 4.8: Sketch of the demonstrator sample with backbone-thickness *h*, number of slats *N*, slat-length *l*, slat-width *w*, distance between slats *d*, sample depth *D*, protrusion length *p*/*p*' and gap between sets of slats *g*.

Table 4.1: List of geometrical features of the demonstrator sample used for tensile tests and FEM simulation.

Parameter	Variable	Value
Backbone-thickness	*h*	5 mm
Number of slats	*N*	10
Slat-length	*l*	10 mm
Slat-width	*w*	2.1 mm
Distance between slats	*d*	0.5 mm
Sample-depth	*D*	10 mm
Protrusion-length (tensile test)	*p*	15 mm
Protrusion-length (FEM)	*p*'	2.75 mm
Gap between sets of slats	*g*	2.5 mm

4.3. Results and discussion

In this chapter, the mechanical behavior of the demonstrator sample as derived from a FEM simulation is presented and this example is used to describe and explain the general behavior of the strain-stiffening material. Additionally, a method of analytically calculating the stiffness of the sample is presented. In the following sub-chapters, the results from FEM based modifications of the geometrical features in Table 4.1 as well as the influence of friction are presented and the behavior is discussed. All FEM simulations were carried out assuming a lateral deformation of 40 mm. In the end, the results are compared to results experimentally determined in tensile tests.

4.3.1. Mechanical behavior of the demonstrator sample

The mechanisms that cause the strain-stiffening effect in the demonstrator sample are complex. For this reason, they are described here in detail. The first step necessary for understanding the strain-stiffening effect is to describe the sample as a series and parallel arrangement of springs. Using this simplified strategy allows describing the influence of all features in detail.

Figure 4.9A shows how the entire sample can be separated into four equal parts. Each part has a certain stiffness and can be represented by a spring. The resulting representation is, as shown in figure 4.9B, a series of two parallel arrangements of two springs.

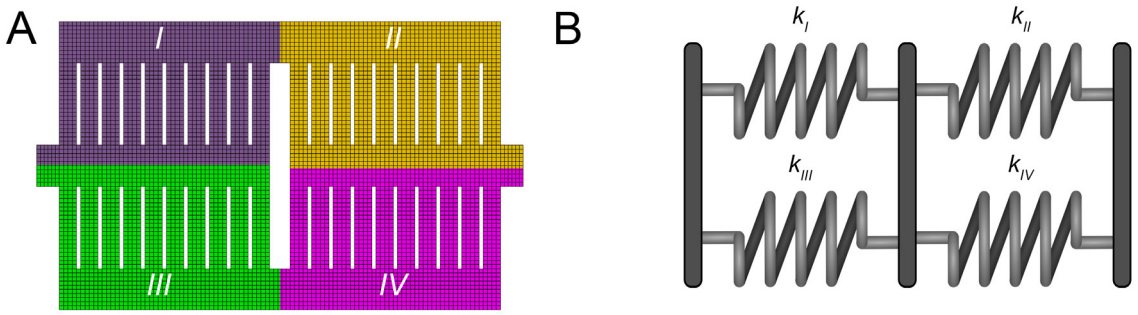

Figure 4.9A: The simulated demonstrator sample can be simplified by assuming four equal parts. Each part is marked with a different color and number. B: The mechanical properties of the sample can be represented by a series of two parallel arrangements of two springs. Each spring represents the stiffness of one part of the sample.

As the geometrical structure of each quarter of the sample plays a key role in the description of the mechanical behavior of the full sample it is from now on called quarter-structure. Each spring representing a quarter-structure in Figure 4.9B can be represented by a series of 5 springs. This is shown exemplarily for the purple quarter-structure (*I*) in Figure 4.10A and B.

The representation with springs is shown in Figure 4.10C. One spring represents the stiffness of the part of the middle backbone where no slats are attached (*1*), one the middle backbone with attached

slats (*2*), one the outer backbone with attached slats (*4*), one the outer backbone without attached slats (*5*) and one the stiffness of the slats (*3*). For later chapters, it is important to mention that the middle backbone where no slats are attached (*1*) represents the protrusion described before.

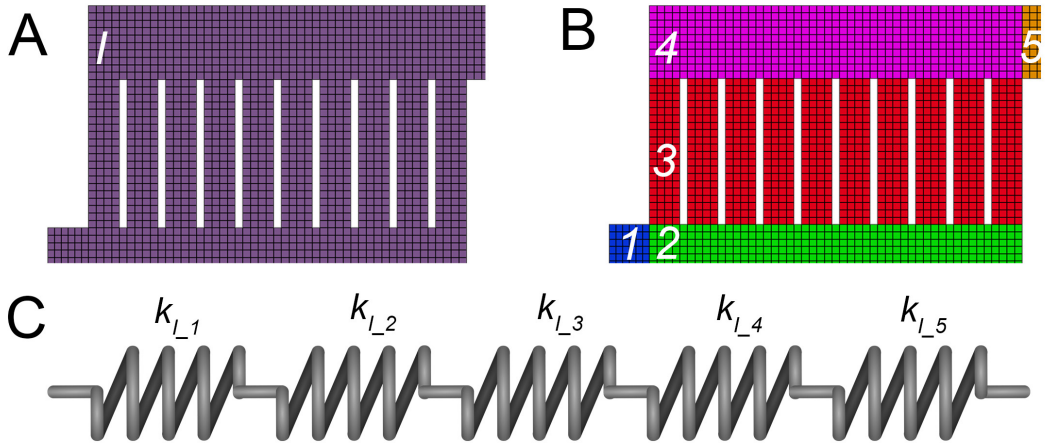

Figure 4.10: The purple quarter-structure of the simulated demonstrator sample (A) can be treated as a combination of five parts (B). Each part is marked with a different color and number and can be represented by a spring. The mechanical behavior of the entire quarter-structure can be described by that series of five springs. k_{I_i} are the corresponding spring constants.

The equation to describe the stiffness k_{DS} of the entire demonstrator sample (see Figure 4.9) is [141]:

$$k_{DS} = \frac{1}{\frac{1}{k_I + k_{II}} + \frac{1}{k_{III} + k_{IV}}} \tag{4.1}$$

As the stiffness of each quarter-structure should be the same, the stiffness values representing the entire quarter structure should be the same. If all stiffness values in equation 4.1 are set equal, k_{DS} will be equal to this stiffness value. Consequently, the stiffness of the demonstrator structure can be described by describing the stiffness of a single quarter-structure. This is a very important assumption that decreases the free parameters for the description of the mechanical behavior of the demonstrator sample drastically.

In addition, the stiffness of one quarter-structure is described by the equation describing a series of 5 springs. In the case of the quarter-structure from Figure 4.10 this would yield:

$$k_I = \frac{1}{\frac{1}{k_{I\_1}} + \frac{1}{k_{I\_2}} + \frac{1}{k_{I\_3}} + \frac{1}{k_{I\_4}} + \frac{1}{k_{I\_5}}} \tag{4.2}$$

Equation 4.2 includes two features that are very important for the upcoming description of the

mechanical behavior of the demonstrator sample. Firstly, the overall stiffness k_1 will always be lower than the stiffness of each part, e.g. k_{1_1}. Secondly, if the stiffness of one part is very high compared to all the others, this stiffness plays a minor role in the overall stiffness. To fully understand the mechanical behavior of the demonstrator sample it is necessary to describe the mechanical behavior of each part of the quarter-structure. Methods how to calculate the stiffness of these parts are provided in the following sub-chapters.

4.3.1.1. Mathematical description of the stiffness of the backbone

The parts of the backbone where no slats are connected (see Figure 4.10B *1* and *5*) can be described as a beam with a rectangular cross-section. This is shown in Figure 4.11.

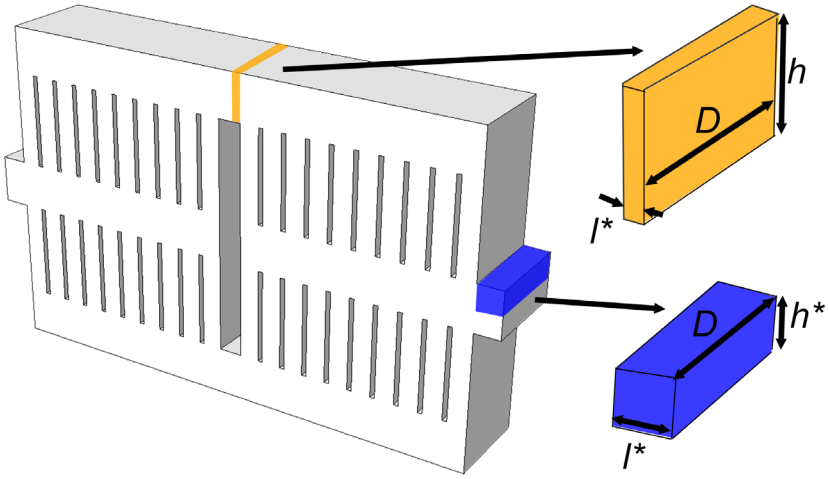

Figure 4.11: Image of a demonstrator sample in which two parts of the backbone without any connection to the slats are highlighted. It can be seen that each of these parts can be described as a linear beam with a certain length *l, the sample-depth *D* and the backbone-thickness *h*. *h** is equal to half of the backbone-thickness.**

The stiffness of a beam can be calculated by rearranging Hooke´s law [8, 68]:

$$\sigma = E\varepsilon \text{ with } \sigma = \frac{F}{A}, A = D \cdot h, \varepsilon = \frac{\Delta l^*}{l^*} \text{ and } k = \frac{F}{\Delta l^*} \tag{4.3}$$

$$k = E\frac{D \cdot h}{l^*} \tag{4.4}$$

The stiffness of the beam depends on the Young´s modulus E and the depth D, thickness h and length l^* of the regarding part of the backbone. All these parameters are known for the slat-free parts of the demonstrator sample backbone.

4.3.1.2. Mathematical description of the stiffness of the slats

The stiffness of the slats (see Figure 4.10B *3*) can be calculated by calculating the stiffness of a single slat and multiplying it by the number of slats in the described block of slats. The equation describing the stiffness of a slat that is confined on top and on the bottom is known from descriptions of parallel spring arrangements. It yields [142]:

$$k = \frac{EDw^3}{L^{*3}} \tag{4.5}$$

In this case, w is the slat-width, D its depth and L^* its length. E is the Young´s modulus of the material.

The equation is derived for metal springs that are fixed on a solid plate. Slats that are fixed on a surface that has the same stiffness as the slat itself also deform the surface if the slat is bent. Schön et al. [131] derived a way of determining a correction factor that takes this behavior into account. As this derivation is based on pillars with a round cross-section, the approach had to be adapted for the slats with a rectangular cross-section. Similar to Schön et al., a correction factor for the stiffness of the slat was calculated using the following equation, which takes bending, shearing and tilting of a slat into account (Figure 4.12):

$$corr = \frac{\delta_{bend}}{\delta_{bend} + \delta_{shear} + \delta_{tilt}} \tag{4.6}$$

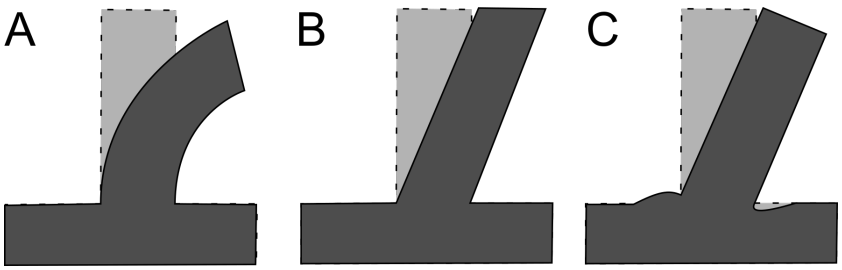

Figure 4.12: Three different modes of displacement of a slat. A: Bending. B: Shearing. C: Tilting

In the equations for δ_{bend}, δ_{shear} and δ_{tilt} from Schön et al. all parameters that described a round cross-section (I, K and σ_{max}) were replaced with descriptions of the rectangular cross-section of the slats. Consequently, they yield:

$$\delta_{bend} = \frac{FL^{*3}}{3EI} \text{ with } I = \frac{Dw^3}{12} [143] \tag{4.7}$$

$$\delta_{shear} = \frac{FL^*}{KGA} \text{ with } G = \frac{E}{2(1+\nu)}, \nu = 0.5\,, K = \frac{10(1+\nu)}{12+11\nu} [144] \text{ and } A = Dw \tag{4.8}$$

$$\delta_{tilt} = \frac{T_{tilt} L^* \sigma_{max}}{E} \text{ with } T_{tilt} = 1.3 \frac{(1+\nu)}{2\pi} \left\{ 2(1-\nu) + \left(1 - \frac{1}{4(1-\nu)}\right) \right\} \text{ and } \sigma_{max} = \frac{L^* F w}{2I} \text{ [143]} \quad (4.9)$$

The final correction factor only depends on the Poisson´s ratio of the material ν and the width *w,* and the length L^* of the slat.

$$corr = \frac{\frac{4L^{*2}}{w^2}}{\frac{4L^{*2}}{w^2} + \frac{2(1+\nu)}{K} + \frac{6L^* T_{tilt}}{w}} \quad (4.10)$$

The final stiffness of a single slat can be calculated by multiplying the stiffness of the slat with the correction factor. To correctly describe the stiffness of a slat in the demonstrator sample only half the length of the slat has to be used for the calculation of the correction factor ($L^*=l/2$). The reason for this is that the slat is fixed to the backbone on both ends. Consequently, its bending behavior can be described by the superposition of two slats with half of the slat-length *l* that are only fixed on one end. This is shown in Figure 4.13.

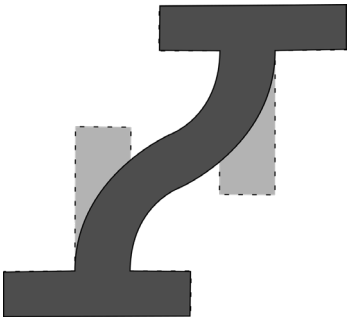

Figure 4.13: Deformation behavior of a slat that is fixed to a surface on both sides.

4.3.1.3. Description of the stiffness of a quarter-structure

As mentioned before, it is necessary to know the stiffness of all five constituent parts of the respective structure for the description of the stiffness of a quarter-structure.

The stiffness of the slats (Figure 4.10B *3*), as well as the stiffness of the parts of the backbone where no slats are attached (Figure 4.10B *1* and *5*), can be calculated, by using the equations from the sub-chapters 4.3.1.1 and 4.3.1.2. The stiffness of the parts of the backbone where slats are attached (Figure 4.10B *2* and *4*) cannot be directly calculated as it is assumed that their stiffness is influenced by the slats to an unknown extent.

It is possible to define two extreme cases for the stiffness of the parts of the backbone with slats attached (Figure 4.10B *2* and *4*). One scenario is that the attached slats have no influence on their

stiffness. In this case, the stiffness of the the two parts (*2* and *4*) of the backbone can be calculated in the same way as the stiffness of the backbone without slats attached (Figure 4.10B *1* and *5*). Alternatively, the attached slats increase the stiffness of the regarding parts of the backbone (*2* and *4*) drastically. Equation 4.2 shows that, if the stiffness of the the parts of the backbone with attached slats (*2* and *4*) exceeds the stiffness of the other parts drastically it has no influence on the overall stiffness and can be ignored. Consequently, the stiffness of the quarter-structure can be described by the stiffness of the slats (Figure 4.10B *3*)and the two parts of the backbone without attached slats (*1* and *5*).

With this approximation, it is possible to calculate the stiffness of the quarter-structure analytically.

4.3.1.4. Qualitative description of the mechanical behavior of the demonstrator sample

In Figure 4.14, the force-displacement curve of the demonstrator sample derived by FEM analysis is provided. In this curve, three regimes are marked. In the initial stiffness regime, there is a linear relation with a positive slope between the force and the displacement that is superimposed by small vibrations, which are artifacts from the FEM simulation. In the transition regime the slope of the curve increases. It is, similar to the initial stiffness regime superimposed by small vibrations, but the amplitude of the vibration decreases with increasing displacement. In the final stiffness regime, the curve has a constant slope that is higher than the slope in the initial stiffness regime.

The vibrations that superimpose the curve, in the beginning, are an artifact from the simulation and it was not possible to avoid them. As they are supposed to have no influence on the general outcome of the simulation they are ignored in the discussion of the experiments.

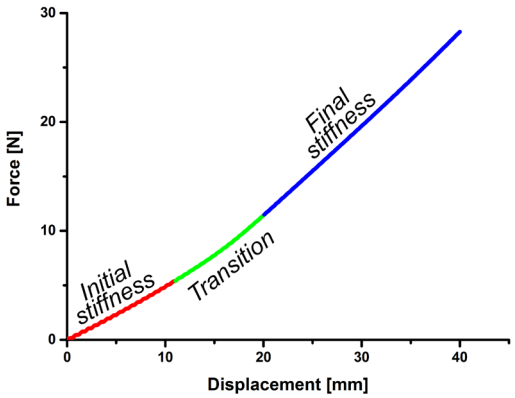

Figure 4.14: Force-displacement curve of the demonstrator sample, as derived from FEM analysis. Three regimes are marked: The initial stiffness, a transition regime and the final stiffness. The vibrations that superimpose the curve, in the beginning, are an artifact from FEM analysis.

With the information from the previous sub-chapters, the force-displacement behavior of the demonstrator sample can be well described. All descriptions assume that the Young´s modulus of the silicone is constant for the observed degree of deformation of ~100% [95].

The initial stiffness is constant. The stiffness can be described by the bending of the slats and by the stretching of the backbone. As the stiffness of all included parts does not depend on the degree of deformation (see equations 4.4 and 4.5), a constant stiffness is expectable. The shape of the sample changes from an un-deformed state as shown in Figure 4.15A to a slightly deformed state as shown in Figure 4.15B

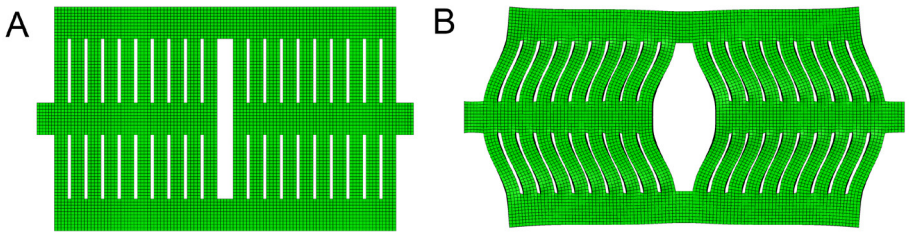

Figure 4.15A: Shape of the demonstrator sample without deformation. B: Shape of the demonstrator sample with slight deformation.

In the transition regime in Figure 4.14, the sample stiffness increases. In this regime, the slats first start to touch each other and most likely two effects superimpose. Figure 4.16 shows the deformed sample with touching slats and one area is highlighted and magnified. The first effect that can be observed is that in a block of slats the slats in the middle are highly confined in their bending behavior (highlighted in Figure 4.16). The part in the middle is not curved but straight. According to Van Eijk [142], this leads to an increase of the stiffness of the slats with increasing length of the straight part. As the length of the straight part increases with increasing displacement, this behavior is one reason for the overall increase of stiffness. A second effect has presumably a higher influence on the stiffening than the effect decribed before. Equation 4.5 shows that the stiffness of a slat increases by the power of 3 with its width. One could state that the stiffness of all touching slats in a block of slats is equal to the stiffness of a single slat with a width that is the sum of all slats in the block. In the case of the demonstrator sample, the stiffness would increase by a factor of 1000 if one assumes that the 10 slats form a single slat. However, this assumption has several restrictions. The slats do not touch over their entire length and even though there is a certain tack between the slats they have the ability to glide over each other. Additionally, the length of the backbone is increased, changing the distance between the slats.

The two effects balance each other at a certain degree of deformation, resulting in the increased final stiffness.

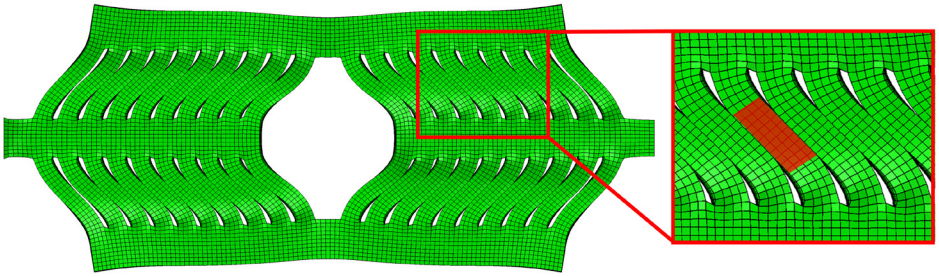

Figure 4.16: Shape of the demonstrator material with a deformation that leads to a touching of the slats. The magnified area shows that slats are confined in their bending behavior. Instead of showing a smooth curve the part in the middle is straight (highlighted in red). This causes to a higher stiffness of the slat.

The final stiffness, in Figure 4.14, is constant, but higher than the initial stiffness. Equation 4.2 states that if the stiffness of a certain part of the quarter-structure exceeds the others by far it does not have any influence on the stiffness of the quarter-structure. Assuming that the stiffness of the slats increases drastically in the transition regime and that it is balanced at the beginning of the final stiffness regime, the stiffness of the quarter-structure is then dominated by the stiffness of the backbone. As described before, the stiffness of the backbone is not influenced by displacement. Consequently, the final stiffness stays constant.

4.3.1.5. Analytical description of the mechanical behavior of the demonstrator sample

As described before it is sufficient to describe the mechanical properties of one quarter-structure in order to describe the properties of the entire demonstrator sample. For the full description of the stiffness of the quarter-structure, the stiffness of all five contributing parts has to be known: The stiffness of the slats (Figure 4.10B *3*), the middle backbone with no attached slats (Figure 4.10B *1*), the outer backbone with no attached slats (Figure 4.10B *5*), the middle backbone with connecting slats (Figure 4.10B *2*) and the outer backbone with connecting slats (Figure 4.10B *4*). While the stiffness of the slats and the parts of the backbone without attached slats can be calculated analytically by the equations given in chapter 4.3.1.1 and 4.3.1.2, the stiffness of the parts of the backbone with attached slats is unknown as described in chapter 4.3.1.3. The initial stiffness of the demonstrator sample can be calculated with the approximations described in chapter 4.3.1.3.

In the approximation that the slats do not influence the stiffness of the backbone, the length of the outer backbone with and without attached slats (Figure 4.10B *4* and *5*) can be added and its stiffness can be calculated. The same holds for the inner backbone (Figure 4.10B *1* and *2*). Consequently, the stiffness of all parts of the quarter-structure is known and the overall stiffness can be calculated. The resulting stiffness represents the minimum analytically calculated stiffness and will from now on be referred to as k_{min_c}.

In the approximation that the slats increase the stiffness of the backbone drastically, only the parts of the backbone without attached slats (Figure 4.10B *1* and *5*) and the stiffness of the slats (Figure 4.10B *3*) are used for the calculation of the stiffness of the quarter structure. The resulting stiffness represents the maximum analytically calculated stiffness and will from now on be referred to as $k_{max\_c.}$

Using the equations from chapter 4.3.1.1 and 4.3.1.2 with the dimensions of the demonstrator sample, a Young´s modulus of 0.87 MPa (according to Ref. [145]) and a Poisson´s ratio of 0.5 (according to Ref. [133]) k_{min_c} is calculated to be 0.27 N/mm while k_{max_c} is 5.1 N/mm. The stiffness obtained from the simulation is 0.48 N/mm. Consequently, the simulated stiffness lies, as expected, between the two calculated extreme cases.

As described before the stiffness of the slats increases after they start touching each other and two effects superimpose. From this point on it is no longer possible to determine the stiffness of the slats analytically. This makes the assumptions of the force-displacement behavior in the transitional regime and the analytical calculation of the final stiffness extremely inaccurate, as three out of the five parameters to calculate the stiffness of the quarter-structure are unknown. Consequently, the final stiffness is not calculated analytically in this thesis.

In this chapter, the strain-stiffening behavior of the demonstrator sample was explained and a method for the analytical calculation of the initial stiffness was provided. In the following chapters, the simulation of the influence of several parameters on the strain-stiffening behavior of the material is described. The results from the simulations are described qualitatively. Additionally, to verify the analytical approach, the analytical calculation of the initial stiffness is compared to the simulated initial stiffness for cases where the tested parameter had a strong influence on the initial stiffness.

4.3.2. Influence of the backbone-thickness

The goal of the series of simulations in this sub-chapter was to determine the influence of the thickness of the backbone h on the strain-stiffening behavior of the structure. Figure 4.17A and B show the geometry of a sample with a thick backbone in comparison to the demonstrator sample. The simulated force-displacement curves, as well as the simulated initial and final stiffness for each modification of the backbone are presented in Figure 4.17C and D. The curve representing the demonstrator sample is plotted in red with a thicker line. This will also be the case in all following chapters.

In Figure 4.17 C and D it is clearly visible that an increase of backbone-thickness compared to the standard sample leads to a small increase of the initial stiffness and to a large increase of the final stiffness. The increase of the final stiffness seems to be linear.

The influence of the backbone-thickness on the final stiffness can be explained by using the description of a series of springs. At a certain displacement, the stiffness of the touching slats exceeds the stiffness of the backbone drastically. Consequently, the stiffness of the material is mainly represented by the stiffness of the backbone. Equation 4.4 in chapter 4.3.1.1 shows that the stiffness of the backbone scales linearly with its thickness h. This explains the linear increase of stiffness with increasing backbone-thickness.

Figure 4.17 E shows the analytically calculated initial stiffness k_{min_c} and k_{max_c} as well as the initial stiffness derived from the simulations for samples with different backbone-thicknesses. The analytically derived stiffness k_{max_c} is closer to the simulated stiffness than k_{min_c} for all analyzed backbone-thicknesses. This result indicates that it is more accurate to describe the stiffness of the sample by assuming that the slats increase the stiffness of the backbone drastically than to assume that they do not influence the backbone.

The results also show that k_{max_c} increases with increasing backbone thickness. This behavior was also determined for the simulated stiffness. The behavior can be explained by the fact that an increasing backbone thickness leads to an increased backbone stiffness as described by equation 4.4. The influence of this increase is not as pronounced as in the case of the final stiffness, as the stiffness of the backbone is high, compared to the stiffness of the slats. According to equation 4.2, this leads to a low influence of the stiffness of the backbone on the initial stiffness of the structure.

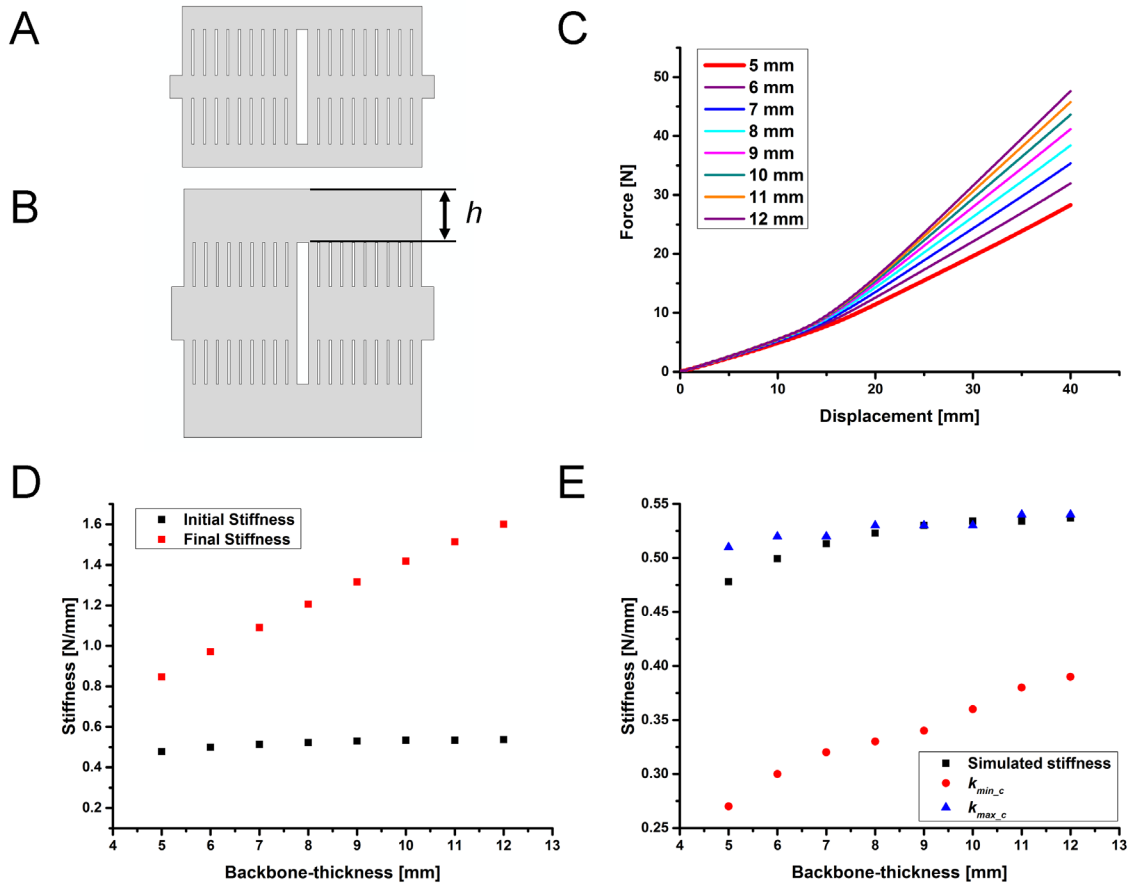

Geometry of the demonstrator sample. B: Geometry of a sample with increased backbone-thickness *h* compared to the demonstrator sample C: Simulated force-displacement behavior of strain-stiffening samples with varied backbone-thicknesses. D: Simulated initial and final stiffness for each backbone-thickness. E: Analytically calculated initial stiffness k_{min_c} and k_{max_c} as well as the initial stiffness derived from the simulations for samples with different backbone-thicknesses.

4.3.3. Influence of slat-width

The goal of the series of simulations in this sub-chapter was to determine the influence of the width of the slats w on the strain-stiffening behavior of the structure. The geometry of a sample with a decreased slat-width in comparison to the demonstrator sample is shown in Figure 4.18A and B. The simulated force-displacement curves, as well as the simulated initial and final stiffness for each modification of slat-width, are presented in Figure 4.18C and D. They show that a decrease of slat width compared to the standard sample has a large influence on the initial stiffness and an influence on the final stiffness that is smaller than the influence on the initial stiffness. The final stiffness seems to increase linearly with decreasing slat-width.

A change of slat-width led to an inevitable change of a second parameter. With decreasing slat-width the length of the backbone, to which slats are connected was decreased, too. While the decrease in backbone length leads to a linear increase of stiffness (equation 4.4), the decrease of slat-width results in a decrease of stiffness with the power of 3. This was described in equation 4.5. in chapter 4.3.1.2. Consequently, a decrease of the initial stiffness with decreasing slat-width is expected.

Figure 4.18E shows the analytically calculated initial stiffness k_{min_c} and k_{max_c} as well as the initial stiffness derived from the simulations for samples with different slat-widths. The simulated stiffness, k_{min_c} and k_{max_c} decrease with decreasing slat-width. k_{max_c} starts slightly above the simulated stiffness at a slat-width of 2.1 mm, is almost the same as the simulated stiffness at 1.9 mm and is slightly below the simulated stiffness for all lower slat-widths. k_{max_c} is closer to the simulated stiffness than k_{min_c} for all slat-widths except for the slat-width of 0.9 mm. At this point, k_{max_c} and k_{min_c} are almost the same. k_{min_c} is below the simulated stiffness for all slat-widths. While its value is far below the simulated one at higher slat-widths, it approaches the simulated values width decreasing slat-width.

The situation that k_{min_c} describes the initial stiffness better with decreasing slat-width is caused by the decrease of backbone-length. With decreasing backbone-length the backbone becomes stiffer and consequently, it´s influence on k_{min_c} decreases. This behavior supports the theory that it is accurate to describe the initial stiffness of the sample with k_{max_c}, where the influence on the backbone with attached slats is neglected. This means that the stiffness of the backbone seems to be drastically increased by the attached slats, even if the slat-width is changed. Additionally, when the slat-width is decreased and the thickness of the backbone stays constant, the backbone-thickness becomes higher in comparison to the slat-width. As described in chapter 4.3.2 this leads to a decreased influence of the stiffness of the backbone between with attached slats and explains why again, k_{max_c} describes the simulated values well.

The increase in final stiffness with decreasing slat-width is caused by the decrease of backbone length. A linear decrease in slat-width leads to a linear decrease in backbone-length and consequently to a linear increase of stiffness.

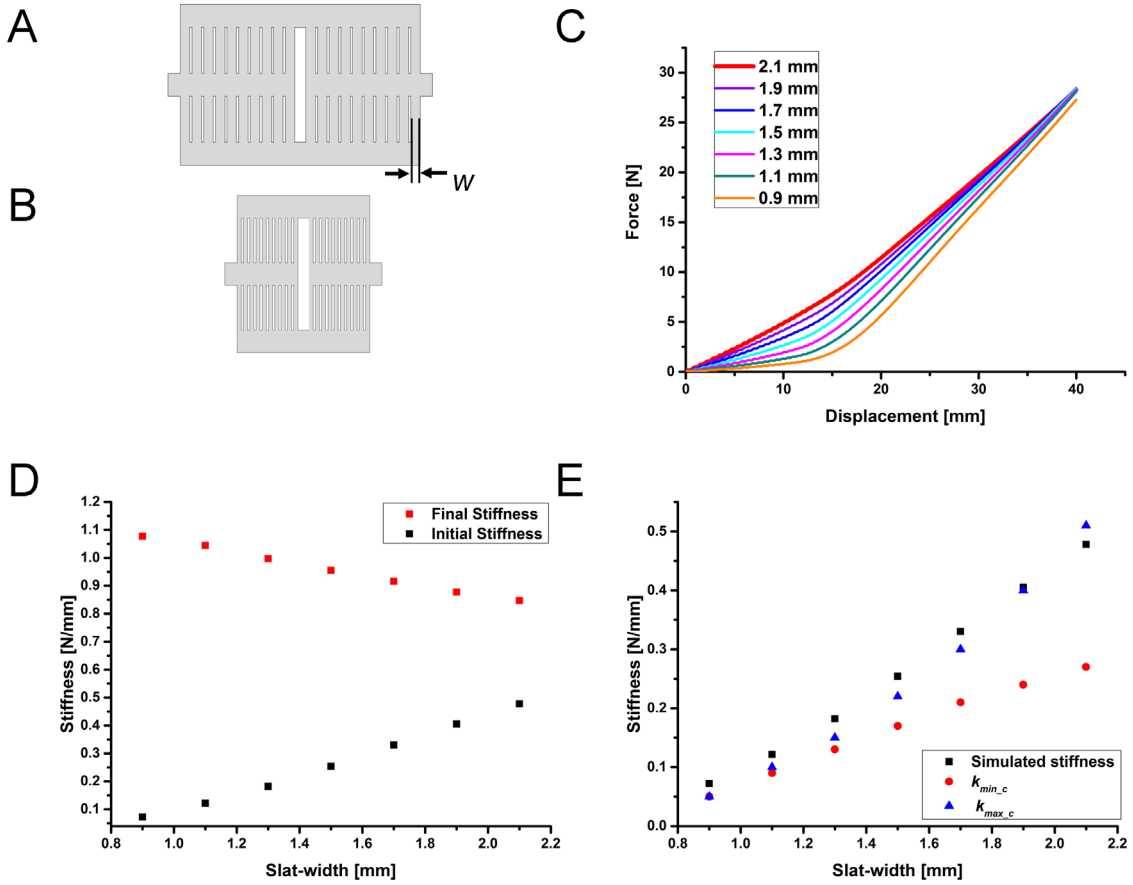

Figure 4.18A: Geometry of the demonstrator sample. B: Geometry of a sample with decreased slat-width *w* compared to the demonstrator sample C: Simulated force-displacement behavior of strain-stiffening samples with varied slat-width. D: Simulated initial and final stiffness for each slat-width. E: Analytically calculated initial stiffness k_{min_c} and k_{max_c} as well as the initial stiffness derived from the simulations for samples with different slat-widths.

4.3.4. Influence of distance between slats

The goal of the series of simulations in this sub-chapter was to determine the influence of the distance between slats *d* on the strain-stiffening behavior of the structure. The geometry of a sample with a decreased distance between slats in comparison to the demonstrator sample is provided in Figure 4.19A and B. The simulated force-displacement curves, as well as the simulated initial and final stiffness for each distance between slats, are presented in Figure 4.19C and D. Additionally, a graph with the "point of stiffening" of each sample is given in Figure 4.19E.

According to the qualitative description of the force-displacement behavior of the strain-stiffening structure in chapter 4.3.1.4 the "point of stiffening" would be the point where the slats first start touching and the stiffness first starts increasing. This exact point is hard to determine from the force-displacement curves as it is not very pronounced in the force-displacement curve of the demonstrator sample and therefore superimposed by the vibrations also described in chapter 4.3.1.4. For this reason, a different method was chosen to represent this "point of stiffening". As it will later be described in the materials and methods part, the initial and final stiffness is determined by fitting a straight line to each of the straight parts of the force-displacement curves that represent the initial and final stiffness. These two straight lines intersect at a certain point. This point is used in this chapter to describe the "point of stiffening" as it contains all the information necessary for the description of the influence of a change of distance between slats on the strain-stiffening behavior (see inset Figure 4.19E).

As presented in Figure 4.19E, the "point of stiffening" is shifted to smaller displacements with a smaller distance between the slats. If slats are closer to each other less displacement is needed until they touch. This explains why the stiffening occurs at lower displacements when the distance between slats is decreased and vice versa. The effect can be demonstrated with an analytical method as described in the Patent "Schicht mit variabler Festigkeit" [146].

In the representation of the initial and final stiffness of the samples (Figure 4.19D), a small increase of stiffness with decreasing distances can be detected. From the experiments described in previous sub-chapters, it is expectable that both, the initial and final stiffness show a slight increase as a response to a decrease in distance between slats. Figure 4.19B shows that a decrease of the distance between the slats decreases the length of the backbone and consequently increases its stiffness. As the decrease in backbone length in this experiment is small (3.6 mm), compared to the experiment with different widths of the slats (12 mm) in chapter 4.3.3, the change of stiffness is not as prominent.

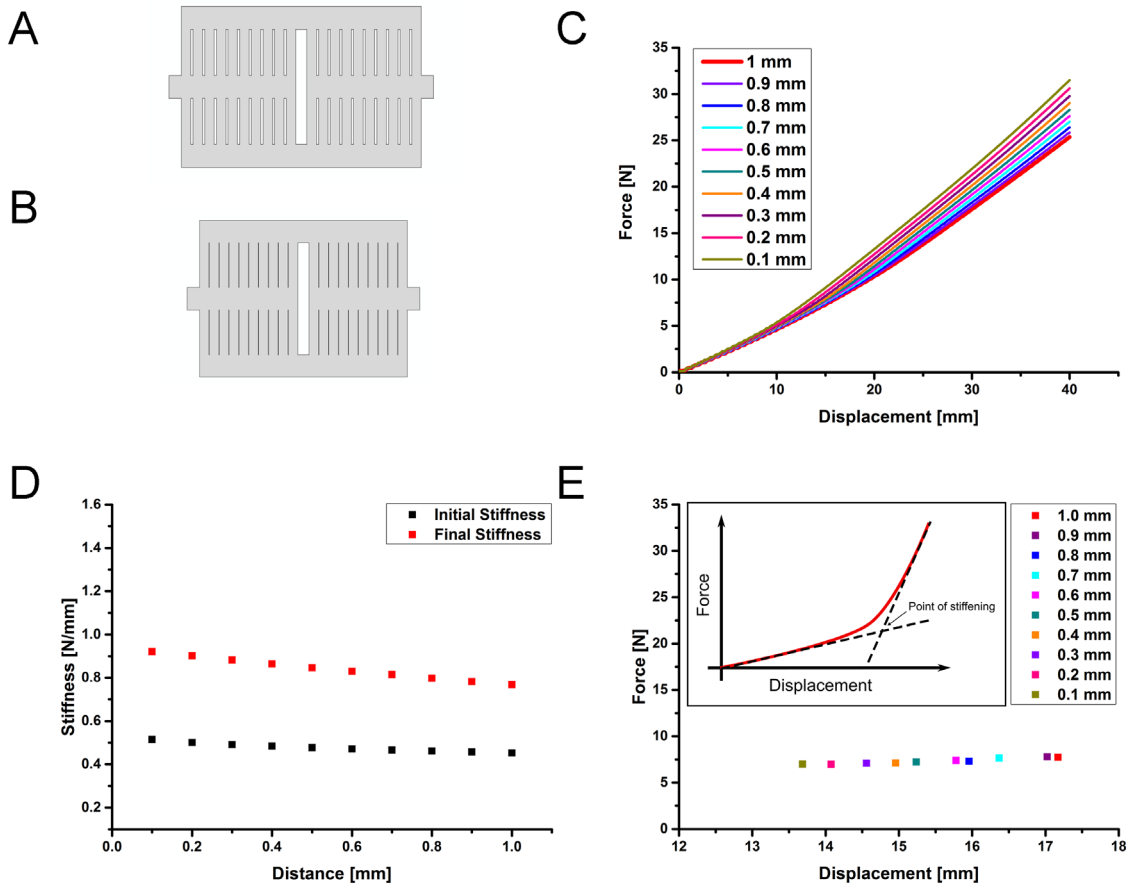

Figure 4.19A: Geometry of the demonstrator sample. B: Geometry of a sample with decreased distance between slats *d* compared to the demonstrator sample C: Simulated force displacement behavior of strain-stiffening samples with varied distance between slats. D: Simulated initial and final stiffness for each distance. E: Point of stiffening for each distance between slats. Inset E: The point of stiffening was set to be the intersection of the line representing the initial stiffness and the line representing the final stiffness.

4.3.5. Influence of number of slats

The goal of the series of simulations in this sub-chapter was to determine the influence of the number of slats *N* on the strain-stiffening behavior of the structure. The geometry of a sample with a decreased number of slats in comparison to the demonstrator sample is shown in Figure 4.20A and B. The simulated force-displacement curves, as well as the simulated initial and final stiffness for each number of slats, are presented in Figure 4.20C and D. With a decreasing number of slats, compared to the standard sample, the initial stiffness is decreased and the final stiffness is increased. The opposite holds for an increase in the number of slats. The increase of initial stiffness with increasing number of slats is lower at a higher number of slats.

Two parameters influence the initial stiffness with a varying number of slats. On one hand the stiffness of the slats - it increases linearly with an increasing number of slats. On the other hand, the backbone - its length increases linearly with an increasing number of slats. As a consequence, its stiffness decreases linearly with increasing slat numbers. In Figure 4.20B the opposite case is shown. If there are fewer slats the backbone-length is decreased compared to the demonstrator sample and its stiffness is increased. As the initial stiffness increases with increasing slat numbers it can be assumed that the increase of the stiffness of the slats dominates the behavior.

Figure 4.20E shows the analytically calculated initial stiffness k_{min_c} and k_{max_c} as well as the initial stiffness derived from the simulations for samples with a different number of slats. All values for the initial stiffness increase with an increasing number of slats. While k_{max_c} seems to increase linearly, k_{min_c} and the simulated stiffness increase with a decreasing slope with an increasing number of slats. k_{min_c} is far below the simulated stiffness for all numbers of slats. k_{max_c}c is very similar to the simulated stiffness for a lower number of slats. For numbers over 8 the values of k_{max_c} start to diverge from the simulated ones and become increasingly larger than the simulated stiffness values.

k_{max_c} increases linearly with an increasing number of slats because it is not influenced by the change of backbone-length and consequently it shows only the linear increase of stiffness of the slats. The simulated stiffness k_{min_c} and k_{max_c} are both influenced by the change of backbone-length. With an increased number of slats, the backbone becomes longer and less stiff. With a decreased stiffness its influence on the equation for the calculation of the initial stiffness (equation 4.2) grows and consequently the overall increase of stiffness is lowered with an increased number of slats. This also explains why k_{max_c} describes the simulated stiffness well if there are fewer slats and not as well if there are more slats. If there are fewer slats the backbone is quite short and quite stiff. Its influence on the equation for the calculation of the initial stiffness would be low and consequently, the assumptions made for the calculation of k_{max_c} describe the behavior well. The opposite holds if there are more slats and the backbone is less stiff.

The influence on the final stiffness is caused by the change of the length of the backbone that is associated with a change in the number of slats. A decrease of slats leads to a decrease of backbone-length

and to an increase of final stiffness of the sample and vice versa.

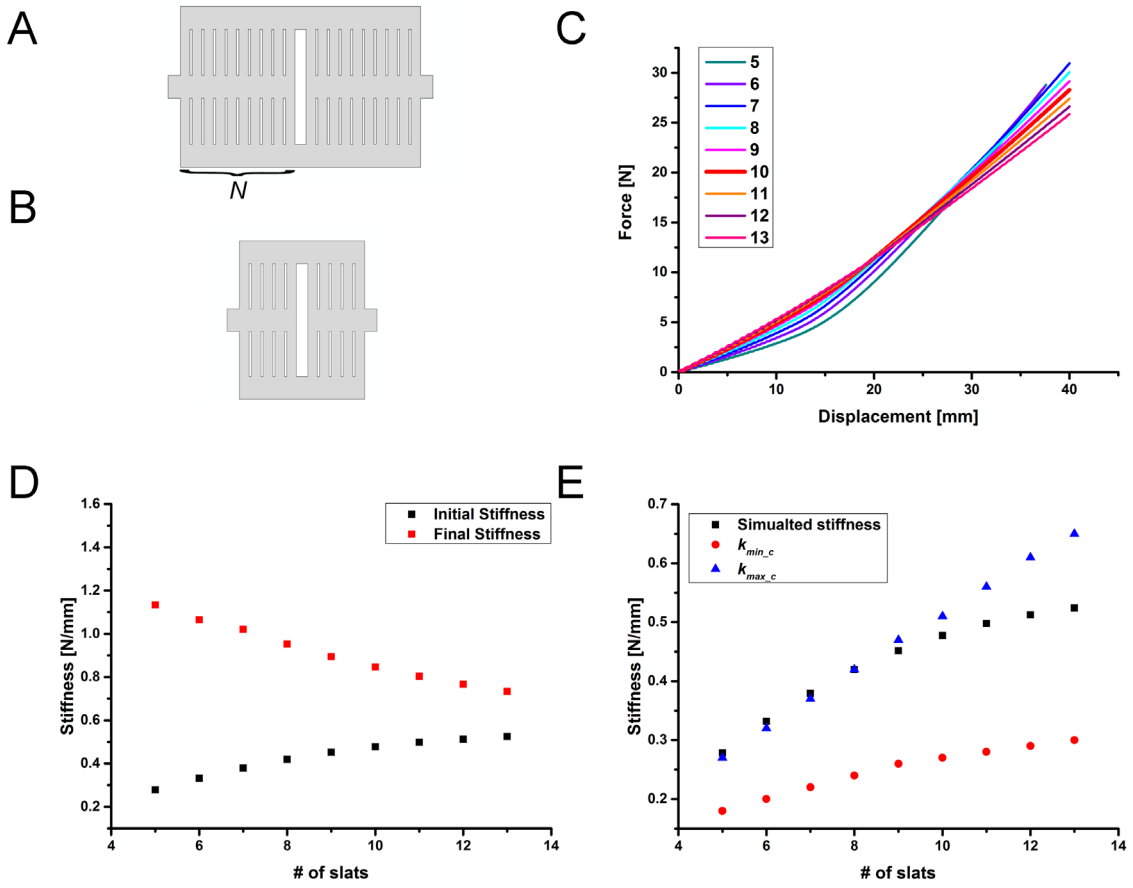

Figure 4.20A: Geometry of the demonstrator sample. B: Geometry of a sample with a decreased number of slats *N* compared to the demonstrator sample. C: Simulated force-displacement behavior of strain-stiffening samples as a function of number of slats. D: Simulated initial and final stiffness for each number of slats. In the case of 5 and 6 slats, the simulation was only conducted until a displacement of 37 mm, due to a non-converging simulation. E: Analytically calculated initial stiffness k_{min_c} and k_{max_c} as well as the initial stiffness derived from the simulations for samples with a different number of slats.

4.3.6. Influence of protrusion-length

In the series of simulations in this sub-chapter the length of the protrusion that represents the part of the sample that is not completely clamped in a tensile test setup *p'* is varied. An example of a sample with a short protrusion in comparison to the demonstrator sample (Figure 4.21A) is shown in Figure 4.21B. The goal of this test was not to achieve any new information about the sample but to achieve an improved match between simulated and measured curves. For this reason, the simulated force-displacement behavior in Figure 4.21C is only shortly discussed. The length of the protrusion has a minor influence on the initial stiffness and a high influence on the final stiffness. Both increase with decreasing protrusion length. This behavior can be well explained with the findings described in the previous sub-chapters. It has been shown that the stiffness of the structure can be described by a series of springs. The main influence to the initial stiffness comes from the stiffness of the slats and a minor influence from the stiffness of the protrusion, as the protrusion is stiff in comparison to the slats. With decreasing length, its stiffness increases and consequently the entire initial stiffness is increased by a small amount. The final stiffness is mainly dominated by the stiffness of the backbone. As the protrusion is a part of the backbone, more specifically the part of the middle backbone without attached slats, its change of stiffness influences the final stiffness to a higher degree.

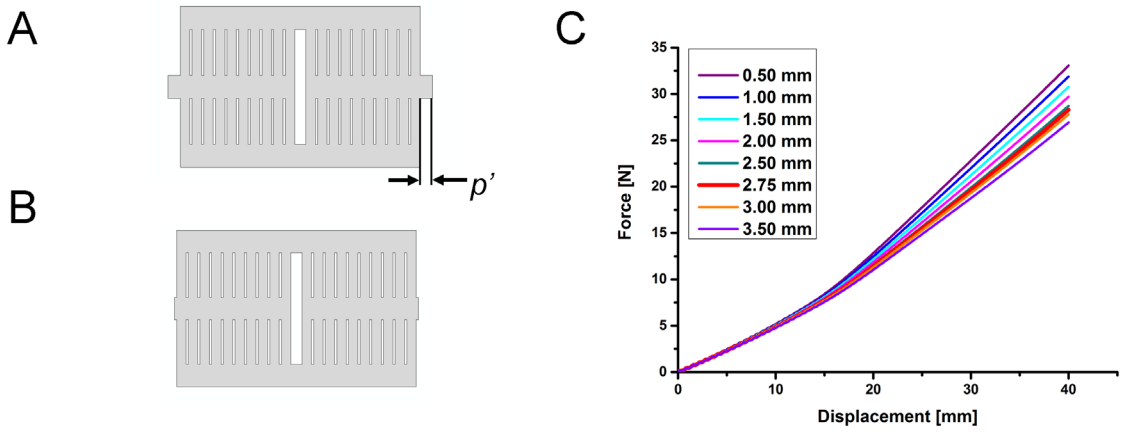

Figure 4.21A: Geometry of the demonstrator sample. B: Geometry of a sample with decreased protrusion length *p'* compared to the demonstrator sample. C: Simulated force-displacement curves for different protrusion-lengths.

4.3.7. Influence of sample-depth

From the discussion in the previous sub-chapters, it can be expected that the force-displacement behavior scales linearly with the sample-depth *D* as the stiffness of all parts of the sample scales linearly with their depth (equation 4.4 and 4.5). To prove this, a series of simulations with different sample-depths was conducted in this sub-chapter. The resulting simulated force-displacement curves are shown in Figure 4.22C. Additionally, the geometry of a sample with a decreased sample depth in comparison to the demonstrator sample (Figure 4.22A) is shown in Figure 4.22B.

As it can only hardly be detected from force-displacement curves if all values scale linearly with sample depth, additionally stress-strain curves, calculated from the simulated force-displacement curves, are shown in Figure 4.22D. As the stress is a normalized value for the force, the influence on the depth should vanish and all stress-strain curves should be the same. For the calculation of the stress, from the given forces, the force needs to be divided by the area the force is acting on. As this area not constant for the strain-stiffening samples, the area of the cross-section of the backbone, represented by its thickness and depth, as shown in chapter 4.3.1.1 was used.

Figure 4.22D shows that the stress-strain curves for different sample-depths are the same. It can be concluded that a change of sample-depth linearly changes the force-displacement behavior of the sample.

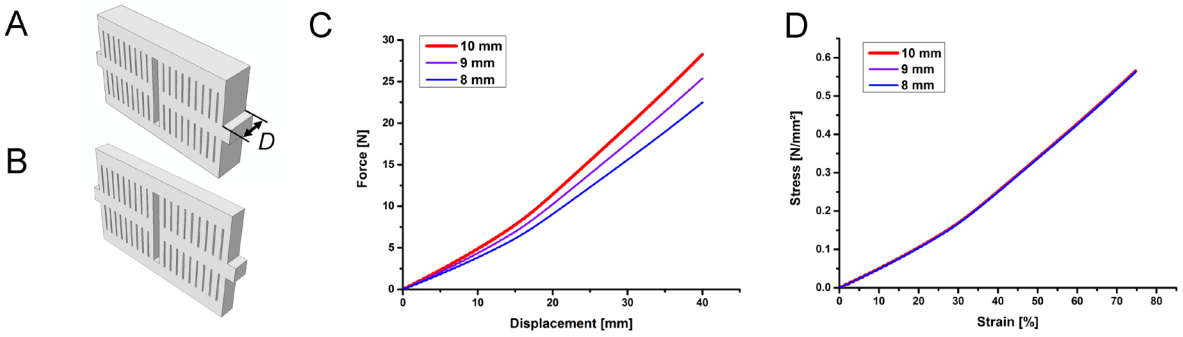

Figure 4.22A: Geometry of the demonstrator sample. B: Geometry of a sample with decreased depth *D* compared to the demonstrator sample. C: Simulated force-displacement curves for samples with different sample-depths. D: Stress-strain curves, based on the simulated force-displacement curves, for samples with different sample-depths. As an area for the calculation of the stress, the cross-section of the backbone was used.

4.3.8. Influence of friction

Not only was the influence of the sample´s geometrical features on its strain-stiffening behavior simulated, but also the influence of friction. Unfortunately, the friction between silicone surfaces is to my best knowledge not documented in the literature. The coefficient of friction used for the demonstrator sample in the simulations was chosen to be 0.05. It is in the range of the friction between Teflon and a polished metal [147] and therefore likely to be much lower than the friction between silicone surfaces. As a comparison, two values for the coefficient of friction that lie above and below values for the friction of rubber on hard surfaces found in the literature are used in a series of simulations [147, 148]. They are supposed to represent the friction between silicone surfaces to a higher degree. The resulting simulated force-displacement curves are shown in Figure 4.23.

The results show that there is no influence on the initial stiffness, but an increase of final stiffness with increasing coefficient of friction. It was expectable that the friction has no influence on the initial stiffness as the slats do not touch in this regime, whereas they do for larger displacements.

In chapter 4.3.1.4 it was described that the increase of stiffness of the slats is caused by two effects. One effect is most likely influenced by friction. It was stated that slats that touch over a large part of their length can be regarded as a single slat with a width that is equal to the sum of their individual widths. As the stiffness of the slat scales to the power of 3 with the width, the stiffness of the slats would increase drastically. In chapter 4.3.1.4 certain limitations to this effect were presented. One of them was the ability of the slats to glide over each other. The coefficient of friction has an influence on the ability of the slats to glide over each other. At low friction, it is easier than at high friction. In the case of high friction, it is likely that the described drastical stiffening occurs to a higher degree than in the case of low friction. Consequently, the stiffness of the slats is higher at higher coefficients of friction. This explains the increase of final stiffness.

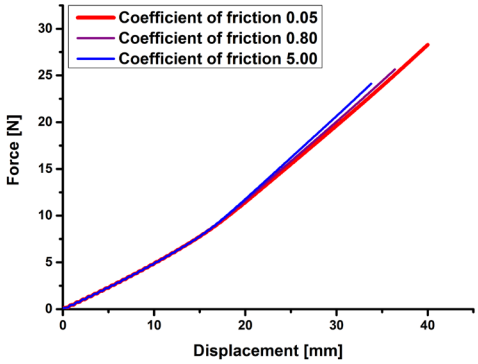

Figure 4.23: Simulated force-displacement curve of samples with different coefficients of friction between the slat surfaces. Due to a non-converging FEM simulation in the case of a coefficient of friction of 0.8, it was conducted to a displacement of 35 mm and in the case of a coefficient of friction of 5, it was conducted to a displacement of 33 mm. This was still sufficient to see their influence on the strain-stiffening behavior.

4.3.9. Overview of parameters influencing the strain-stiffening behavior of the structure

In the FEM simulations in the previous sub-chapters, several parameters influencing the strain-stiffening behavior of the sample were analyzed. The variation of the dimension of a certain parameter has a certain influence on its stiffness. As the variation of the dimension of that certain parameter comes in most cases with a variation of the backbone-length, its influence on the general strain-stiffening behavior of the structure is superimposed by this behavior. Table 4.2 summarizes all results from the previous sub-chapters by listing the analyzed parameters, the influence of a variation of their dimension on their stiffness and their influence on the strain-stiffening behavior of the sample.

Table 4.2: List of parameters influencing the force-displacement behavior of the sample in the first column, the influence of a variation of the dimension of their stiffness in the second column and their influence on the strain-stiffening behavior of the sample in the third column.

Parameter	Influence on stiffness	Influence on strain-stiffening behavior
Backbone-thickness h	Linear increase of stiffness with increasing backbone-thickness.	Small increase of initial stiffness, large increase of final stiffness with increasing backbone-thickness.
Backbone-length	Linear decrease of stiffness, with increasing backbone-length	Small decrease of initial stiffness and large decrease of final stiffness with increasing backbone-length.
Slat-width w	Increase of stiffness to the power of 3 with increasing slat-width	Large decrease of initial stiffness due to decrease of slat-width, and large increase of final stiffness due to the change of backbone-length that comes with decrease of slat-width.
Distance between slats d	No direct influence on stiffness.	Shift of point of stiffening towards lower displacements with decrease in distance between slats. Small increase of initial and final stiffness due to decrease of backbone-length with decreasing distance between slats.
Number of slats N	Linear increase of stiffness with increasing number of slats.	Increase of initial stiffness with increasing number of slats. Decrease of final stiffness with increasing number of slats due to increasing backbone-length.
Protrusion-length p'	Linear decrease of stiffness with increasing protrusion-length.	Small increase of initial stiffness and large increase of final stiffness with decreasing protrusion length
Sample-depth D	Linear increase of stiffness with increasing sample-depth.	Linear increase of the entire force-displacement curve with increasing sample depth.
Friction between slats	Increase of stiffness with increasing coefficient of friction.	Increase of final stiffness with increasing coefficient of friction. Initial stiffness stays constant.

4.3.10. Experimental characterization of silicone samples via tensile tests

The demonstrator sample and four representative other geometries have been tested in a tensile test, to validate the results of the FEM analysis. In addition, also the influence of friction between slats was tested to confirm its influence on the final stiffness of the structure.

In Figure 4.24A a simulated and the measured force-displacement curve of the demonstrator sample are shown.

In Figure 4.24B the five different geometries that were tested are shown. The demonstrator sample is named *DS*. It has a slat-width w of 2.1 mm, a backbone-thickness h of 5 mm and the distance between the slats d is 0.5 mm. In the other samples, one or two parameters are changed in comparison to the demonstrator sample. The sample where slat-width w is reduced to 1.3 mm is named $S_{w\_1.3}$, the sample where the backbone-thickness h is increased to 10 mm is named S_{h_10}, the sample with reduced slat-width w (1.3 mm) and increased backbone-thickness h (10mm) is named $S_{w\_1.3\_h\_10}$ and the sample increased distance between slats d (2.5 mm) is named $S_{d\_2.5}$. In the force-displacement curves of the sample in Figure 4.24C the geometries are represented by the regarding name. The same holds for the following description and discussion of the results. In Figure 4.24D the force-displacement curves of tensile tests with the samples *DS* and S_{h_10} with oil and without oil between the slats are presented. Due to restrictions in the measurement setup, the tensile tests were only conducted up to a displacement of 30 mm compared to the displacement of 40 mm simulated in the FEM simulations. This was still sufficient to see all important influences of the parameters on the stiffening behavior.

The comparison of the simulated and the tensile test data of the demonstrator sample in Figure 4.24A shows that their behavior is generally the same. Both curves show a constant initial stiffness up to a displacement of ~15 mm and a constant final stiffness from a displacement of ~18 mm. The only difference is that the simulated initial and final stiffness is higher than the measured one. A similar behavior can be found when comparing the simulated and tensile test data of the other geometries (see Figure 2.25D). As the simulated force-displacement curves only differ from the measured curves in their absolute value but not in their general behavior, the influences listed in Table 4.2 in chapter 4.3.2.9 should also apply to the measured geometries. This will be discussed in the following:

Sample $S_{w\_1.3}$, the sample with a decreased slat-width compared to the demonstrator sample *DS* shows a decreased initial stiffness and an increased final stiffness, compared to the demonstrator sample (see Figure 2.24C). The stiffening takes place at roughly the same displacement. This behavior follows exactly the behavior determined via FEM analysis. The decreased initial stiffness arises from the decreased stiffness of the slats. It scales with the power of 3 with the slat-width. A decrease will, therefore, lead to a decrease in stiffness. The increase in final stiffness is caused by the decrease in backbone length due to the decreased slat-width. A shorter backbone is stiffer and will lead to an

increased final stiffness. As the distance between the slats was not changed, the displacement where the stiffening occurs should stay the same.

Sample S_{h_10}, the sample with an increased backbone-thickness, compared to the demonstrator sample *DS* shows a slightly higher initial stiffness and a clear increase of final stiffness, compared to the demonstrator sample (see Figure 2.24C). The stiffening occurs at a similar displacement. This behavior follows exactly the behavior determined via FEM analysis. The increase in initial stiffness can be explained with a decreased influence of the backbone on the stiffness of the sample, due to its increased thickness and consequently increased stiffness. The increase of final stiffness can also be explained with an increase of backbone-stiffness due to the increased thickness. As the distance between slats has not changed, a shift of the displacement at which the stiffening takes place was not expected.

Sample $S_{w\_1.3\_h\_10}$, the sample with an increased backbone-thickness and a decreased slat-width compared to the demonstrator sample *DS* shows a decreased initial stiffness and increased final stiffness compared to the demonstrator sample (see Figure 2.24C). The decreased initial stiffness is caused by the decreased slat-width and the increased final stiffness is caused by a superposition of the increased stiffness of the backbone due to its decrease in length caused by the decreased slat-width and the increased backbone-thickness. The slat-width of sample $S_{w\_1.3}$ and $S_{w\_1.3\_h\_10}$ is the same. This explains why their initial stiffness is the same. The backbone-thickness of sample S_{h_10} and $S_{w\_1.3\_h\_10}$ are the same. Caused by the fact that the backbone-length of sample $S_{w\_1.3\_h\_10}$ is shorter than the backbone-length of sample S_{h_10}, the final stiffness of sample $S_{w\_1.3\_h\_10}$ is slightly higher than the final stiffness of sample S_{h_10}.

Sample $S_{d\_2.5}$, the sample with an increased distance between slats compared to the demonstrator sample *DS*, shows a decreased initial and final stiffness compared to the demonstrator sample (see Figure 2.24C). This decrease can be explained by the increase in backbone-length due to the increase in the distance between the slats. In this special sample, another effect occurs. Due to the largely increased distance between the slats, they do not touch in response to the displacement. This explains why there is no stiffening-effect visible in the force-displacement curve.

By introducing silicone oil on the surfaces of the slats, the friction of these surfaces was drastically decreased. This situation of decreased friction was compared to the initial situation of the sample. The test was conducted with the demonstrator geometry and sample S_{h_10} as the stiffening effect was more pronounced in this sample. In both samples, the final stiffness is clearly decreased by the introduction of oil, compared to the situation without oil, while the initial stiffness stays constant (see Figure 2.24D). This can be explained by the influence of the oil on the friction between touching slats. The stiffness of the block of touching slas is decreased with decreased friction. As only touching slats are influenced by the oil, the initial stiffness stays constant.

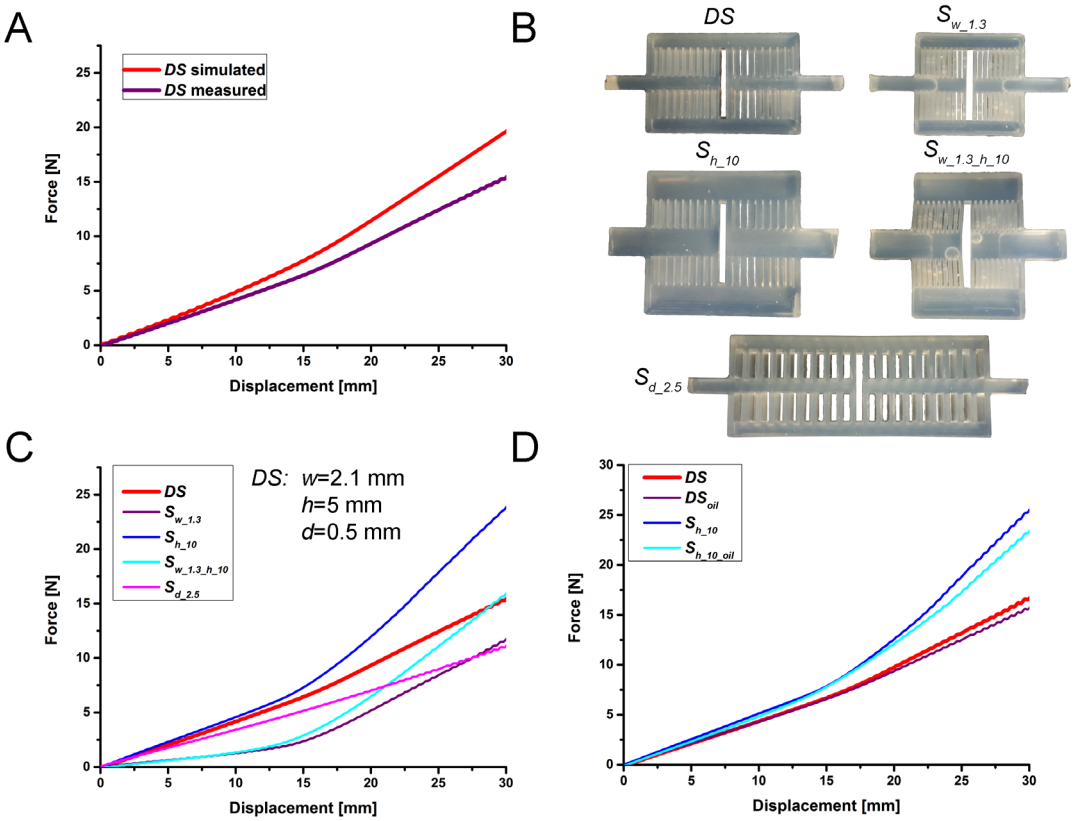

Figure 4.24A: Simulated and measured force-displacement curve of the demonstrator sample. B: Pictures of the geometries that were tested in a tensile test setup. The demonstrator sample *DS* has a slat-width *w* of 2.1 mm, a backbone-thickness *h* of 5 mm and the distance between the slats *d* is 0.5 mm. The deviations of the other geometries from the demonstrator sample are identified in the subscripts of their names. C: Measured force-displacement curves of the samples shown in B. D: Measured force-displacement curves for two samples from B. Measured force-displacement curves of two samples with oil between the slats and without oil between the slats.

Figure 4.25A shows the initial and final stiffness of the samples with different geometries. The values were derived from tensile tests. For each geometry, three samples were tested and for each sample, 10 tensile tests were conducted. While there was no mentionable deviation between the tensile test curves for every single sample there was a certain deviation between the tensile test curves of the three samples of each geometry. The error bars in Figure 4.25A represent the minimum and maximum stiffness measured for each geometry and the actual marker labels the average stiffness. The deviation is large for the final stiffness of the samples and especially large for the final stiffness of the samples S_{h_10} and $S_{w\_1.3\_h\_10}$.

The deviation in final stiffness is most likely caused by the clamping of the sample in the tensile test setup. It was shown in the FEM simulations in chapter 4.3.6 that the length of the protrusion that represents a part of the backbone that is not clamped (p') has a large influence on the final stiffness of the sample. It is likely that a sample that is clamped directly at the beginning of the protrusion has a higher final stiffness than a sample that is clamped further away from the beginning of the protrusion. Both cases of clamping are shown in Figure 4.25B. In samples S_{h_10} and $S_{w\_1.3\_h\_10}$ the effect of clamping is superimposed by another effect. Both samples have an increased backbone-thickness compared to the demonstrator sample. A detailed analysis of the samples has shown that especially samples with a thick backbone show a high variance in backbone-depth (D). As the stiffness of the backbone depends on the depth to the same degree as it depends on the thickness (equation 4.4), a decreased depth leads to a decreased backbone stiffness. The stiffness of the backbone has a large influence on the final stiffness. The large variance in backbone-depth is caused by the molding process. The molds used for the experiments are open on the top. If not enough silicone is filled in the molds the area of the backbone shows a void. This is shown in Figure 4.25C. The result is a decreased backbone-depth.

As described before, the simulated values for the initial and final stiffness are higher than the measured ones. This is shown in Figure 4.25D. This could have two reasons. The first one could be the mesh size used in the analysis. Tests have shown that the initial and final stiffness of the sample is decreased with decreased mesh size. Theory states that there is a certain mesh size upon which a further decrease does not change the results [149]. Before this saturation was reached, the maximum number of nodes for the software used for this work was reached, allowing no further decrease in mesh size. The second reason could be the material model. The material model used for the simulation is taken from a publication by Chen et al. [145], who used tensile test data for the derivation of the model. In literature, a large range of stiffness, determined from tensile test data can be found for Elastosil RT625 [95, 145, 150]. The stiffness of the Elastosil RT625 used by Chen et al. for the derivation of the material model is the highest. Consequently, it is possible that the material used in the tensile test in this chapter is softer than the material used for the determination of the material model by Chen et al.

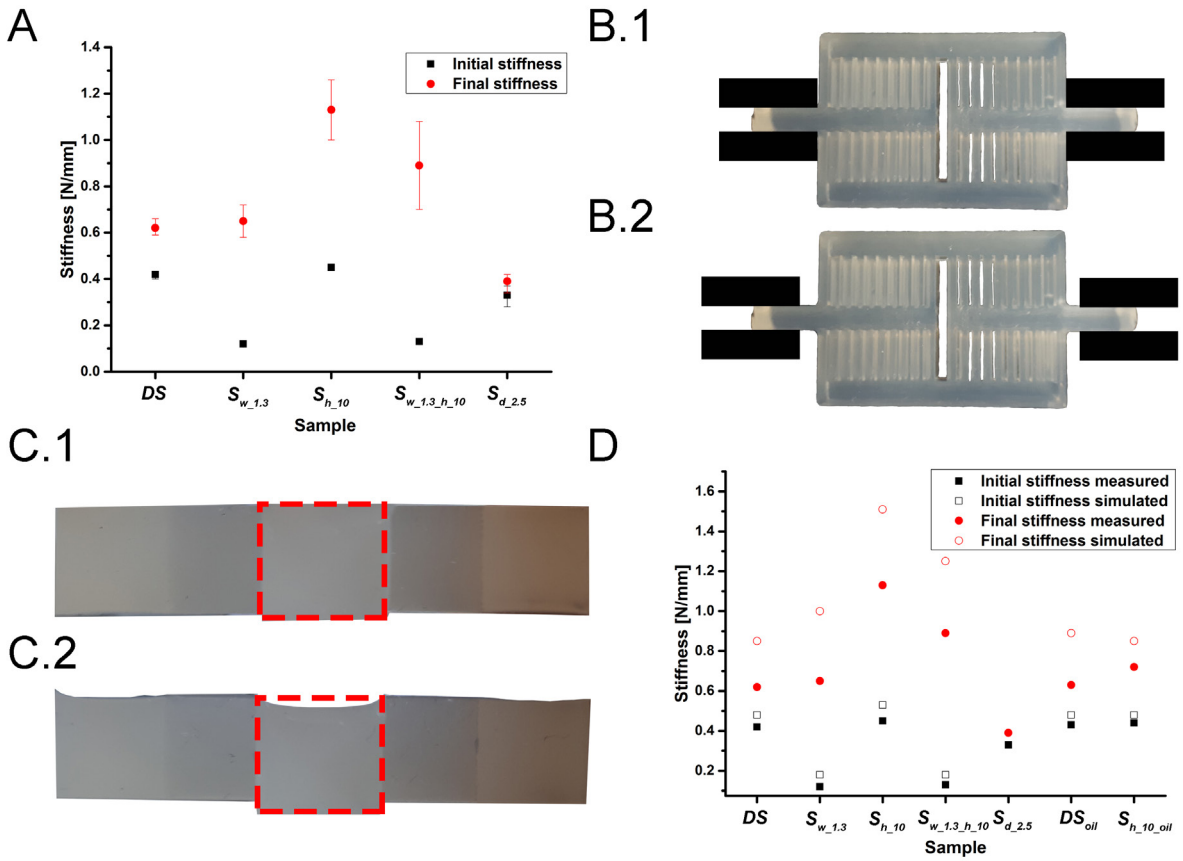

Figure 4.25A: Initial and final stiffness of the samples measured in a tensile test. For each test 3 samples with the same geometry were used. The average is marked in the plot and the error bars represent the minimum and maximum value. B: Two possible ways of clamping a sample in the tensile test setup. The black rectangles represent the clamps. B.1: Sample that is clamped directly at the beginning of the protrusion. B.2: Sample that is clamped further away from the beginning of the protrusion. C: Front view of two different samples with the geometry S_{h_10}. The red boxes mark the area of the backbone. While it is completely filled with silicone in C.1, it is not completely filled in C.2. D: Initial and final stiffness determined via FEM simulation and tensile test measurements for the different samples. For sample $S_{d\_2.5}$ no FEM simulation was conducted.

4.4. Conclusion

In the presented FEM simulations a demonstrator sample that showed a certain amount of strain-stiffening was introduced. Several geometrical parameters of this sample were systematically altered FEM simulations and the influence of these parameters on the strain-stiffening behavior was determined. It was possible to explain the influence of all tested parameters and it was possible to predict the initial stiffness for a certain geometry with an analytical approach. This analytical approach was not applicable to the final stiffness, as the stiffness of certain parts of the geometry was not reliably predictable. Experimental tensile tests with representative geometries supported the conclusions that were taken to describe the influence of geometrical features. Additionally, the influence of friction between the samples was analyzed via FEM simulation and tensile tests. It could be shown that the final stiffness of the sample is influenced by friction. Generally, the tensile tests showed the same

behavior as the simulated results but led to a lower initial and final stiffness. This was either caused by a too large mesh size or a material model that was determined with a material that was too stiff.

In order to match the tensile tests with the FEM simulation, in the future two improvements should be incorporated. It has been shown that the stiffness of the entire sample can be described by just describing one part of the sample, the quarter-structure. It has additionally been shown that the force-displacement behavior scales linearly with sample depth. These two features can be exploited to decrease the mesh size. If only the quarter-structure with a lower depth would be simulated, the size of the simulated geometry is drastically reduced compared to the simulations conducted in this chapter. Consequently, the mesh size can be further reduced until the maximum number of nodes is reached. Another alternative would be to change to a program without limitations in the number of nodes. It is also possible to determine the parameters for the material model with measured data from the exact same material and with that match the model with the real results. For this work the accuracy of the simulation was sufficient as the qualitative behavior of the simulation and the tensile tests matched perfectly and the role of geometrical feature could be determined.

With the help of simulations, it could in the future be possible to find a way of predicting the stiffness of the parts of the backbone that has not been described yet. This would allow an exact analytical description of the initial and final stiffness and would ideally supersede the FEM simulation.

4.5. Materials and Methods

4.5.1. FEM simulation

In this sub-chapter, the different settings in the program Abaqus 6.13 (Simulia, USA), that were done to achieve the simulated force-displacement behavior of the sample, are listed. The headlines of the following sections are named after the different modules in the program.

4.5.1.1. Module „Part“

In this module, the actual shape of the part was defined. A cuboid solid with the depth and the outer dimensions of the sample was constructed and all features like the gaps between slats and parts to form “clamps” were cut out from the cuboid to yield the final shape. The sample was divided into partitions along slat walls to make the future mash applicable and the slats walls that were supposed to touch during the simulation were defined as surfaces. Figure 2.26 shows the steps to visualize it.

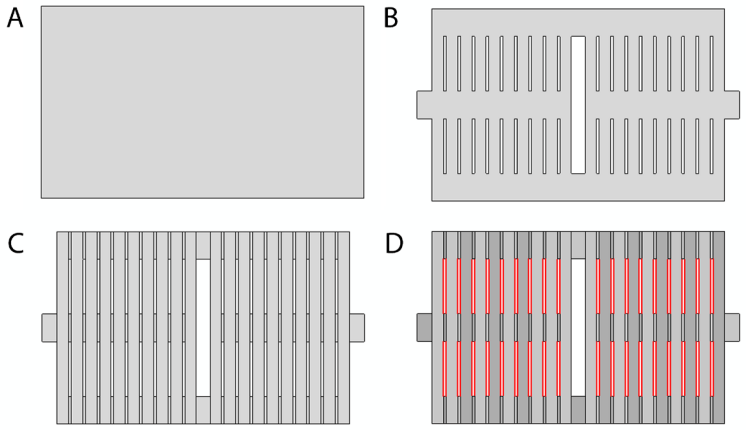

Figure 4.26: The four steps in the module "Part" in Abaqus. A: A cuboid structure is constructed. B: Several parts are cut out. C: The structure is divided into several partitions and D: Slat walls are defined as surfaces.

4.5.1.2. Module "Properties"

In this module, the material of the sample during the simulation was defined. In the case of the standard sample, two material behaviors for the silicone Elastosil RT625 (Wacker) were provided: The density, derived from the material data sheet [87], and the hyperelastic material parameters. These parameters were taken from Chen et al. [145] where the Yeoh model was chosen to describe the hyperelastic properties of this specific material. All parameters are listed in Table 4.3.

Table 4.3: Mass density and hyperelastic material parameters for the Yeoh model describing the silicone Elastosil RT625

Mass density	μ_1	μ_2	μ_3
1.31 g/cm3	*0.148*	-0.009	0.004

The material was applied to the part in the form of a solid homogeneous section.

4.5.1.3. Module "Mesh"

In this module, the sample was meshed. Global seeds were defined by setting the approximate global size to 0.5 and then a mesh with C3D8RH elements was constructed. The sample with the mesh is shown in Figure 4.27. These elements are defined by Abaqus as "8-node linear brick, hybrid, constant pressure, reduced integration, hourglass control" and described being well suitable for the type of simulation [149].

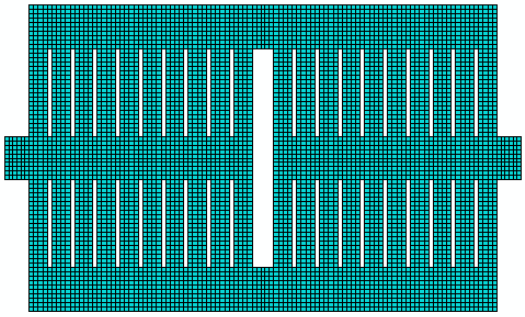

Figure 4.27: Sample with the applied mesh of 8-node linear brick elements.

4.5.1.4. Module "Assembly"

After meshing of the part, three sets of nodes were defined in the assembly module. These node sets play an important role in some of the next modules. The first set of nodes was composed by all nodes on the outer surface of the left clamp. These nodes were supposed to be fixed during simulation. The node set was therefore called "fixed nodes". The second set of nodes was composed by one single node on the outer surface of the right clamp. It was the so-called "load node", as this node represented the load during the tensile test. The third set of nodes was composed of all the other nodes on the same surface. It was called "following nodes", as their properties were later connected to the load node. Details are shown in Figure 4.28.

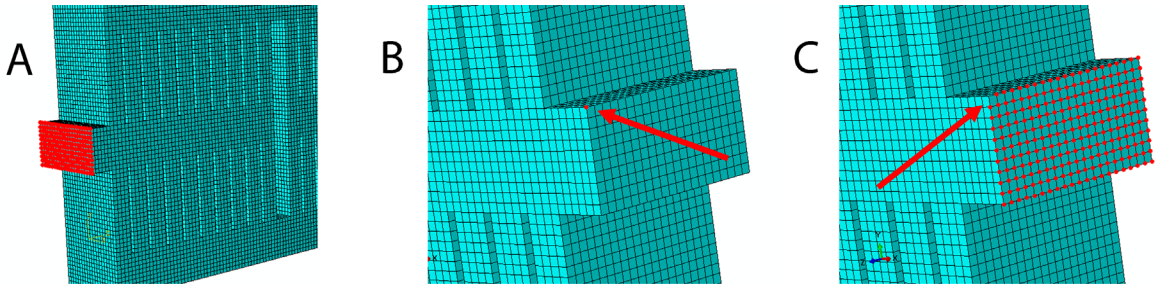

Figure 4.28: Node sets defined in the Assembly module. A: One set, the "fixed nodes" is composed of all nodes on the outer surface of the left clamp. B: The "load node" is a single node on the outer surface of the right clamp C: The "following nodes" are all other nodes on this surface.

4.5.1.5. Module "Interaction"

In this module, the interaction of parts of the sample was defined. First, for each pair of touching surfaces between slats, a surface-to-surface contact was defined and the coefficient of friction between these surfaces was set to 0.05. Second, an equation constraint between the "load node" and the "following nodes" was defined by setting the "following nodes" to a coefficient of 1 and the "load node"

to a coefficient of -1. By this constraint, all deformations defined to act on the “load node” were set to act on the “following nodes”, too. This allowed to read out the force that acted on this special node in the analysis after the simulation. This force represented the force on the entire surface and could be used to describe the force-displacement behavior of the entire sample.

4.5.1.6. Module “Load”

In this module, the deformation of the sample that was actively applied during the simulation was defined. First, an amplitude was defined that increased linearly between 0 and 1. Second two boundary conditions were defined. The “fixed nodes” were set to be encastered. This means that no translation or rotation in any direction was allowed. This should simulate the fixed clamped end of the sample. A displacement boundary condition was applied to the “load node”. A displacement of 40mm in one direction was allowed and all other translations and rotations were inhibited. The earlier defined amplitude was applied to this boundary condition to ensure a linear increase of displacement between the beginning and the end of the simulation. This is simulating the elongation of the sample in the tensile test.

All described settings allowed the simulation of a tensile test of the sample. For the analysis in this work mainly the force-displacement behavior of the “load node” that represented the force-displacement of the entire sample was analyzed. For each simulation, 500 evenly spaced displacement values and the regarding forces were available and could be analyzed the same way as force-displacement values from mechanical tensile test tests. To modify the geometry of the sample, in order to determine the influence of geometry on the force-displacement behavior, the shape of the model was changed in the first module and then the settings in all other modules were adapted to the new shape. To detect the influence of friction only the coefficient of friction in the interaction module had to be changed.

4.5.2. Experiments on polymer samples

The tensile tests in this chapter are conducted in a tensile test setup that was built by the members of the working group of Prof. Adelung. It featured a stepper motor (PD57-2-1161-TMCL, Trinamic, Germany) that provided a tension by driving a threaded rod with a slope of 0.5 mm, and a load cell (Kmm 62 500N, Inelta, Germany) to measure the force. Information about the measured force was transferred to a Labview program (National Instruments, USA) over a data acquisition board (USB-2537, Measurement Computing, USA) and a custom-made amplifier. Pictures of the tensile test setup are shown in Figure 4.29.

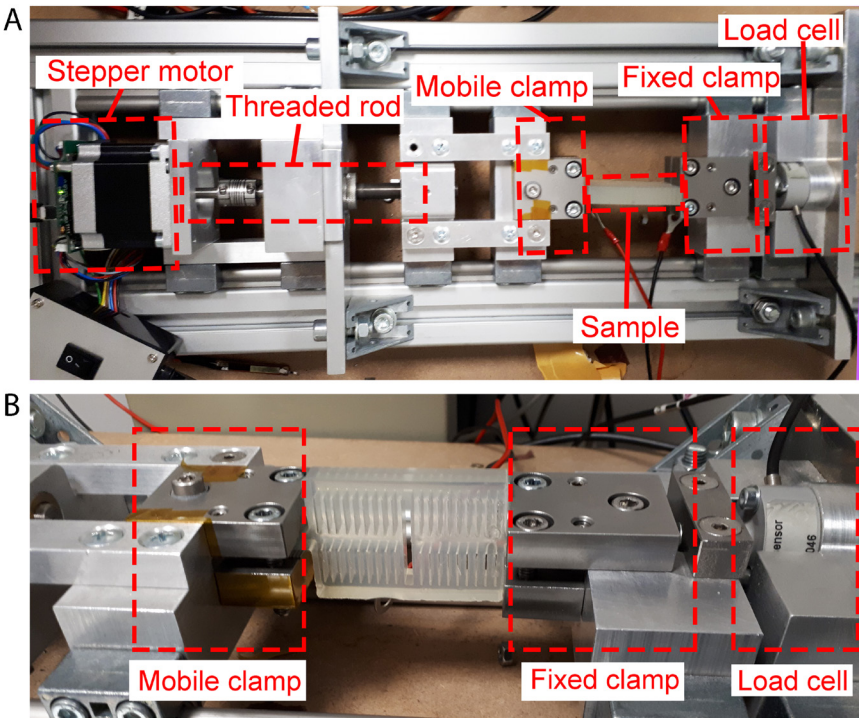

Figure 4.29A: Top view of the tensile test setup. The sample is fixed in two clamps. The fixed clamp is attached to the load cell and the mobile clamp is attached to the threaded rod that is driven by a stepper motor. B: Side view of the tensile test setup.

The tensile tests were conducted with a speed of 0.5 mm/s and up to a displacement of 30 mm. In the tests where the friction between the slats was decreased by introducing oil, silicone oil for oil baths (Sigma-Aldrich/Merck, Germany) was used. Samples were made from the silicone Elastosil RT625 (Wacker, Germany). The two components of the silicone, A and B, were mixed according to the manufacturer´s instructions [87] in a 9:1 ratio. The mixture was degassed in a desiccator and poured in a mold. After a second degassing step in the desiccator, the polymer was cured in an oven at 70°C for 1 hour. The molds were milled from solid aluminum blocks. A sketch of the molds is shown in Figure 4.30. At the end of each clamp, a spare part was added. It that could be destroyed when taking the sample out of the form and was cut off to form the final sample.

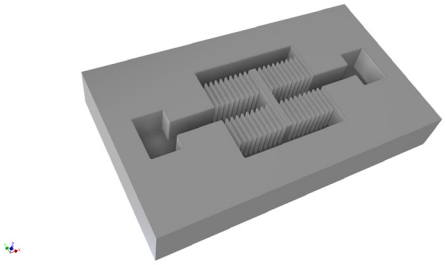

Sketch of a mold for the production of silicone samples for tensile tests.

For each of the geometry related tests, three samples of the same geometry were measured for 11 cycles. The first cycle was discarded as an initial slipping of the sample in the clamps occured. To present the results, the 10 curves for one sample are combined into one curve by an averaging algorithm in the software Origin 9.1 (OriginLab, USA). This was possible as there was no notable difference between the curves. As there was a certain difference between the averaged curves of the three samples of each geometry, they were are again combined into one with the help of the averaging algorithm. The average curve was used to present the general strain-stiffening behavior of a certain geometry, the minimum and maximum values were used as information for the error bars.

For the friction related tests, only one sample per type was used. It was measured without oil and afterward with oil. Again, 11 curves were measured for each sample in each state and the last 10 curves were combined to a single curve with the averaging algorithm in Origin 9.1, to show the general force-displacement behavior

4.5.3. Determination of stiffness from measured and simulated curves

The stiffness of a sample is the slope in its force-displacement curve. To determine the initial and final stiffness of a sample the slopes of the representing parts of the curve had to be determined. This was done by fitting a line to each section of the curve. The size of the section was determined for each curve individually. It was chosen to be as large as possible, but small enough to represent a purely linear section. The fit was conducted with the software Origin 9.1.

5. Conclusion and perspective

In this thesis, two strategies were presented how biomimetic structures of silicones can be used in two very different types of applications. Micro-pillar arrays were used to represent the confinement cells encounter in the extracellular matrix and cell-inspired structures showed strain-stiffening behavior.

5.1. An artificial extracellular matrix

A.castellanii adapted their vacuole diameter to the available space inside micro-pillar arrays in order to be able to intrude them. This showed the cell´s ability to actively adapt internal structures to spatial confinements, which are also common in the extracellular matrix in body tissue. In further experiments, *A. castellanii* phagocytosed stiff artificial micro-particles. Particles that were smaller than the distance between the pillars in the structure did not significantly influence the migration behavior of the cells. In the cases where *A. castellanii* had phagocytosed particles that were at least in one dimension larger than the gap between the pillars, most cells were completely hindered in their movement. Still, some cells showed remarkable problem-solving skills to enter the structure or move inside the structure. These approaches gave new insights into the cells´ ability to act as an intelligent and active system. The approach of the cell to lift the artificial cargo above the pillar structure in order to migrate through it proved their ability to sense spatial information about their environment and to choose a method of minimal effort for migration. Their approach of selectively guiding or even twisting particles such that cell movement inside the structures is possible indicates that the cells have a mechanism to sense the orientation of phagocytosed particles and to actively adapt to external confinements. Some cells actively dragged particles through the gap between neighboring pillars and thereby deformed the pillars. This allowed an indirect measurement of the forces the cells are able to apply on phagocytosed particles.

Therefore, micro-pillar arrays are a suitable system to provide spatial confinements for *Acanthamoeba* trophozoites and to modulate their motion. The results of the experiments might be the foundation for novel strategies to prevent *Acanthamoeba*-born diseases. These might in the future include ways of stopping amoeba from entering body tissue by letting them phagocytose particles that hinder their movement inside the body tissue. Another method could be to lure amoeba into artificial pillar structures and let them phagocytose particles that do not allow them to leave the structure.

Information about cell migration in micropillar arrays can be adapted to the migration behavior of other pathogenic microorganisms, or migrating cancer cells. Cancer cells that form metastases migrate through body tissues in a similar way as *Acanthamoeb*a trophozoites. Consequently, methods of cell-trapping might be applied in this field in the future, too.

A further interesting aspect to study would be the impact of particle stiffness on the capture of *A. castellanii* by the micropillar arrays. A method of producing monodisperse alginate micro-spheres

was developed together with Saman Stölting during the course of this thesis [151]. These microspheres are very soft (~50 kPa [152]) compared to the ones used in the described experiments (~3 GPa [153]). It will be exciting to see how *A. castellanii* adapts its behavior inside micro-pillar arrays after phagocytosing such soft particles and how it transports particles of different stiffness.

5.2. A strain-stiffening structure

Biomimetic strain-stiffening has been demonstrated by shaping silicone in a way that it shows an increasing stiffness in response to elongation. The general concept for shaping the material was adopted from the ability of cells to actively cross-link parts of their cytoskeleton to increase their stiffness. The biomimetic strain-stiffening structure presented consists of four sets of slats elastic that were connected via a backbone made of the same elastic material. The influence of several geometrical features, as well as the influence of friction between the slats, was determined by FEM simulations and conclusions about these influences were proven by experiments using tensile tests.

All samples regardless of their specific geometry showed an initial linearly increasing force-displacement curve, representing the initial stiffness of the material. After a certain displacement, the slope of the force-displacement curve started to increase to finally show a linearly increasing force-displacement behavior with an increased stiffness, compared to the initial stiffness. This was the final stiffness of the sample.

The main influences that determined the strain-stiffening of the sample are the following: (1) The thickness of the backbone mainly influences the final stiffness of the geometry. An increase of backbone thickness leads to an increase of final stiffness. (2) The thickness of the slats influences the initial stiffness. A decrease in thickness of the slats leads to a decrease of the initial stiffness. (3) The distance between the slats was shown to influence the displacement at which the structure starts to stiffen. An increased distance between the slats leads to a stiffening at larger displacement. (4) The friction between slats influences the final stiffness of the sample. An increase in friction leads to an increase in final stiffness.

The presented method of introducing strain-stiffening into a material by biomimetic structuring is simple to achieve but to my best knowledge completely new. This was supported by the acceptance of the patent “Schicht mit variabler Festigkeit” [146] and the patent search prior to the application of the patent “Progressives Auslenkungselement, Herstellungsverfahren dazu sowie Verwendung” by the PVA Schleswig-Holstein.

The biggest advantage of the method is, that it is based on the pure structure of a material. This allows several degrees of freedom in the design of such strain-stiffening materials and provides several unique features. Generally, all materials that can deform elastically can be shaped to show strain-stiffening. This includes biocompatible materials. As there is no further chemical modification

of the material, a biocompatible material will stay biocompatible in the strain-stiffening geometry. The effect is completely reversible. If a purely elastic material is used, the strain-stiffening effect is completely speed independent. The method is not limited to a certain length scale so that it can in principle be produced from the micrometer- to the meter-scale.

Three main future applications for the strain-stiffening structure were determined during the course of this thesis. They are shortly described in the next sub-chapters.

5.2.1. Strain-stiffening structures in soft-robotics

Supported by the recent advances in the design of intelligent soft materials and flexible sensor and actuator technologies, novel soft material robotic systems have been developed. These systems often referred to as soft robots, are autonomous machines that majorly consist of soft materials. In several cases, these materials have a stiffness that is comparable to that of soft biological tissues [154]. With the transition from rigid materials to soft materials, the design and modeling of robots have changed. While in conventional rigid-link robots only a finite number of degrees of freedom can be implemented, soft robots can have a virtually infinite number of degrees of freedom. Even though this high dexterity might generally be desirable, controlled movement can only be realized if there is a certain balance between compliance and internal kinematic constraints [155]. At this point strain-stiffening structures become important. They can be used to allow full flexibility to a certain degree of deformation and to act as constraint after further deformation.

Structures that show strain-stiffening in more than one direction might be desirable for the application in soft robotics. Such structures could be constructed by a combination of the pillar arrays from chapter 3 and the strain-stiffening structures presented in this thesis. In such structures the function of the slats is taken over by the pillars and the function of the backbone is taken over by the substrate below the pillars. Figure 5.1 shows several strategies to achieve layers with strain stiffening in different directions. Pillars with a square cross-section, shown in Figure 5.1A, represent the simplest method of combining pillar structures and strain-stiffening structures. A similar amount of stiffening should be observed by shearing the top-layer and the bottom-layer in the directions perpendicular to the pillar surfaces. A slightly more complex structure, shown in Figure 5.1B, can be obtained by using hexagonally arranged pillars with a triangular cross-section. In these samples, the stiffening should occur in the three directions perpendicular to the pillar surfaces. Figure 5.1C shows a very advanced method. Two samples with the same pillar arrangement are glued into each other to achieve an arrangement of pillars that provides a high degree of stiffening in certain directions and a low degree of stiffening in other directions. For these applications the possibility of producing the samples in the micrometer range might offer high potential as thin layers with special properties could be combined to increase the strain-stiffening effect.

The idea of using the strain-stiffening structures as parts of soft-robotic systems was included in a

project proposal for the Prioritiy Programme “Soft Material Robotic Systems” funded by the DFG (Deutsche Forschungsgemeinschaft), which was submitted in December 2017.

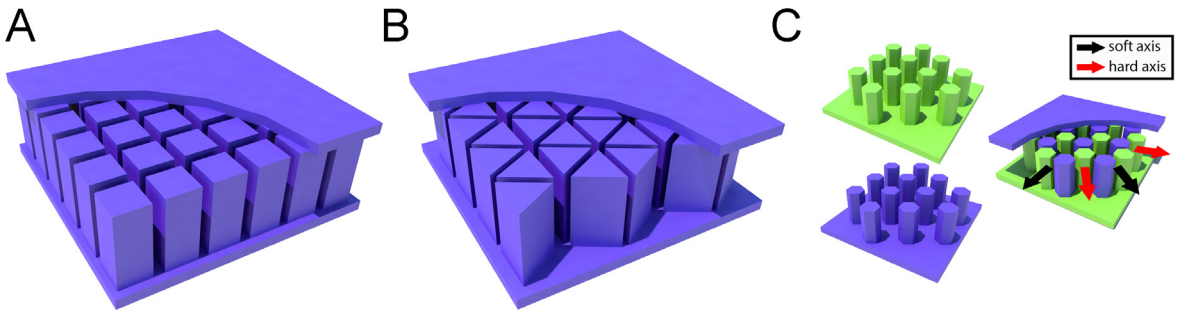

Figure 5.1: Structures with strain stiffening in more than one direction. The substrate on top of the pillars is partially removed in the graphic to show the arrangement of pillars below. A: Sample with pillars with a square cross-section. Stiffening can occur in the two directions perpendicular to the pillar surfaces by shearing the substrate above and below the pillars. B: Sample with pillars with a triangular cross-section. Stiffening can occur in the three directions perpendicular to the pillar surfaces. C: Structure with direction-dependent strain-stiffening. Two identical structures with specially arranged hexagonal pillars (green and purple) are glued into each other. The resulting arrangement provides directions where strong strain-stiffening is achieved (red arrows) whereas other directions appear soft (black arrows).

5.2.2. Strain-stiffening structures as parts of orthoses

In our society orthopedic disorders become increasingly prevalent. This might be caused by an increased average age and an increased life expectancy [156]. The result is a steadily increasing demand for orthotic devices, especially by elderly adults [157]. Current applications of orthotic devices range from bandages for the stabilization of joints after traumata or ligament ruptures to complex individually manufactured orthoses, like corsets or leg orthoses.

As in many fields, also in the field of orthotics, there is a constant need for improvement. One particular example that shows that need is the example of “genu recurvatum”. According to a study by Portnoy et al. 40-68% of poststroke patients, who regain walking ability, experience a symptom called genu recurvatum, a knee hyperextension, during the stance phase [158]. There are special orthoses available that could prevent this symptom, but they are not widely used, because of donning difficulties, unaesthetic appearance, and excessive weight perceived by the patient [158, 159].

Not only complex orthoses bear the danger that they might not be used due to such reasons. Even simple bandages include hard components that might be uncomfortable and can lead to severe pressure sores. An improvement of this situation is not only relevant for elderly patients, where the skin is sensitive and heals slowly, but also for pediatric orthoses, where comfort and aesthetic reasons play an important role.

The strain-stiffening material developed and investigated in this thesis is completely produced from flexible parts and thus might allow an improvement in the field of orthotics. Its ability to allow for full flexibility and softness to a certain degree and to provide support due to the stiffening at larger deformations, for example when carrying out a movement in the wrong direction, makes it a promising solution.

Soft strain-stiffening structures might in the future replace hard components that limit the degree of flexibility in conventional orthotic devices and could, therefore, be a part of lighter, easier to apply and more comfortable to wear orthoses. Especially the possibility to use 3D printable materials allows a very flexible design of orthotic devices with the strain-stiffening effect already included.

The idea of using the strain-stiffening structures as parts of orthoses was the basis of a project proposal for the Proof of Concept Grant funded by the ERC (European Research Council). It was submitted under the Acronym “STRAINSTIFF” and got accepted in May 2018.

5.2.3. Strain-stiffening structures as artificial blood vessels

In our aging society, not only an increase in demand for orthotics can be detected but also an increase in demand for synthetic vascular grafts. This is caused by a worldwide increase in cardiovascular diseases [160]. Today´s solutions, i.e. artificial blood vessels produced from polyethylene terephthalate and expanded polytetrafluoroethylene, are mainly used as large-caliber replacements (diameter >6 mm). As soon as they are used for smaller caliber applications the rate of failure is high. One of the main reasons for this failure is intima hyperplasia, an increase of blood vessel diameter, at the site of the junction to the artery. The causes for this intima hyperplasia are amongst others at compliance mismatch between the relatively rigid artificial vessel and the more elastic native vessel, and a lack of endothelial cells on the walls of the artificial vessel [161, 162]. In a review by Sarkar et al. [162] several characteristics are listed an ideal vascular graft should possess. These include mechanical strength and compliance to withstand long-term hemodynamic stresses, non-toxicity, biocompatibility and operative suturability. Especially the demand for compliance of mechanical properties between the artificial blood vessel and the native blood vessel might be satisfied with solutions including the strain-stiffening material, as studies have shown that arteries have a significant strain-stiffening that is similar to the effect generated by my material [163, 164].

Figure 5.2 provides the sketch of a possible method of including strain-stiffening structures into an artificial blood vessel. Several blocks with slats and backbones, the red structures in the sketch, can be combined to form a tube. This tube shows, similar to a real blood vessel, strain stiffening upon deformation in the radial direction. The blue structures in the sketch represent layers that might be included to have a smooth inner and outer surface of the vessel. Especially a smooth inner surface might allow an even blood flow. To allow an ingrowth of endothelial cells pores might be included in the backbones and additional layers.

If the vessels are made from silicone some other characteristics of an ideal vascular graft could be matched. Silicones can be produced to be non-toxic and biocompatible [86]. Some silicones, like Elastosil RT 625 provide an outstanding crack propagation resistance, which would provide the desired good suturability. Hence, the results achieved in this thesis are a promising starting point for further investigations in the field of synthetic vascular grafts.

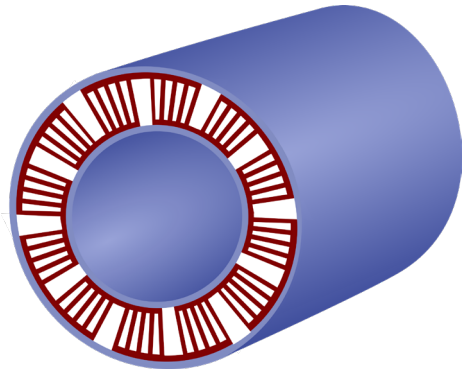

Figure 5.2: Sketch of the cross-section of a possible structure of an artificial blood vessel including strain-stiffening structures. It consists of a combination of several blocks of slats and backbones (red) and an additional layer on the inside and on the outside of the structure to provide smooth surfaces (blue). The structure would show strain-stiffening in radial direction.

Bibliography

[1] C. Suddath, A Brief History of: Velcro. [Online] Available: http://content.time.com/time/nation/article/0,8599,1996883,00.html. Accessed on: Oct. 12 2018.

[2] D. F. Larkin, S. Kilvington, and D. L. Easty, "Contamination of contact lens storage cases by Acanthamoeba and bacteria," The British journal of ophthalmology, vol. 74, no. 3, pp. 133–135, 1990.

[3] E. V. Wong, Cells: Molecules and mechanisms. Louisville, KY: Axolotl Academic Publishing Company, 2009.

[4] D. Sept and F. C. MacKintosh, "Microtubule elasticity: connecting all-atom simulations with continuum mechanics," Physical review letters, vol. 104, no. 1, p. 18101, 2010.

[5] Q. Wen and P. A. Janmey, "Polymer physics of the cytoskeleton," Current opinion in solid state & materials science, vol. 15, no. 5, pp. 177–182, 2011.

[6] G. M. Cooper, The cell: A molecular approach, 2nd ed. Washington, DC: ASM Press, 2000.

[7] C. Storm, J. J. Pastore, F. C. MacKintosh, T. C. Lubensky, and P. A. Janmey, "Nonlinear elasticity in biological gels," Nature, vol. 435, no. 7039, pp. 191–194, 2005.

[8] M. Nič, J. Jirát, B. Košata, A. Jenkins, and A. McNaught, IUPAC Compendium of Chemical Terminology. Research Triagle Park, NC: IUPAC, 2009.

[9] E. E. Charrier and P. A. Janmey, "Mechanical Properties of Intermediate Filament Proteins," Methods in enzymology, vol. 568, pp. 35–57, 2016.

[10] N. Mücke et al., "Assessing the flexibility of intermediate filaments by atomic force microscopy," Journal of molecular biology, vol. 335, no. 5, pp. 1241–1250, 2004.

[11] D. Boal, Mechanics of the Cell. Cambridge: Cambridge University Press, 2001.

[12] F. Huber, A. Boire, M. P. López, and G. H. Koenderink, "Cytoskeletal crosstalk: when three different personalities team up," Current opinion in cell biology, vol. 32, pp. 39–47, 2015.

[13] B. Geiger, J. P. Spatz, and A. D. Bershadsky, "Environmental sensing through focal adhesions," Nature reviews. Molecular cell biology, vol. 10, no. 1, pp. 21–33, 2009.

[14] A. de Donatis, F. Ranaldi, and P. Cirri, "Reciprocal control of cell proliferation and migration," Cell communication and signaling : CCS, vol. 8, p. 20, 2010.

[15] M.-R. Lee and T. J. Jeon, "Cell migration: regulation of cytoskeleton by Rap1 in Dictyostelium discoideum," Journal of microbiology (Seoul, Korea), vol. 50, no. 4, pp. 555–561, 2012.

[16] A. J. Ridley et al., "Cell migration: integrating signals from front to back," Science (New York, N.Y.), vol. 302, no. 5651, pp. 1704–1709, 2003.

[17] J. S. King and R. H. Insall, "Chemotaxis: finding the way forward with Dictyostelium," Trends in cell biology, vol. 19, no. 10, pp. 523–530, 2009.

[18] C. Y. Chung, S. Funamoto, and R. A. Firtel, "Signaling pathways controlling cell polarity and chemotaxis," Trends in biochemical sciences, vol. 26, no. 9, pp. 557–566, 2001.

[19] R. J. Petrie and K. M. Yamada, "Fibroblasts Lead the Way: A Unified View of 3D Cell Motility," Trends in cell biology, vol. 25, no. 11, pp. 666–674, 2015.

[20] L. K. Fritz-Laylin, S. J. Lord, and R. D. Mullins, "WASP and SCAR are evolutionarily conserved in actin-filled pseudopod-based motility," The Journal of cell biology, vol. 216, no. 6, pp. 1673–1688, 2017.

[21] T. Lämmermann and M. Sixt, "Mechanical modes of ‚amoeboid' cell migration," Current opinion in cell biology, vol. 21, no. 5, pp. 636–644, 2009.

[22] G. Charras and E. Paluch, "Blebs lead the way: how to migrate without lamellipodia," Nature reviews. Molecular cell biology, vol. 9, no. 9, pp. 730–736, 2008.

[23] F. Sabeh, R. Shimizu-Hirota, and S. J. Weiss, "Protease-dependent versus -independent cancer cell invasion programs: three-dimensional amoeboid movement revisited," The Journal of cell biology, vol. 185, no. 1, pp. 11–19, 2009.

[24] E. Sahai and C. J. Marshall, "Differing modes of tumour cell invasion have distinct requirements for Rho/ROCK signalling and extracellular proteolysis," Nature cell biology, vol. 5, no. 8, pp. 711–719, 2003.

[25] K. Wolf et al., "Compensation mechanism in tumor cell migration: mesenchymal-amoeboid transition after blocking of pericellular proteolysis," The Journal of cell biology, vol. 160, no. 2, pp. 267–277, 2003.

[26] W.-C. Lin, L.-C. Wang, T.-L. Pang, and M.-Y. Chen, "Actin-binding protein G (AbpG)

participates in modulating the actin cytoskeleton and cell migration in Dictyostelium discoideum," Molecular biology of the cell, vol. 26, no. 6, pp. 1084–1097, 2015.

[27] K. Yoshida and T. Soldati, "Dissection of amoeboid movement into two mechanically distinct modes," Journal of cell science, vol. 119, no. Pt 18, pp. 3833–3844, 2006.

[28] F. Marciano-Cabral and G. Cabral, "Acanthamoeba spp. as Agents of Disease in Humans," Clinical Microbiology Reviews, vol. 16, no. 2, pp. 273–307, 2003.

[29] H. Trabelsi et al., "Pathogenic free-living amoebae: epidemiology and clinical review," Pathologie-biologie, vol. 60, no. 6, pp. 399–405, 2012.

[30] M. Omaña-Molina et al., "Reevaluating the role of Acanthamoeba proteases in tissue invasion: observation of cytopathogenic mechanisms on MDCK cell monolayers and hamster corneal cells," BioMed research international, vol. 2013, p. 461329, 2013.

[31] B. Alberts, Molecular biology of the cell, 4th ed. New York, NY: Garland Science, 2002.

[32] K. E. Kasza et al., "Filamin A is essential for active cell stiffening but not passive stiffening under external force," Biophysical journal, vol. 96, no. 10, pp. 4326–4335, 2009.

[33] J. Pourati et al., "Is cytoskeletal tension a major determinant of cell deformability in adherent endothelial cells?," The American journal of physiology, vol. 274, no. 5 Pt 1, p. C1283-9, 1998.

[34] P. A. Janmey, U. Euteneuer, P. Traub, and M. Schliwa, "Viscoelastic properties of vimentin compared with other filamentous biopolymer networks," The Journal of cell biology, vol. 113, no. 1, pp. 155–160, 1991.

[35] H. Lee, J. M. Ferrer, F. Nakamura, M. J. Lang, and R. D. Kamm, "Passive and active microrheology for cross-linked F-actin networks in vitro," Acta biomaterialia, vol. 6, no. 4, pp. 1207–1218, 2010.

[36] G. H. Koenderink et al., "An active biopolymer network controlled by molecular motors," Proceedings of the National Academy of Sciences of the United States of America, vol. 106, no. 36, pp. 15192–15197, 2009.

[37] C. P. Broedersz and F. C. MacKintosh, "Molecular motors stiffen non-affine semiflexible polymer networks," Soft Matter, vol. 7, no. 7, p. 3186, 2011.

[38] J. R. Blundell and E. M. Terentjev, "Stretching Semiflexible Filaments and Their Networks," Macromolecules, vol. 42, no. 14, pp. 5388–5394, 2009.

[39] J. Stricker, T. Falzone, and M. L. Gardel, "Mechanics of the F-actin cytoskeleton," Journal of biomechanics, vol. 43, no. 1, pp. 9–14, 2010.

[40] P. A. Janmey et al., "Negative normal stress in semiflexible biopolymer gels," Nature materials, vol. 6, no. 1, pp. 48–51, 2007.

[41] P. R. Onck, T. Koeman, T. van Dillen, and E. van der Giessen, "Alternative explanation of stiffening in cross-linked semiflexible networks," Physical review letters, vol. 95, no. 17, p. 178102, 2005.

[42] K. Burridge and E. S. Wittchen, "The tension mounts: stress fibers as force-generating mechanotransducers," The Journal of cell biology, vol. 200, no. 1, pp. 9–19, 2013.

[43] P. Hotulainen and P. Lappalainen, "Stress fibers are generated by two distinct actin assembly mechanisms in motile cells," The Journal of cell biology, vol. 173, no. 3, pp. 383–394, 2006.

[44] A. M. Greiner, H. Chen, J. P. Spatz, and R. Kemkemer, "Cyclic tensile strain controls cell shape and directs actin stress fiber formation and focal adhesion alignment in spreading cells," PloS one, vol. 8, no. 10, pp. e77328, 2013.

[45] S. Lin, X. Han, G. C. Tsui, D. Hui, and L. Gu, "Active stiffening of F-actin network dominated by structural transition of actin filaments into bundles," Composites Part B: Engineering, vol. 116, pp. 377–381, 2017.

[46] S. Na, G. A. Meininger, and J. D. Humphrey, "A theoretical model for F-actin remodeling in vascular smooth muscle cells subjected to cyclic stretch," Journal of theoretical biology, vol. 246, no. 1, pp. 87–99, 2007.

[47] S. Tavares et al., "Actin stress fiber organization promotes cell stiffening and proliferation of pre-invasive breast cancer cells," Nature communications, vol. 8, p. 15237, 2017.

[48] M. Yoshigi, L. M. Hoffman, C. C. Jensen, H. J. Yost, and M. C. Beckerle, "Mechanical force mobilizes zyxin from focal adhesions to actin filaments and regulates cytoskeletal reinforcement," The Journal of cell biology, vol. 171, no. 2, pp. 209–215, 2005.

[49] S. Deguchi, T. Ohashi, and M. Sato, "Tensile properties of single stress fibers isolated from cultured vascular smooth muscle cells," Journal of biomechanics, vol. 39, no. 14, pp. 2603–2610, 2006.

[50] N. Wang, J. P. Butler, and D. E. Ingber, "Mechanotransduction across the cell surface and through the cytoskeleton," Science (New York, N.Y.), vol. 260, no. 5111, pp. 1124–1127, 1993.

[51] P. Fernández, P. A. Pullarkat, and A. Ott, "A master relation defines the nonlinear viscoelasticity of single fibroblasts," Biophysical journal, vol. 90, no. 10, pp. 3796–3805, 2006.

[52] B. Yan et al., "Duplicating Dynamic Strain-Stiffening Behavior and Nanomechanics of Biological Tissues in a Synthetic Self-Healing Flexible Network Hydrogel," ACS nano, vol. 11, no. 11, pp. 11074–11081, 2017.

[53] D. Riveline et al., "Focal Contacts as Mechanosensors," J Cell Biol, vol. 153, no. 6, pp. 1175–1186, 2001.

[54] K. Channon, E. H. C. Bromley, and D. N. Woolfson, "Synthetic biology through biomolecular design and engineering," Current opinion in structural biology, vol. 18, no. 4, pp. 491–498, 2008.

[55] M. P. Lutolf, "Integration column: artificial ECM: expanding the cell biology toolbox in 3D," Integrative biology : quantitative biosciences from nano to macro, vol. 1, no. 3, pp. 235–241, 2009.

[56] B. Han, D. Kim, U. H. Ko, and J. H. Shin, "A sorting strategy for C. elegans based on size-dependent motility and electrotaxis in a micro-structured channel," Lab on a chip, vol. 12, no. 20, pp. 4128–4134, 2012.

[57] T. Omori, Y. Imai, K. Kikuchi, T. Ishikawa, and T. Yamaguchi, "Hemodynamics in the microcirculation and in microfluidics," Annals of biomedical engineering, vol. 43, no. 1, pp. 238–257, 2015.

[58] M. Raab et al., "ESCRT III repairs nuclear envelope ruptures during cell migration to limit DNA damage and cell death," Science (New York, N.Y.), vol. 352, no. 6283, pp. 359–362, 2016.

[59] P. Rezai, A. Siddiqui, P. R. Selvaganapathy, and B. P. Gupta, "Electrotaxis of Caenorhabditis elegans in a microfluidic environment," Lab on a chip, vol. 10, no. 2, pp. 220–226, 2010.

[60] C. M. Denais et al., "Nuclear envelope rupture and repair during cancer cell migration," Science (New York, N.Y.), vol. 352, no. 6283, pp. 353–358, 2016.

[61] H. Bao, "Intracellular Dynamics of Acanthamoeba in Constrained, Micro-fabricated Environments," Master Thesis, Christian Albrechs Universitaet Kiel, Kiel, 2015.

[62] A. Raic, L. Rödling, H. Kalbacher, and C. Lee-Thedieck, "Biomimetic macroporous PEG hydrogels as 3D scaffolds for the multiplication of human hematopoietic stem and progenitor cells," , Biomaterials, vol. 35, no. 3, pp. 929–940, 2014.

[63] S. J. Hollister, "Porous scaffold design for tissue engineering," Nature materials, vol. 4, no. 7, pp. 518–524, 2005.

[64] S. B. Gutekunst, "Biophysical Investigation of Acanthamoeba castellanii Interactions with Target Cells and Biomimetic Materials," PhD Thesis, Christian Albrechs Universitaet Kiel, Kiel, 2015.

[65] D. Arcizet et al., "Contact-controlled amoeboid motility induces dynamic cell trapping in 3D-microstructured surfaces," Soft Matter, vol. 8, no. 5, pp. 1473–1481, 2012.

[66] P. M. Davidson, C. Denais, M. C. Bakshi, and J. Lammerding, "Nuclear deformability constitutes a rate-limiting step during cell migration in 3-D environments," Cellular and molecular bioengineering, vol. 7, no. 3, pp. 293–306, 2014.

[67] I. Y. Wong et al., "Collective and individual migration following the epithelial-mesenchymal transition," Nature materials, vol. 13, no. 11, pp. 1063–1071, 2014.

[68] E. Baumgart, "Stiffness--an unknown world of mechanical science?," Injury, vol. 31 Suppl 2, pp. S-B14-23, 2000.

[69] S. N. Khotimah, S. Viridi, and K. Widayani, "The dependence of the spring constant in the linear range on spring parameters," Physics Education, vol. 46, no. 5, p. 540, 2011.

[70] J. C. McMahon, "Medical Device Made From Self-Stiffening Composite," US6994723.

[71] R. Cross, "Elastic and viscous properties of Silly Putty," American Journal of Physics, vol. 80, no. 10, pp. 870–875, 2012.

[72] J. R. Ferguson, "Impact Shock Absorbing Material," US 8087101B2.

[73] Y. H. Tran, M. J. Rasmuson, T. Emrick, J. Klier, and S. R. Peyton, "Strain-stiffening gels based on latent crosslinking," Soft Matter, vol. 13, no. 47, pp. 9007–9014, 2017.

[74] M. E. Seitz et al., "Fracture and large strain behavior of self-assembled triblock copolymer gels," Soft Matter, vol. 5, no. 2, pp. 447–456, 2009.

[75] K. A. Erk, K. J. Henderson, and K. R. Shull, "Strain stiffening in synthetic and biopolymer networks," Biomacromolecules, vol. 11, no. 5, pp. 1358–1363, 2010.

[76] P. H. J. Kouwer et al., "Responsive biomimetic networks from polyisocyanopeptide hydrogels," Nature, vol. 493, no. 7434, pp. 651–655, 2013.

[77] R. K. Das, V. Gocheva, R. Hammink, O. F. Zouani, and A. E. Rowan, "Stress-stiffening-mediated stem-cell commitment switch in soft responsive hydrogels," Nature materials, vol. 15, no. 3, pp. 318–325, 2016.

[78] M. Jaspers et al., "Ultra-responsive soft matter from strain-stiffening hydrogels,", Nature communications, vol. 5, p. 5808, 2014.

[79] van Oosten, Anne S G et al., "Uncoupling shear and uniaxial elastic moduli of semiflexible biopolymer networks: compression-softening and stretch-stiffening," Scientific reports, vol. 6, p. 19270, 2016.

[80] E. I. Rivin, Stiffness and damping in mechanical design. New York: Marcel Dekker, 1999.

[81] J. Kolb, "Horizontal spring device for vehicle seats with elastomer spring element with progressive sprin characteristics," EP2416030B1.

[82] S. Kim, W. Moon, and Y. Yoo, "An efficient method for calculating the nonlinear stiffness of progressive multi-leaf springs," IJVD, vol. 29, no. 4, p. 403, 2002.

[83] Society of Automotive Engineers, Spring design manual, 2nd ed. Warrendale, Pa: SAE, 1996.

[84] F. Schneider, T. Fellner, J. Wilde, and U. Wallrabe, "Mechanical properties of silicones for MEMS," J. Micromech. Microeng., vol. 18, no. 6, p. 65008, 2008.

[85] R. S. Trask, H. R. Williams, and I. P. Bond, "Self-healing polymer composites: mimicking nature to enhance performance," Bioinspiration & biomimetics, vol. 2, no. 1, p. P1-9, 2007.

[86] S. C. Shit and P. Shah, "A Review on Silicone Rubber," Natl. Acad. Sci. Lett., vol. 36, no. 4, pp. 355–365, 2013.

[87] Wacker Chemie AG, Bonding, Selaing, Potting/Encapsulation and Coating with RTV Silicone Rubber Compounds.

[88] L. Xia, Z. Xu, L. Sun, P. M. Caveney, and M. Zhang, "Nano-fillers to tune Young's modulus of silicone matrix," J Nanopart Res, vol. 15, no. 4, p. 1, 2013.

[89] I. D. Johnston, D. K. McCluskey, C. K. L. Tan, and M. C. Tracey, "Mechanical characterization of bulk Sylgard 184 for microfluidics and microengineering," J. Micromech. Microeng., vol. 24, no. 3, p. 35017, 2014.

[90] Y. Yue, H. Zhang, Z. Zhang, and Y. Chen, "Polymer–filler interaction of fumed silica filled

polydimethylsiloxane investigated by bound rubber," Composites Science and Technology, vol. 86, pp. 1–8, 2013.

[91] J. S. Liu, S. P. Wu, M. Z. Chen, and Y. X. Mi, "The Effect of Filler on the Properties of Silicone Rubber," MSF, vol. 620-622, pp. 311–314, 2009.

[92] S. Vudayagiri, M. D. Junker, and A. L. Skov, "Factors affecting the surface and release properties of thin polydimethylsiloxane films," Polym J, vol. 45, no. 8, pp. 871–878, 2013.

[93] J. Liu et al., "Effects of Fumed and Mesoporous Silica Nanoparticles on the Properties of Sylgard 184 Polydimethylsiloxane," Micromachines, vol. 6, no. 7, pp. 855–864, 2015.

[94] M. A. Brook, "Platinum in silicone breast implants," Biomaterials, vol. 27, no. 17, pp. 3274–3286, 2006.

[95] S. Risse, B. Kussmaul, H. Krüger, and G. Kofod, "A versatile method for enhancement of electromechanical sensitivity of silicone elastomers," RSC Adv., vol. 2, no. 24, p. 9029, 2012.

[96] A. F. Bower, Applied mechanics of solids. Boca Raton, Fla.: CRC Press, 2010.

[97] T. A. Osswald and G. Menges, Materials Science of Polymers for Engineers, 1st ed. s.l.: Carl Hanser Fachbuchverlag, 2012.

[98] D. R. Askeland and W. Fahland, Materialwissenschaften: Grundlagen, Übungen, Lösungen. Heidelberg: Spektrum Akad. Verl., 1996.

[99] R. J. Young and P. A. Lovell, Introduction to Polymers, Third Edition, 3rd ed. Hoboken: CRC Press, 2011.

[100] G. Marckmann and E. Verron, "Comparison of Hyperelastic Models for Rubber-Like Materials," Rubber Chemistry and Technology, vol. 79, no. 5, pp. 835–858, 2006.

[101] R. Weiß and E. Osen, "FEM-Berechnung von Elastomerbauteilen," ATZ Automobiltech Z, vol. 103, no. 3, pp. 242–247, 2001.

[102] Ali, "A Review of Constitutive Models for Rubber-Like Materials," American Journal of Engineering and Applied Sciences, vol. 3, no. 1, pp. 232–239, 2010.

[103] M. Shahzad, A. Kamran, M. Z. Siddiqui, and M. Farhan, "Mechanical Characterization and FE Modelling of a Hyperelastic Material," Mat. Res., vol. 18, no. 5, pp. 918–924, 2015.

[104] A. Dorfmann, Ed., Constitutive models for rubber: Proceedings of the First European Conference on Constitutive Models for Rubber, Vienna, Austria, 9 - 10 September 1999. Rotterdam: Balkema, 1999.

[105] T. Guélon, E. Toussaint, J.-B. Le Cam, N. Promma, and M. Grédiac, "A new characterisation method for rubber," Polymer Testing, vol. 28, no. 7, pp. 715–723, 2009.

[106] C. Renaud, J.-M. Cros, Z.-Q. Feng, and B. Yang, "The Yeoh model applied to the modeling of large deformation contact/impact problems," International Journal of Impact Engineering, vol. 36, no. 5, pp. 659–666, 2009.

[107] M. Wagner, Lineare und nichtlineare FEM: Eine Einführung mit Anwendungen in der Umformsimulation mit LS-DYNA®. Wiesbaden: Springer Vieweg, 2017.

[108] O.-P. Jacquotte and J. Oden, "Analysis of hourglass instabilities and control in underintegrated finite element methods," Computer Methods in Applied Mechanics and Engineering, vol. 44, no. 3, pp. 339–363, 1984.

[109] X. Hu, R. H. Wagoner, G. S. Daehn, and S. Ghosh, "Comparison of explicit and implicit finite element methods in the quasistatic simulation of uniaxial tension," Commun. Numer. Meth. Engng., vol. 10, no. 12, pp. 993–1003, 1994.

[110] M. Wallmeier, E. Linvill, M. Hauptmann, J.-P. Majschak, and S. Östlund, "Explicit FEM analysis of the deep drawing of paperboard," Mechanics of Materials, vol. 89, pp. 202–215, 2015.

[111] J. M. Muthinja et al., "Tailored environments to study motile cells and pathogens," Cellular microbiology, vol. 20, no. 3, 2018.

[112] S. V. Avery, J. L. Harwood, and D. Lloyd, "Quantification and Characterization of Phagocytosis in the Soil Amoeba Acanthamoeba castellanii by Flow Cytometry," Applied and environmental microbiology, vol. 61, no. 3, pp. 1124–1132, 1995.

[113] J. Lorenzo-Morales, N. A. Khan, and J. Walochnik, "An update on Acanthamoeba keratitis: diagnosis, pathogenesis and treatment," Parasite (Paris, France), vol. 22, p. 10, 2015.

[114] L. A. Lautscham et al., "Migration in Confined 3D Environments Is Determined by a Combination of Adhesiveness, Nuclear Volume, Contractility, and Cell Stiffness," Biophysical journal, vol. 109, no. 5, pp. 900–913, 2015.

[115] C. S. Chen, "Geometric Control of Cell Life and Death," Science, vol. 276, no. 5317, pp. 1425–1428, 1997.

[116] K. Siemsen, "Adhesion of acanthamoeba on microstructured pillar substrates," Bachelor Thesis, Christian Albrechs Universitaet Kiel, Kiel, 2014.

[117] B. Bowers, "Acanthamoeba discriminates internally between digestible and indigestible particles," The Journal of cell biology, vol. 97, no. 2, pp. 317–322, 1983.

[118] N.-E. Oyunbaatar, D.-H. Lee, S. J. Patil, E.-S. Kim, and D.-W. Lee, "Biomechanical Characterization of Cardiomyocyte Using PDMS Pillar with Microgrooves," Sensors (Basel, Switzerland), vol. 16, no. 8, 2016.

[119] A. Haupt and N. Minc, "How cells sense their own shape - mechanisms to probe cell geometry and their implications in cellular organization and function," Journal of cell science, vol. 131, no. 6, 2018.

[120] V. Vogel and M. Sheetz, "Local force and geometry sensing regulate cell functions," Nature reviews. Molecular cell biology, vol. 7, no. 4, pp. 265–275, 2006.

[121] G. Aquino, L. Tweedy, D. Heinrich, and R. G. Endres, "Memory improves precision of cell sensing in fluctuating environments," Scientific reports, vol. 4, p. 5688, 2014.

[122] MicroChem Corp., Nano(TM) SU-8 Negative Tone Photoresist Formulations 2-25.

[123] B.-H. Jo, L. M. van Lerberghe, K. M. Motsegood, and D. J. Beebe, "Three-dimensional micro-channel fabrication in polydimethylsiloxane (PDMS) elastomer," J. Microelectromech. Syst., vol. 9, no. 1, pp. 76–81, 2000.

[124] J. L. Tan et al., "Cells lying on a bed of microneedles: an approach to isolate mechanical force," Proceedings of the National Academy of Sciences of the United States of America, vol. 100, no. 4, pp. 1484–1489, 2003.

[125] M. T. Yang, J. Fu, Y.-K. Wang, R. A. Desai, and C. S. Chen, "Assaying stem cell mechanobiology on microfabricated elastomeric substrates with geometrically modulated rigidity," Nature protocols, vol. 6, no. 2, pp. 187–213, 2011.

[126] S. Block, "Optimierung des Mikrogussverfahrens für PDMS Strukturen," Bachelor Thesis, Christian Albrechs Universitaet Kiel, Kiel, 2015.

[127] P.-Y. Wang et al., "Rapid Self-Assembly of Shaped Microtiles into Large, Close-Packed Crystalline Monolayers on Solid Surfaces," Small (Weinheim an der Bergstrasse, Germany), vol. 12, no. 10, pp. 1309–1314, 2016.

[128] C. W. Shields et al., “Field-directed of patchy anisotropic microparticles with defined shape,” Soft Matter, vol. 9, no. 38, pp. 9219–9229, 2013.

[129] J. F. Reverey, R. Fromme, M. Leippe, and C. Selhuber-Unkel, “In vitro adhesion of Acanthamoeba castellanii to soft contact lenses depends on water content and disinfection procedure,” Contact lens & anterior eye : the journal of the British Contact Lens Association, vol. 37, no. 4, pp. 262–266, 2014.

[130] S. B. Gutekunst, C. Grabosch, A. Kovalev, S. N. Gorb, and C. Selhuber-Unkel, “Influence of the PDMS substrate stiffness on the adhesion of Acanthamoeba castellanii,” Beilstein journal of nanotechnology, vol. 5, pp. 1393–1398, 2014.

[131] I. Schoen, W. Hu, E. Klotzsch, and V. Vogel, “Probing cellular traction forces by micropillar arrays: contribution of substrate warping to pillar deflection,” Nano letters, vol. 10, no. 5, pp. 1823–1830, 2010.

[132] R. N. Palchesko, L. Zhang, Y. Sun, and A. W. Feinberg, “Development of polydimethylsiloxane substrates with tunable elastic modulus to study cell mechanobiology in muscle and nerve,” PloS one, vol. 7, no. 12, pp. e51499, 2012.

[133] R. H. Pritchard, P. Lava, D. Debruyne, and E. M. Terentjev, “Precise determination of the Poisson ratio in soft materials with 2D digital image correlation,” Soft Matter, vol. 9, no. 26, p. 6037, 2013.

[134] M. Ozawa, T. Ozawa, M. Nishio, and K. Ueda, “The role of CH/π interactions in the high affinity binding of streptavidin and biotin,” Journal of molecular graphics & modelling, vol. 75, pp. 117–124, 2017.

[135] S. Paveenkittiporn, “Controlling Mechanical Properties of PDMS Microstructures with Surface Functionalization,” Master Thesis, Christian Albrechs Universitaet Kiel, Kiel, 2015.

[136] T. V. Ratto et al., “Force spectroscopy of the double-tethered concanavalin-A mannose bond,” Biophysical journal, vol. 86, no. 4, pp. 2430–2437, 2004.

[137] W. H. Binder, Ed., Self-Healing polymers: From principles to applications. Weinheim, Bergstr: Wiley-VCH, 2013.

[138] N. Xia, J. S. Shumaker-Parry, M. H. Zareie, C. T. Campbell, and D. G. Castner, “A Streptavidin Linker Layer That Functions after Drying,” Langmuir, vol. 20, no. 9, pp. 3710–3716, 2004.

[139] G. M. Whitesides, “The origins and the future of microfluidics,” Nature, vol. 442, no. 7101,

pp. 368–373, 2006.

[140] M. Mikrut, “Low surface energy rubber materials: Relationship between network architecture and tack of silicone rubbers,” University of Twente, Enschede, 2007.

[141] B. Assmann and P. Selke, Technische Mechanik 1: Band 1: Statik, 18th ed. München: Oldenbourg Wissenschaftsverlag, 2009.

[142] J. van Eijk, “On the design of plate-spring mechanisms,” Doctoral thesis, Tu Delft, Delft, 1985.

[143] K. Gieck and R. Gieck, Technische Formelsammlung, 30th ed. Germering: Gieck, 1995.

[144] G. R. Cowper, “The Shear Coefficient in Timoshenko’s Beam Theory,” J. Appl. Mech., vol. 33, no. 2, p. 335, 1966.

[145] Z. Chen, T. Scheffer, H. Seibert, and S. Diebels, “Macroindentation of a soft polymer: Identification of hyperelasticity and validation by uni/biaxial tensile tests,” Mechanics of Materials, vol. 64, pp. 111–127, 2013.

[146] M. Timmermann, S. B. Gutekunst, C. Selhuber-Unkel, and E. Quandt, “Schicht mit variabler Festigkeit,” DE102016107480B4, Germany.

[147] Beckhoff Automation, Beckhoff Information System: Reibungskoeffizient. [Online] Available: https://infosys.beckhoff.com/index.php?content=./content/1031/tc_motion_designer/2761712779.html&id=5193980904707027356. Accessed on: Oct. 12 2018.

[148] A. Schweizer, Formelsammlung und Berechnungsprogramme Anlagenbau: Reibwerte verschiedener Materialien. [Online] Available: https://www.schweizer-fn.de/stoff/reibwerte/reibwerte.php. Accessed on: Oct. 12 2018.

[149] M. Smith, ABAQUS/Standard Unser´s Manual, Version 6.9. Providence, RI.

[150] M. Wind and C. Schindler, Numerische und experimentelle Analyse und Optimierung der technischen Eigenschaften eines selbstexpandierenden Stents. Zugl.: Kaiserslautern, Techn. Univ., Diss., 2011. Kaiserslautern: Universitätsbibliothek Kaiserslautern, 2011.

[151] S. Stölting, “Verfahrensentwicklung zur Herstellung Monodisperser Alginat-Mikro-Kügelchen,” Bachelor Thesis, Christian Albrechs Universitaet Kiel, Kiel.

[152] K. Siemsen, “Coating and functionalization of NiTi-structures with alginate and their cha-

racterization with respect to cell properties," Master Thesis, Christian Albrechs Universitaet Kiel, Kiel, 2016.

[153] Dielectric Corporation, Polystyrene: General Material Properties. [Online] Available: http://www.dielectriccorp.com/downloads/thermoplastics/polystyrene.pdf. Accessed on: Oct. 16 2018.

[154] D. Rus and M. T. Tolley, "Design, fabrication and control of soft robots," Nature, vol. 521, no. 7553, pp. 467–475, 2015.

[155] A. D. Marchese, R. K. Katzschmann, and D. Rus, "A Recipe for Soft Fluidic Elastomer Robots," Soft robotics, vol. 2, no. 1, pp. 7–25, 2015.

[156] B. Lunenfeld and P. Stratton, "The clinical consequences of an ageing world and preventive strategies," Best practice & research. Clinical obstetrics & gynaecology, vol. 27, no. 5, pp. 643–659, 2013.

[157] B. Pomeranz, U. Adler, N. Shenoy, C. Macaluso, and S. Parikh, "Prosthetics and orthotics for the older adult with a physical disability," Clinics in geriatric medicine, vol. 22, no. 2, p. 377-94; ix, 2006.

[158] S. Portnoy, A. Frechtel, E. Raveh, and I. Schwartz, "Prevention of Genu Recurvatum in Poststroke Patients Using a Hinged Soft Knee Orthosis," PM & R : the journal of injury, function, and rehabilitation, vol. 7, no. 10, pp. 1042–1051, 2015.

[159] A. Frechtel, S. Portnoy, E. Raveh, and I. Schwartz, "Prevention of knee hyperextension in stroke patients using a knee orthosis: 3D computational gait analysis and dynamic EMG," Gait & Posture, vol. 38, pp. S85, 2013.

[160] M. Mirbagheri, D. Mohebbi-kalhori, and N. Jirofti, "Evaluation of Mechanical Properties and Medical Applications of Polycaprolactone Small Diameter Artificial Blood Vessels," Int J Basic Sci Med, vol. 2, no. 1, pp. 58–70, 2017.

[161] J. Chlupác, E. Filová, and L. Bacáková, "Blood vessel replacement: 50 years of development and tissue engineering paradigms in vascular surgery," Physiological research, vol. 58 Suppl 2, p. S119-39, 2009.

[162] S. Sarkar, H. J. Salacinski, G. Hamilton, and A. M. Seifalian, "The mechanical properties of infrainguinal vascular bypass grafts: their role in influencing patency," European journal of vascular and endovascular surgery : the official journal of the European Society for Vascular Surgery, vol. 31, no. 6, pp. 627–636, 2006.

[163] G. Sommer, P. Regitnig, L. Költringer, and G. A. Holzapfel, "Biaxial mechanical properties of intact and layer-dissected human carotid arteries at physiological and supraphysiological loadings," American journal of physiology. Heart and circulatory physiology, vol. 298, no. 3, p. H898-912, 2010.

[164] G. A. Holzapfel, G. Sommer, C. T. Gasser, and P. Regitnig, "Determination of layer-specific mechanical properties of human coronary arteries with nonatherosclerotic intimal thickening and related constitutive modeling," American journal of physiology. Heart and circulatory physiology, vol. 289, no. 5, p. H2048-58, 2005.

Acknowledgements

Zuerst möchte ich mich bei Frau Prof. Dr. Christine Selhuber-Unkel für die Möglichkeit in ihrer Arbeitsgruppe meine Promotionsarbeit anfertigen zu dürfen bedanken. Ich möchte mich aber auch bei ihr dafür bedanken, dass sie mir stets den Freiraum gegeben hat, den ich zum Arbeiten brauchte, mir aber gleichzeitig immer mit ihrem Wissen und ihrer Erfahrung zur Seite stand.

Ganz besonders möchte ich mich bei meinen aktuellen und ehemaligen Kollegen in der Arbeitsgruppe Biokompatible Nanomaterialien bedanken: Christine Arndt, Angelika Duttmann, Sören Gutekunst, Britta Hesseler, Steven Huth, Laith Kadem, Tina Kerby, Manuela Lieb, Nils Lukat, Hendrikje Neumann, Julia Reverey, Katharina Siemsen, Sandra Sindt, Reza Taale und Tobias Tellkamp. Ihr habt stets für eine wunderschöne Arbeitsatmosphäre gesorgt. Spezieller Dank gilt Ellen Riemer für zahlreiche aufbauende und lachmuskeltrainierende Gespräche.

Ich möchte mich weiterhin bei denen bedanken, die durch ihre Bachelor- und Masterarbeiten sowie durch HiWi-Tatigkeiten zu meiner Arbeit beigetragen haben. Dies sind Tobias Bichel, Sören Block, Huu Chánh Trinh, Supattra Paveenkittiporn, Karolin Thiemann and Saman Stölting.

I would like to thank my coworkers that were part of the research on Amoeba Nils Lukat, Lindsay P. Schneider, Dr. C. Wyatt Shields IV and Prof. Dr. Gabriel P. López for providing samples, for helping with experiments and image analysis and for the scientific input.

I would like to thank the ERC for funding the research presented in my thesis, which was part of the Starting Grant 336104.

Mein Dank gilt dem Deutschen Akademischen Austauschdienst für die Förderung des DAAD RISE Stipendiums für Lindsay P. Schneider, das für viele interessante Entdeckungen gesorgt hat.

Dafür, dass sie stets meine Ideen in Hardware umgesetzt haben, möchte ich mich bei allen Mitarbeitern der Werkstatt der Technischen Fakultät, speziell Bernd Neumann, herzlich bedanken.

Für die Hilfe bei der mechanischen Charakterisierung meiner Proben möchte ich mich bei Sören Kaps und Leonard Siebert vom Lehrstuhl für Funktionale Nanomaterialien sowie Christoph Chluba vom Lehrstuhl für Anorganische Funktionsmaterialien bedanken.

Weiterhin bin ich Fabian Schütt und Bastian Gothe für die Freundschaft im Studium und auch danach dankbar.

Ich möchte mich bei Steven Huth, Christine Arndt, Sandra Sindt, Laith Kadem, Nils Lukat und Enno Lage für das Korrekturlesen der Arbeit und bei Heinz von Bockelmann für die sprachliche Unterstützung bedanken.

Da mein Leben in den letzten vier Jahren nicht nur aus Arbeit bestand, möchte ich mich auch bei Maike und Lutz für die zahlreichen Stunden unbeschwerter Freizeit bedanken. Auch möchte ich mich bei Tobi, der weit mehr also nur mein Nachbar ist, für eine stets offene Tür und ein stets offenes Ohr bedanken.

Ich bedanke mich bei meinen Eltern und meinen Brüdern für die Unterstützung in den letzten Jahrzehnten, die dafür gesorgt hat, dass ich ein glücklicher Mensch bin, der gerade eine Danksagung einer Doktorarbeit schreibt.

Zu guter Letzt möchte ich mich bei den beiden wichtigsten Personen in meinem Leben bedanken: Martje, vieles was ich hier schreiben möchte wäre zu persönlich für einen öffentlich zugänglichen Text. Deshalb möchte ich dir an dieser Stelle dafür danken, dass du mich während der letzten 7 Jahre unglaublich unterstützt hast und mein Leben in allen Belangen bereichert hast. Ole, wenn du in der Lage bist das zu lesen, ist dieser Text schon einige Jahre alt. Du hast aber in der Zeit, in der ich diesen Text verfasst habe, dafür gesorgt, dass ich aus einem anderen Blickwinkel auf die wichtigen und eher nicht so wichtigen Dinge im Leben sehe und dadurch meine Leben und diese Arbeit sehr positiv beeinflusst.

Abbreviations, symbols and variables

A. castellanii	*Acanthamoeba castellanii*
$\boldsymbol{a}$	Vector of the accelerations at each node in FEM
a	Fitting parameter for the calculation of a pillar deformation
B	Cauchy-Green Deformation tensor
$\boldsymbol{B}$	Matrix conatin derivatives of the basis function with respect to global coordiantes in FEM
C	Matrix describing material properties in FEM
d	Distance between slats of the strain-stiffening structure
D	Sample-depth of the strain-stiffening structure
d'	Extension of a spring
D'	Mean diameter of a coil spring
d''	Wire diameter of a coil spring
D''	Diameter of a pillar
d'''	Distance between two parallel lines
$d'''*$	Nearest distance between two tilted parallel lines
DS	Strain-stiffening demonstrator sample.
$\boldsymbol{D}_{\varepsilon}$	Differential operator matrix in FEM
E	Young´s modulus
ECM	Extracellular Matrix
F	Force
$\boldsymbol{f}$	Force acting on all nodes in FEM
$\boldsymbol{f}^{e}$	Force acting on an element in FEM
FEM	Finite element method
g	Gap between sets of slats
G	Shear modulus
h	Backbone-thickness of the strain-stiffening structure
I	Moment of inertia
I	Identity tensor
I_1 , I_2 , I_3	Invariants of the Cauchy-Green deformation tensor
k	Spring constant
K	Timoshenko shear coefficient
$\boldsymbol{K}$	Stiffness matrix in FEM
$\boldsymbol{K}^{e}$	stiffness matrix of a single element in FEM
l	Slat-length of the strain-stiffening structure
L'	Length of a pillar
l'_0	Original length of a deformed object
$\boldsymbol{M}$	Mass matrix that contains information about the position of all nodes in FEM

N	Number of slats of the strain-stiffening structure
$\boldsymbol{N_i}$	Matrix of polynomial basis functions in FEM
n_a	The number of active coils of a coil spring
p_i	Pitch of a coil spring
p	Protrusion-length of the strain-stiffening structure (tensile tests)
p'	Protrusion-length of the strain-stiffening structure (FEM)
p''	Arbitrary scalar parameter for the calculation of the Cauchy stress tensor $\boldsymbol{\sigma}$
PDMS	Polydimethylsiloxane
$S_{d\_2.5}$	Strain-stiffening sample distance between slats of 2.5 mm all other dimensions are the same as *DS*
S_{h_10}	Strain-stiffening sample with backbone-thickness of 10 mm all other dimensions are the same as *DS*
$S_{w\_1.3}$	Strain-stiffening sample with slat-width of 1.3 mm all other dimensions are the same as *DS*
$S_{w\_1.3\_h\_10}$	Strain-stiffening sample with slat-width of 1.3 mm and backbone-thickness of 10 mm all other dimensions are the same as *DS*
$\mathbf{t}$	Vector of internal node forces in FEM
$\mathbf{u}$	Displacement of all nodes in FEM
$\mathbf{u^e}$	Displacement of an element in FEM
$\mathbf{\tilde{u}^e(x)}$	Deformation of a finite element in FEM
W	Strain energy density
w	Slat-width of the strain-stiffening structure
α	Tilting angle of two parallel lines
δ	Deflection of a pillar or slat
$\Delta l'$	Increase in length of a deformed object
ε	Strain
$\lambda_1, \lambda_2, \lambda_3$	Principal stretches of a solid
μ_1, μ_2, μ_3	Material constants in a strain energy density W
v'	Velocity
σ	Stress
$\boldsymbol{\sigma}$	Cauchy stress tensor
σ_{max}	Maximum stress on a structure

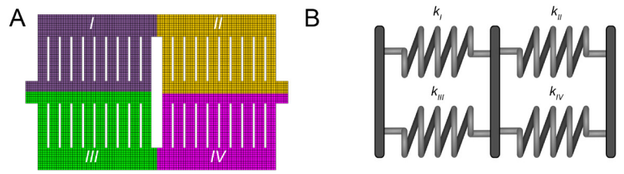

Figure 4.9A: The simulated demonstrator sample can be simplified by assuming four equal parts. Each part is marked with a different color and number. B: The mechanical properties of the sample can be represented by a series of two parallel arrangements of two springs. Each spring represents the stiffness of one part of the sample.

$$k_{DS} = \frac{1}{\frac{1}{k_I + k_{II}} + \frac{1}{k_{III} + k_{IV}}} \tag{4.1}$$

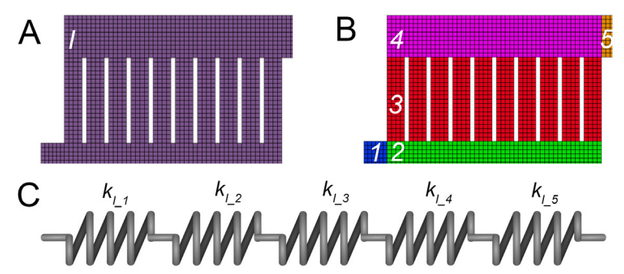

Figure 4.10: The purple quarter-structure of the simulated demonstrator sample (A) can be treated as a combination of five parts (B). Each part is marked with a different color and number and can be represented by a spring. The mechanical behavior of the entire quarter-structure can be described by that series of five springs. k_{I_i} are the corresponding spring constants.

$$k_I = \frac{1}{\frac{1}{k_{I\_1}} + \frac{1}{k_{I\_2}} + \frac{1}{k_{I\_3}} + \frac{1}{k_{I\_4}} + \frac{1}{k_{I\_5}}} \tag{4.2}$$

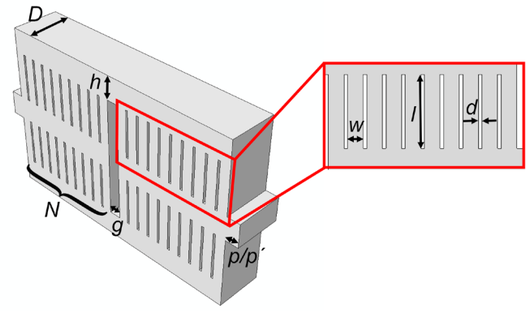

Figure 4.8: Sketch of the demonstrator sample with backbone-thickness *h*, number of slats *N*, slat-length *l*, slat-width *w*, distance between slats *d*, sample depth *D*, protrusion length *p/p'* and gap between sets of slats *g*.

$$\sigma = E\varepsilon \text{ with } \sigma = \frac{F}{A}, A = D \cdot h, \varepsilon = \frac{\Delta l^*}{l^*} \text{ and } k = \frac{F}{\Delta l^*} \tag{4.3}$$

$$k = E\frac{D \cdot h}{l^*} \tag{4.4}$$

$$k = \frac{EDw^3}{L^{*3}} \tag{4.5}$$